論文 / 著書情報
Article / Book Information

題目(和文)	
Title(English)	Evolution of Pre-Main Sequence Stars and Its Environmental Impact on Their Circumstellar Disks
著者(和文)	國友正信
Author(English)	Masanobu Kunitomo
出典(和文)	学位:博士（理学）, 学位授与機関:東京工業大学, 報告番号:甲第9719号, 授与年月日:2015年3月26日, 学位の種別:課程博士, 審査員:井田　茂,中本　泰史,佐藤　文衛,野村　英子,長澤　真樹子
Citation(English)	Degree:, Conferring organization: Tokyo Institute of Technology, Report number:甲第9719号, Conferred date:2015/3/26, Degree Type:Course doctor, Examiner:,,,,
学位種別(和文)	博士論文
Type(English)	Doctoral Thesis

Evolution of Pre-Main Sequence Stars and Its Environmental Impact on Their Circumstellar Disks

Masanobu Kunitomo

Department of Earth and Planetary Sciences,
Tokyo Institute of Technology

Doctoral Thesis
2015

Abstract

Planetary systems consist of a host star and planets. Since the gravitational and radiation fields of the planetary systems are dominated by the host star, the host star ' s properties is essential for the formation and evolution of planets. The understanding of the formation and evolution of stars have been advanced last a few decades, thanks to the innovative progress of both numerical simulations and observations. However, there are still some unresolved problems such as the luminosity-spread problem and the surface composition anomaly of the Sun. The observed luminosities of some young stars in clusters are much smaller than expected from the stellar evolution theory at the cluster age. The spectroscopic observations have revealed that the solar surface abundance of the refractory elements is lower than the sun-like stars. These may imply that there are some missing effects on the stellar evolution process. Recently the multidimensional hydrodynamic simulations have been performed and it has been revealed that the materials accrete onto a star via a circumstellar disk. This is different from the spherical accretion, which is assumed in the classical studies. With this finding of the accretion configuration, the star formation has been revisited. It was found that the disk accretion has a potential to change the evolution of the PMS stars significantly: The radius and luminosity become much smaller and the internal structure evolution proceeds more quickly, compared to the classical evolution. Therefore the effect of the disk accretion is a promising solution of the luminosity-spread problem. Since this is a highly important issue in the context of both the star formation itself and even the planet formation, we have studied the PMS evolution with disk accretion under a variety of settings with especially focusing on the internal structure evolution.

We simulated the PMS evolution from the protostar to the main sequence star with accretion. We integrated the stellar evolution code with including the effect of the multidimensional configuration of the accretion flow.

We found that the PMS evolution is highly affected by the accreting material ' s entropy and the deuterium content. We showed that the less luminous stars are formed by the accretion with the low entropy or the deuterium-poor accretion. Moreover, we found that the internal structure of the young stars is also highly affected by the disk accretion. We examined the age of the surface convective zone shrinkage in the case of a solar-mass stars and found that it can be about a few million years if the accreting material ' s entropy and the deuterium content are low. This is significantly shorter than the classical PMS evolution and even shorter than the protoplanetary disk ' s lifetime. This can be important for the stellar surface composition. If

the materials with the different composition from the stellar surface accrete onto the star with the shallow convective zone, then the stellar surface composition is changed. We suggest that this process happened in the young Sun if the disk lifetime is as long as ten million years.

Furthermore, the different evolution of the stellar radiation field has an impact on the disk evolution. We showed that the PMS evolution affects the disk evolution and lifetime using a simple one-dimensional accretion disk model.

Contents

Chapter 1

Introduction

In this chapter, first we review the classical picture of the formation of low- and intermediate-mass stars. After the recent progress has been summarized, the problems and the purpose of this study are described.

Since the classical picture is based on the one-dimensional hydrodynamic simulation (Stahler et al. 1980a, Masunaga & Inutsuka 2000), the spherical accretion is obviously assumed. However, recent multi-dimensional radiation- (magneto-) hydrodynamic simulations revealed that the accretion occurs via disk accretion rather than the spheric accretion Machida et al. (e.g., 2008). This different accretion lead to the different entropy of the accreting material and then the evolution is changed.

1.1 Overview of star formation

Here we describe the general picture of star formation. A star is formed through the collapse of the dense region in a molecular cloud. The temperature and the number density of the molecular cloud are typically 10 K and $n_{\rm H} \sim 10^4$ cm^{-3}. Although the cloud is supported by the pressure, a certain perturbation makes the gravity overcome the pressure and causes the dynamical collapse. Since the timescale of the collapse is inversely proportional to the square root of the density, the dense central region experiences the runaway collapse. After the core is dense enough to be adiabatic, the temperature increases due to the compressional heating and then the thermal pressure becomes comparable to the gravity at some point. Thus, in the central region the hydrostatic equilibrium is satisfied. This object is called a "first core" (Larson 1969).

Due to the runaway collapse of the central region, the material initially located in the

our region of the molecular cloud core accretes onto the first core later and then the first core mass increases. The increase of mass makes the central temperature higher and then the central temperature reaches about 2000 K at some point. At 2000 K, the hydrogen molecules dissociates. Since this reaction is strongly endothermic, in the central region the pressure is again overcome by the gravity. This collapse is called the "second collapse". After the dissociation of hydrogen molecules completes, the pressure becomes comparable to the gravity and the hydrostatic equilibrium is again satisfied. This object is called a "second core" or "protostar" (Larson 1969).

The second core still accretes the material which was initially located in the outer region of the molecular cloud core. Then, the mass of the second core increases and at the time when the cloud mass is zero, the star formation completes.

This is the general picture of the star formation. The star formation can be split into two phases: We call "the collapse phase" prior to the protostar formation, while the later phase is called "the (main) accretion phase" until the accretion ceases. In this thesis we focus on the later accretion phase.

1.1.1 Evolution after the accretion phase

After the accretion ceases, the star experiences the quasi-static evolution until reaching the main sequence (MS) through two paths: the Hayashi track and Henyey track.

The star after the accretion phase has a large luminosity and radius according to the one-dimensional hydrodynamic simulation through the accretion phase (Stahler et al. 1980a, Winkler & Newman 1980). In the case of the formation of a 1 $M_\odot$ star, the luminosity and radius are about 10 $L_\odot$ and 5 $R_\odot$.

Then, on the Hertzsprung-Russell (H-R) diagram, the low-mass star evolves downward along their *Hayashi track* (named after C. Hayashi, Hayashi 1961). The Hayashi track denotes the locus of fully convective stars and also represents the borderline between the allowed and forbidden region. To the right of the Hayashi track, i.e., in the lower temperature region, there is no solution of a star in the hydrodynamic equilibrium. Since the opacity has a strong sensitivity on the temperature due to the negative hydrogen ions, the Hayashi track is not sensitive to the temperature and then it is almost vertical line on the H-R diagram as shown in Fig. 1.1.

During the Hayashi phase (the phase in which the star located on the Hayashi track), the star experiences the Kelvin-Helmholtz (K-H) contraction. The K-H contraction is the quasi-static contraction by the energy loss via radiation. Thus its timescale is determined by the total energy over the luminosity and in the 1 $M_\odot$ star it is about 10^7 yr (see Fig. 1.1). As

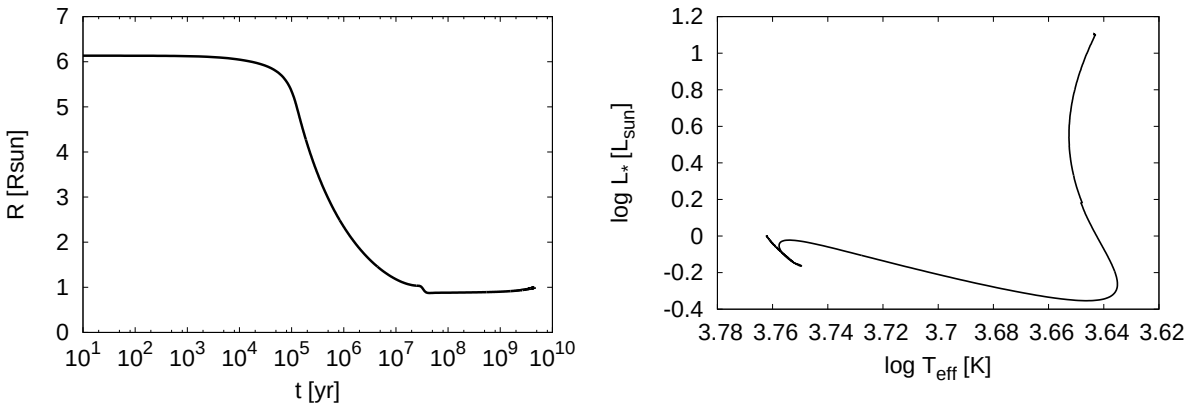

Figure 1.1: Radius evolution (left panel) and evolutionary track of a 1 $M_\odot$ star with no accretion until the solar age, 4.567 Gyr.

the contraction proceeds, the temperature of the stellar interior increases. This is because the steeper pressure gradient is needed in order to support the stronger gravity. As a result of the temperature increase, the opacity becomes low enough for the radiative transfer to work and then the radiative core develops.

After the radiative core develops, the star leaves their Hayashi track and moves to the *Henyey track*, since the Hayashi track denotes the locus of fully convective stars. On the Henyey track, the star keeps contracting with increasing the characteristic temperature. Then, when the central temperature becomes high enough to cause the hydrogen burning, the star becomes a main sequence (MS) star.

We define a star until reaching MS as a Pre-Main-Sequence (PMS) star including the protostar [1].

1.2 Recent picture of star formation: Disk accretion

Recently it has been proposed by Baraffe et al. (2009) that the PMS evolution can be largely different from the classical picture described above. Here we summarize the differences from the classical picture and its origin.

Recently the multi-dimensional simulations of star formation have been intensively conducted (e.g., Vorobyov & Basu 2010, Machida et al. 2008, Tomida et al. 2010). They revealed that the first core has a disk-like morphology unlike the sphere in the classical picture. This is because the angular momentum of the molecular cloud core is large. In the second collapse,

[1]Note that the PMS star is sometimes defined as the phase after the accretion completes. Here the mass accretion phase is also included into the PMS phase.

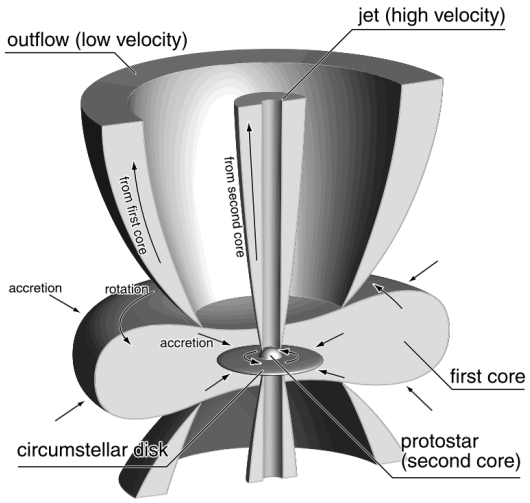

Figure 1.2: Schematic picture of the protostar and its envelope during the main accretion phase after Machida et al. (2008). The first core has a thick disk-like shape and the protostar accretes mass through the circumstellar disk.

the second core (protostar) is formed at the central region of the disk-like fist core, while most of the first core forms the circumstellar disk. Figure 1.2 shows the schematic picture of this morphology. Thus, most materials accrete onto the protostar through the disk with losing their angular momentum via the magnetic braking.

This update in the accretion configuration from the classical spheric accretion results in the drastic change in the PMS evolution. This is because the different accretion configuration leads to change the accreting material largely.

In the classical calculations (e.g., Stahler et al. 1980a, Winkler & Newman 1980), the one-dimensional hydrodynamic simulation were conducted. Therefore, the material accretes onto the star via the spherical accretion. In the spherical accretion, the radiation generated at the shock front can not be radiated away to space because there are a lot of materials in the radial direction and they serves the blanket effect. Therefore, the accreting material's entropy is large.

On the other hand, if the materials accrete onto the protostar through the circumstellar disk, the gravitational energy of the accreting material is thermalized in the disk and radiated away before reaching the stellar surface. Moreover, at the stellar surface, the entropy may be radiated away to space efficiently because there are little materials in the direction normal to the disk (Hartmann et al. 1997). Thus, it is possible that the materials accrete onto the star through the circumstellar disk with the lower entropy than the classical model with the spherical accretion (see Fig. 1.3). In this sense, the disk accretion with low entropy is called "*the cold accretion*", whereas the accretion with the high entropy injection as in the spherical accretion

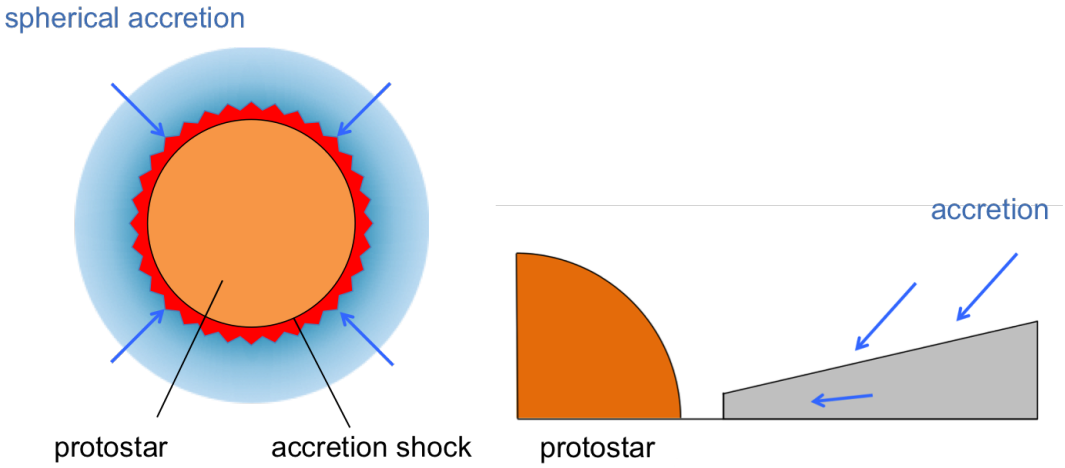

Figure 1.3: Schematic pictures of the spherical (left panel) and the spherical accretion (right panel).

is called "*the hot accretion*".

1.2.1 Present understanding and problems on the PMS evolution with cold accretion

Baraffe et al. (2009) calculated the PMS evolution in the cold accretion model. They showed the drastic differences in the PMS evolution. Baraffe et al. (2009), and the following studies by Baraffe & Chabrier (2010), Hosokawa et al. (2011), Baraffe et al. (2012), Dunham & Vorobyov (2012), found that the cold accretion changes the PMS evolution dramatically compared to the classical PMS evolution in the following respects: (1) The shifts of evolutionary tracks, (2) the smaller radius and (3) the different internal structure evolution.

These changes are important not only for the stellar and solar physics but the planet formation theory. Obviously the change in the evolution tracks directly affects the estimation of the stellar properties such as the stellar age and mass, the initial mass function, and so on. Furthermore, the change of the host star's evolution affects the planet formation. The host star govern the radiation and gravitational fields in the planetary system. The change in the ultraviolet or X-ray luminosity of the host star affects the disk evolution and the change in the stellar internal structure affects the close-in planet's orbit via the tidal interaction. Therefore, we stress that the accurate understanding of the PMS evolution is very important for the wide range of studies.

Here we summarize the current understandings and problems on the PMS evolution with cold accretion. Although we describe the effect of the change in the evolutionary tracks in detail in order to stress the importance and impacts of the cold accretion, in particular we focus on

the internal structure evolution in this thesis.

Evolutionary tracks with cold accretion

Among the impacts of the cold accretion, in particular, much attention has been paid to the evolutionary tracks. This is because (1) the evolutionary tracks can be directly compared with the observation, (2) the change of the evolutionary tracks may be the solution for the long-standing problem ("luminosity spread problem"), and (3) the change in the evolutionary tracks directly affects the determination of the stellar age and mass.

Luminosity spread problem. It is currently well known that the luminosity of the observed PMS stars in young star-forming regions widely spreads on the H-R diagram. Figure 1.4 show the PMS stars which covers the region between 1 and 10 Myr isochrones derived by the classical model (Baraffe et al. 1998)[2]. If the isochrones in the classical model are accurate, this wide spread directly corresponds to the large variation of the age ($\sim 10^7$ yr; e.g., Hillenbrand 2009). However, considering the timescale for the star formation in a cluster is at most $\sim 10^6$ yr, the ages should match within the accuracy of $\sim 10^6$ yr. This contradiction is called "luminosity spread problem" and still remains an important issue on the star formation. There are three possible solutions: (I) The observational error, (II) the star formation occurs for a long period of time in a cluster and (III) the classical evolutionary tracks are not valid.

Baraffe et al. (2009) claimed that the cold accretion can be the solution of this problem. Since the PMS star's evolutionary tracks in the cold accretion model are changed largely, the luminosity spread can be explained if stars formed by the cold accretion and those by the hot accretion are mixed in the star forming region. Thus, the luminosity spread problem can be naturally explained by the existence of the cold accretion.

Impact on the stellar mass and age. The update of the evolutionary tracks has another important influence. The stellar age and mass are in general evaluated by the comparison of the observed stellar temperature and luminosity with the theoretical evolutionary tracks. Thus, the update in the evolutionary tracks directly affects the estimated age and mass. Baraffe et al. (2012) claimed that the age and mass of the PMS stars determined with the classical evolutionary tracks can be overestimated by a factor of several or more and 40% or more, respectively. Baraffe et al. (2009) also pointed out that this update of the stellar mass has a potential to affect our understanding of the initial mass function (IMF).

Although this is a surprisingly huge difference, recently a possible evidence has been reported by Stassun et al. (2014). They determined the mass of 26 eclipsing binaries independent

[2]Isochrone is the line connecting points of many evolutionary tracks with the various mass at the same age.

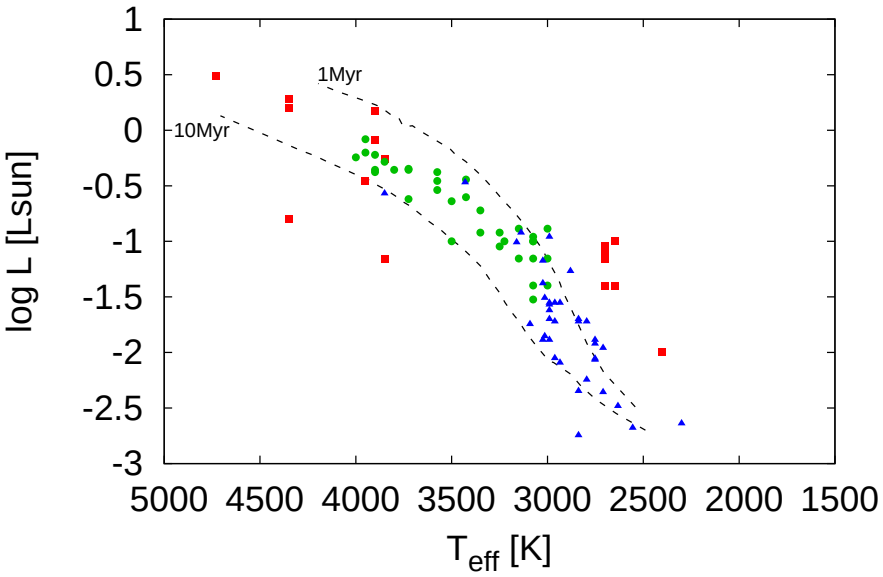

Figure 1.4: Observed young stellar objects in Tauras and Chamaeleon I (blue, Muzerolle et al. 2005), ρ Ophiucus (red, Gatti et al. 2006) and σ Orionis (green Gatti et al. 2008). The dashed lines show the isochrone at 1 (upper line) and 10 Myr in the classical model (Baraffe et al. 1998). The observed objects widely spread from 1 to 10 Myr isochrones.

of the theoretical evolutionary tracks and used it to verify the accuracy of the standard theoretical PMS evolutionary tracks. The stellar mass of the binary member can be determined dynamically with the orbital period and the radial velocity. Note that the mass determined by this method does not include the uncertainty of the stellar evolution theory. They found that no theoretical evolutionary tracks reproduce all binaries and the error of the mass determined by the evolutionary tracks is at most 100%. Therefore, the surprisingly huge difference in the mass estimation may be needed.

Internal structure evolution

Furthermore, the internal structure evolution is also changed by the cold accretion. Baraffe & Chabrier (2010) found that the decrease in the injected energy into the star makes the stellar radius small during the PMS phase. In the classical model, the radius of the 1 $M_{\odot}$ PMS star is about 5 $R_{\odot}$ or more, while it is ~ 1 $R_{\odot}$ or less in the disk accretion model. This big difference is critical for the internal structure evolution. In order to support the stronger gravity in the smaller stars, the central temperature needs to be higher. The higher temperature decreases the opacity and then the radiation tends to be effective. Therefore, the radiative core develops in the earlier phase, namely the surface convective region shrinks earlier than the classical model.

Baraffe & Chabrier (2010) investigated the internal structure evolution of a 1 $M_\odot$ star with cold accretion and found that the surface convective zone can shrink at $\sim$ 5 Myr. This means that it can shrink before the protoplanetary disk's lifetime ($\sim$ 6 Myr, Haisch et al. 2001) and then before the planet formation completes. Thus, the update in the PMS evolution is possible to affect or to be affected by the planet formation process in the following ways.

- migration of close-in planets through the tidal dissipation in the surface convective zone
- pollution of the accreted material onto the thin convective zone
- stellar magnetic field and the surface activity

Hence, the internal structure evolution may have an impact on not only the stellar evolution theory but also the planet formation theory.

Pollution of the stellar surface

Here we especially focus on the pollution of the 1 $M_\odot$ star's surface composition. The accreted material is distributed within the surface convective zone. If the star is fully convective, the effect of the accreting material is negligible. On the contrary, if the mass in the surface convective zone is comparable to the disk mass when the protoplanetary disk exists, the accreted material has a strong impact on the stellar surface composition because planet formation can change the composition of the accreting material significantly. For example, the mass in the surface convective zone of the present-day Sun is only $\sim$ 2% by helioseismic observation (see Chap. 2). This is comparable to the protoplanetary disk's mass. Therefore, the cold accretion with planet-forming disk has a potential to influence the stellar surface composition. Note that this scenario does not work in the classical picture because the PMS stars in the classical model have fully convective structure for $\sim$ 30 Myr.

The pollution mechanism can be important in terms of the estimation of the stellar property, the planet survey, and the solar peculiar surface composition.

Impact on the stellar evolution. If the surface composition is affected by the accreting material largely, the surface composition is totally different from the bulk composition. For example, the metallicity of the Sun is under debate. From the atmospheric composition by spectroscopic observation, the solar metallicity is estimated as 0.014. On the other hand, the one-dimensional stellar structure simulation suggest the higher value of $\sim$ 0.02 (Asplund et al. 2009). This contradiction in the solar metallicity may reflect the difference between the surface and bulk composition. Thus, it might affect our understanding of the stellar evolution theory.

Impact on the planet survey. Moreover, the effect of the pollution is left on the stellar surface. If the pollution is detectable by observation and is caused by the cold accretion with planet formation, the pollution tells us the existence of planet. Thus, the polluted surface composition may help to detect the planet in the future planet survey.

Solar surface composition anomaly. The pollution mechanism can be the solution for the anomaly of the solar surface composition. Recently it has been found by Meléndez et al. (2009) that our Sun has a peculiar composition compared to the solar twins, which are the stars with the almost identical spectra and metallicity to the Sun [3]. They analyzed 11 solar-twins and found that the Sun is depleted in the refractory elements, which are the elements with the high ($\gtrsim 1200$ K) condensation temperature by at most 0.04 dex($\simeq 10\%$) as shown in Fig. 1.5[4]. Therefore, the Sun is a peculiar star among the solar-twins. Ramírez et al. (2009) analyzed another 22 solar-twins and they found some solar-twins also have the solar-like composition. However, they estimated the fraction of such a star to be about $\simeq 15\%$.

Meléndez et al. (2009) discussed both the primordial and acquired origins of this peculiar trend. In the primordial hypothesis, the protosolar nebula was originally depleted in the refractory elements (e.g., due to Galactic evolution, supernova pollution, radiation pressure), whereas in the acquired hypothesis, the refractory elements are depleted within the solar system. In the latter hypothesis, it is assumed that the refractory elements were set aside in the terrestrial objects and the accreting material onto the young sun was depleted in the refractory elements. By estimating the effects qualitatively, Meléndez et al. (2009) concluded that the latter is preferable. Moreover, Chambers (2010) has quantitatively shown that adding the total mass of the rocky material in the solar system ($\sim 4\ M_\oplus$) to the solar surface convective zone is sufficient to match the compositions of the Sun and solar twins.

However, we have to take into account the evolution of the surface convective zone. In the classical model, it shrinks to be 0.1 $M_\odot$ at ~ 30 Myr. On the other hand, the planet formation takes place within the disk lifetime, which is typically ~ 6 Myr (Haisch et al. 2001). Thus, while the planet formation occurs, the surface convective zone is quite deep in the classical model.

[3] Although the definitions of the terms of solar-type stars, solar-analog stars and solar twins are not strictly defined, we follow the definitions in Meléndez et al. (2009):

- solar-type stars: stars with spectrum type of late F to early K
- solar-analog stars: G0–G5 dwarfs
- solar twins: stars with almost identical spectra to the Sun

Note that there are some other definitions. For example, some people define solar-type stars as from 0.7 to 1.3 $M_\odot$ MS stars.

[4] Before their study, the chemical composition of the Sun was regarded as the typical due to the relatively large ($\gtrsim 0.05$ dex) systematic errors (Gustafsson 2008).

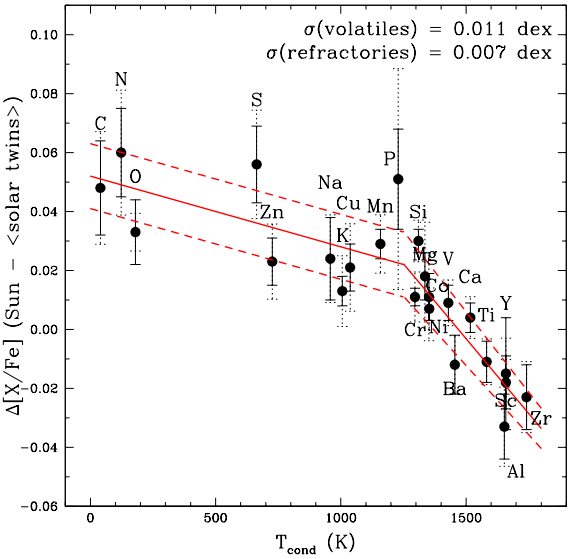

Figure 1.5: Chemical abundances of the Sun compared to those of solar twins as a function of the condensation temperature after Meléndez et al. (2009). The Sun is abundant in the volatile elements whereas less abundant in the refractory elements compared to the solar twins by about 0.04 dex, i.e. $\sim 10\%$.

Even if the accreting material is depleted in the refractory elements, it is mixed within the entire star and then its effect is much weakened. Therefore, we have to confirm that the early shrinkage of the surface convective zone happens.

Although the internal structure evolution in the cold accretion has a big impact, it has been investigated under only one setting so far. Therefore, we have not confirmed the age of the convective zone shrinkage and understood the dependence on the settings such as the mass accretion rate, the initial condition, and so on.

1.3 Purpose of this study

In this thesis, we investigate the PMS evolution in a comprehensive way. We simulate the PMS evolution particularly focusing on the internal structure evolution under a variety of settings and clarify the dependence on the conditions such as the mass accretion rate, the initial condition, the composition, the heat (entropy) injection efficiency by the accreting material, and the final mass. By compiling the results, we constrain the condition that the surface convective zone shrinks before the disk lifetime.

This thesis is organized as follows. In chapter 2, we describe the relevant physics to the PMS evolution, the input parameters and the computational method. In chapter 3, we described the

detailed examination of the PMS evolution with cold accretion. We conduct many calculations with changing the settings and explore the dependence on them. In chapter 4, we discuss the validity of the cold accretion and implication for the stellar surface composition including our Sun.

Chapter 2

Method

In this study we calculate the Pre-Main-Sequence (PMS) star's evolution with a stellar evolution code MESA including accretion (Modules for Experiments in Stellar Astrophysics, Paxton et al. 2011, 2013). In this chapter, we describe the basic physics in the stellar evolution and the computational method and settings relevant to this study. In particular, the accreting material's entropy and the chemical composition are important. We refer the reader to the Paxton et al. papers for the full details of the computational method.

2.1 Basic Equations

The following five stellar structure equations express the evolution of a spherically symmetric, non-rotating, single gaseous star without strong magnetic fields:

$$\frac{\partial r}{\partial m} = \frac{1}{4\pi r^2 \rho} \ , \tag{2.1}$$

$$\frac{\partial P}{\partial m} = -\frac{Gm}{4\pi r^4} - \frac{1}{4\pi r^2}\frac{\partial^2 r}{\partial t^2} \ , \tag{2.2}$$

$$\frac{\partial l}{\partial m} = \varepsilon_{\rm nuc} - T\frac{\partial s}{\partial t} + \varepsilon_{\rm add}, \tag{2.3}$$

$$\frac{\partial T}{\partial m} = -\frac{GmT}{4\pi r^4 P}\nabla \ , \tag{2.4}$$

$$\left(\frac{\partial X_i}{\partial t}\right)_m = \frac{m_i}{\rho}\left(\sum_j r'_{ji} - \sum_k r'_{ik}\right) + \frac{\partial}{\partial m}\left(D\frac{\partial X_i}{\partial m}\right) \ , \tag{2.5}$$

where ρ, P, l and T indicate density, pressure, luminosity and temperature, respectively. These are the equations of continuity, motion, energy, heat transport and chemical composition, re-

spectively. The spatial independent variable is the Lagrangian mass coordinate m [1], instead of the distance from the center r. This is because, in general, the radius can change rapidly with time, while the spatial coordinate of a given mass element does not vary and then we do not need to calculate the advection term, except for the stars changing their mass. In the rest of this section, we describe the meanings of these equations.

Equation of continuity

The mass in the shell of thickness dt at a given time t_0, $dm(r, t_0)$, is given by $4\pi r^2 \rho(r, t_0) dr$. Thus,

$$\frac{\partial m}{\partial r} = 4\pi r^2 \rho \ . \tag{2.6}$$

In the Eulerian description, the mass flow out of the shell due to a radial velocity v in the outward direction in the time interval dt is given by

$$\frac{\partial m}{\partial t} = -4\pi r^2 \rho v \ . \tag{2.7}$$

Differentiating Eq. (2.6) and (2.7) with respect to t and r respectively, one obtains the continuity equation of hydrodynamics in the case of spherical symmetry:

$$\frac{\partial \rho}{\partial t} + \frac{1}{r^2}\frac{\partial (\rho r^2 v)}{\partial r} = 0 \ . \tag{2.8}$$

In the Lagrangian description, mass is the independent variable. The transformation between the partial derivatives in the two spatial coordinates, r and m, is given by

$$\begin{aligned} \frac{\partial}{\partial m} &= \frac{\partial r}{\partial m}\frac{\partial}{\partial r} \ , \\ \left(\frac{\partial}{\partial t}\right)_m &= \left(\frac{\partial}{\partial t}\right)_r + \frac{\partial}{\partial r}\left(\frac{\partial r}{\partial t}\right)_m \ . \end{aligned} \tag{2.9}$$

The two subscripts indicate which of the spatial variables (m or r) is constant. From the derivative of m by the first of Eq. (2.9), we obtain the continuity equation in the Lagrangian description as Eq. (2.1).

[1] Sometimes our mass function m is denoted by $M_{\rm r}$. In this thesis, we basically follow the description in Kippenhahn & Weigert (1990).

Equation of motion

With our assumptions (gases stars without rotation, magnetic fields and close companions), there are only two forces: due to gravity and to the pressure gradient. The Eulerian motion equation,

$$\rho \left(\frac{\partial^2 r}{\partial t^2} \right)_m = -\frac{\partial P}{\partial r} - \rho \frac{Gm}{r^2} \ , \tag{2.10}$$

can be transformed to the Lagrangian form (Eq. 2.2) with Eq. (2.9).

We shall assume that the inertial term is negligible, i.e., assume *hydrostatic equilibrium*. In the nearly hydrostatic static stars, the timescales of both gravity and the pressure gradient are almost the same. This timescale is only determined by the mean density. For example, in the case of the Sun it is surprisingly small and about 30 minutes, while even in the case of PMS stars or red giants with 1 $M_\odot$ and 100 $R_\odot$ it is about only 20 days. Since these values are much smaller than the stellar evolutional timescale and we do not focus on the oscillation in this study, the inertial term can be neglected.

Equation of energy

The difference of the energy fluxes between the inner and outer edges of the shell at the mass coordinate m with mass dm is given by $l(m + dm) - l(m) \simeq (\partial l/\partial m)dm$. This energy flux difference must be equal to the energy generation or absorption rate in the shell. In PMS and MS stars, energy can be generated or absorbed by the thermonuclear reaction and the change of the internal energy [2]. Here we call the thermonuclear energy generation rate per unit mass $\varepsilon_{\rm nuc}$ and the energy generation rate by the internal energy change $\varepsilon_{\rm grav} \equiv -T\partial s/\partial t$. Moreover, in the accreting star, the extra energy per unit mass $\varepsilon_{\rm add}$, which is defined in Sec. 2.6, can be carried into the star. Thus, we obtain Eq. (2.3): $\partial l/\partial m = \varepsilon_{\rm nuc} + \varepsilon_{\rm grav} + \varepsilon_{\rm add}$.

Integration of Eq. (2.3) over the entire star represents the energy conservation law. The star's total energy, $E_{\rm tot}$ is given by

$$E_{\rm tot} = E_{\rm int} + E_{\rm g} \ , \tag{2.11}$$

where $E_{\rm int} \equiv \int_0^{M_\star} u \ {\rm d}m$ and $E_{\rm g} \equiv -\int_0^{M_\star} (Gm/r) \ {\rm d}m$ are the internal energy and the gravitational energy of a star. From the Virial theorem, in the star constructed with monoatomic

[2] Since neutrino has the mean free path much larger than the stellar radius, it has nothing to do with the stellar evolution in PMS and MS stars. Therefore we exclude the neutrino energy loss rate from the thermonuclear energy generation rate.

perfect gas,

$$E_{\rm tot} = \frac{1}{2}E_{\rm g} = -E_{\rm int} \ . \tag{2.12}$$

Note that the total energy of a star in the quasi-static state is negative. Here we rewrite the change rate of the energy using the specific energy change rate $\varepsilon_{\rm grav} = -T\partial s/\partial t$. From the first law of the thermodynamics,

$$\varepsilon_{\rm grav} = -\frac{\partial u}{\partial t} + \frac{P}{\rho^2}\frac{\partial \rho}{\partial t} \ . \tag{2.13}$$

Integration of this equation over the entire star gives the total amount of the energy stored or released in the star per unit time. We define it as

$$L_{\rm grav} \equiv \int_0^{M_\star} \varepsilon_{\rm grav} dm \ . \tag{2.14}$$

The integral of the first term in the right-hand side (RHS) of Eq. (2.13) over mass corresponds to $-dE_{\rm int}/dt$, while that of the second term gives $-dE_{\rm g}/dt$ if the time derivative of the surface pressure can be neglected. Therefore, we obtain

$$L_{\rm grav} = -\frac{{\rm d}E_{\rm int}}{{\rm d}t} - \frac{{\rm d}E_{\rm g}}{{\rm d}t} = -\frac{{\rm d}E_{\rm tot}}{{\rm d}t} \ . \tag{2.15}$$

The total energy varies via radiative cooling, nuclear burning, and accretion, given by

$$\frac{{\rm d}E_{\rm tot}}{{\rm d}t} = -L_\star + L_{\rm nuc} - L_{\rm acc} + L_{\rm add} \ , \tag{2.16}$$

where $L_\star = \int_0^{M_\star} l \, {\rm d}m$ is the bolometric luminosity, $L_{\rm nuc} = \int_0^{M_\star} \varepsilon_{\rm nuc} \, {\rm d}m$ is the energy production rate by nuclear fusion. $L_{\rm acc} = GM_\star \dot{M}/R_\star$ and $L_{\rm add} = \int_0^{M_\star} \varepsilon_{\rm add} \, {\rm d}m$ correspond to the gravitational and the heat injection by the accreting materials. Therefore,

$$E_{\rm tot}(t) = E_{\rm tot}(t=0) + \int_0^t \left(-L_\star + L_{\rm nuc} - L_{\rm acc} + L_{\rm add}\right) dt' \ . \tag{2.17}$$

Substituting Eq. (2.13), this is rewritten as

$$\int_0^t \left(-L_{\rm grav} - L_\star + L_{\rm nuc} - L_{\rm acc} + L_{\rm add}\right) dt' = 0 \ . \tag{2.18}$$

Equation of heat transport

The temperature gradient, $\partial T/\partial m$, depends on the energy transport mechanism, which can be radiation and/or convection. Here we define the temperature gradient as a function of pressure as $\nabla \equiv \mathrm{d}\ln T/\mathrm{d}\ln P$. Since ∇ is given by the mixing-length theory (MLT) as described in Sec. 2.2.1, the temperature gradient, $\partial T/\partial m$, is given by Eq. (2.3) and the MLT scheme.

Equation of chemical composition

The chemical composition of the star changes with time due to the thermonuclear reaction and the diffusion process. Hence, the evolution of the chemical composition is expressed by Eq. (2.5), where X_i is the mass fraction of the nuclei i, and m_i the mass of a nucleus i, r'_{ij} the thermonuclear reaction rate per unit volume and time that transform nuclei from the element i to j, and D the diffusion coefficient.

2.2 Input physics

In order to solve the set of equations, Eq. (2.1)–(2.5), the following closures as a function of P, T and X_i are needed: the equation of state (EoS) which gives the density ρ, the mixing length theory (MLT) which gives the temperature gradient ∇, the Rosseland mean opacity (including conduction) κ_{R}, the thermodynamic properties (e.g., the specific heat, the adiabatic temperature gradient, etc.), and the nuclear reaction rates. Since in this thesis we focus on the evolution and internal structure of the accreting PMS stars, the MLT, the opacity table and the thermonuclear reactions are particularly important. In this section we describe them in detail.

2.2.1 Convection

A fluid is convectively unstable if a fluid element keeps moving upward due to a certain upward perturbation, and vice versa. This is realized if the density of the element is lower than that of the environment. The lower density of the element drives the upward motion due to the buoyancy. This is expressed as

$$\left(\frac{\partial \rho}{\partial r}\right)_{\mathrm{e}} < \left(\frac{\partial \rho}{\partial r}\right)_{\mathrm{a}} , \tag{2.19}$$

where the subscripts e and a indicate the element's and the ambient value. If the inequality is satisfied, the convection does not occur. In the case of the ideal gas with a homologous chemical

composition, the the convective stability can be transformed to the Schwarzschild criterion:

$$\nabla_{\rm rad} < \nabla_{\rm ad} \ , \tag{2.20}$$

the radiative and adiabatic temperature gradients are given as

$$\nabla_{\rm rad} = \frac{3}{64\pi\sigma_{\rm SB}G}\frac{\kappa_{\rm R} l P}{m T^4} \ , \tag{2.21}$$

$$\nabla_{\rm ad} = -\frac{P}{T\rho c_P}\left(\frac{\partial \ln \rho}{\partial \ln T}\right)_P \ , \tag{2.22}$$

where $\sigma_{\rm SB}, \kappa_{\rm R}$ and c_P are the Stefan-Boltzmann constant, the Rosseland mean opacity and the specific heat at constant pressure. Since $\nabla_{\rm ad} = \gamma/(\gamma - 1)$ in the case of an ideal gas, the adiabatic temperature gradient does not change largely in the entire star. On the other hand, the radiative temperature gradient $\nabla_{\rm rad}$ changes significantly and the precise determination of $\nabla_{\rm rad}$ is required to the quantitative estimation of the convective region. Thus, the opacity is important for the convective region in this study and described in Sec. 2.2.2.

Note that using the entropy, s, the convective stability is also equivalent to [3]

$$\frac{\partial s}{\partial m} > 0 \ . \tag{2.23}$$

The radial gradient of the chemical composition on the convection affects the convective stability (i.e., the Ledoux criterion). For example, if the mean molecular weight of the accreting material is lower than that of the stellar surface, the convective stability will be enhanced and the so-called semiconvection occurs. Although this effect is important, in this study the accreting material's composition is assumed to be constant with time and we do not consider it.

In order to determine the temperature gradient ∇, we use the mixing length theory (MLT) of Henyey et al. (1965). In MLT, the typical length of the motion of convective cells (the mixing length) is assumed to be $\alpha_{\rm MLT} H_{\rm p}$, where $H_{\rm p} = -dr/(d \ln P)$ is the pressure scale hight and $\alpha_{\rm MLT}$ is a free parameter typically ranging $\sim$ 1–2. Although basically $\nabla = \nabla_{\rm rad}$ in the radiative region and $\nabla = \nabla_{\rm ad}$ in the adiabatic region, at the upper region of the convective zone, the temperature gradient deviates from $\nabla_{\rm ad}$. This is so-called superadiabatic region and the MLT is needed to determine the temperature gradient there.

The convective mixing of elements is treated as a diffusive process and the diffusion coefficient D in Eq. (2.5) is also calculated by the MLT. In addition to the standard convective mixing,

[3] This is derived from Eq. (2.19) with the Maxwell's relations.

we include overshooting, which express the effect that the convective parcel is not stopped just at the Schwarzschild boundary and penetrates the radiative region. Here we use the scheme of Herwig (2000), in which the diffusion coefficient exponentially approaches zero in the radiative zone from the Schwarzschild boundary. The diffusion coefficient, $D_{\rm ov}$, is modeled as

$$D_{\rm ov} = D_0 \exp\left(\frac{-2z}{f_{\rm ov} H_p}\right) , \tag{2.24}$$

where the D_0 is the diffusion coefficient from MLT at the boundary, z is the distance from the boundary, $f_{\rm ov}$ is a free parameter (more properly, the ratio of the pressure scale height, H_p, to the scale height of the velocity field).

2.2.2 Opacity

As described in the previous section, opacity is important for the boundary between the convective and radiative regions. Therefore, we need to take in the opacity tables in the stellar evolution calculation. Although there are four types of opacity (for radiation, the electron conduction, the Compton scattering and the electron scattering), in low-mass PMS and MS stars, only the radiative and the electron conduction opacity are relevant.

In this study we use the radiative opacity of the "Opacity Project" (OP, Seaton 2005) and the Wichita group (FERG, Ferguson et al. 2005) for the lower temperature than $10^{4.5}$ K. In the high density region, the opacity is dominated by the electron conduction [4] . The electron conduction opacity of Cassisi et al. (2007) is used.

Figure 2.1 shows an example of the opacity profile as a function of temperature higher than 10^4 K. Since the opacity is the sum of the absorption by many nuclei, there are some bumps. In particular, the κ-bump around ~ 2–3×10^6 K, which is made by the absorption by carbon, oxygen, neon and iron nuclei, determines the boundary between the surface convective zone and the radiative core of low-mass PMS and MS stars. Below this temperature the large opacity results in the large $\nabla_{\rm rad}$ and then the convection occurs, while the region with the higher temperature is radiative due to the small $\nabla_{\rm rad}$.

[4] The radiative luminosity, $L_{\rm rad}$ and the luminosity by the heat conduction by electron, $L_{\rm cond}$ are given by

$$L(r) = L_{\rm rad}(r) + L_{\rm cond}(r) = -4\pi r^2 \frac{4ac}{3\rho}\left(\frac{1}{\kappa_{\rm R}} + \frac{1}{\kappa_{\rm cond}}\right) T^3 \frac{{\rm d}T}{{\rm d}r},$$

where a is the radiation constant, c is the light speed, and $\kappa_{\rm cond}$ is the heat conduction opacity. When $\kappa_{\rm cond} < \kappa_{\rm R}$, the energy transport by heat conduction is important.

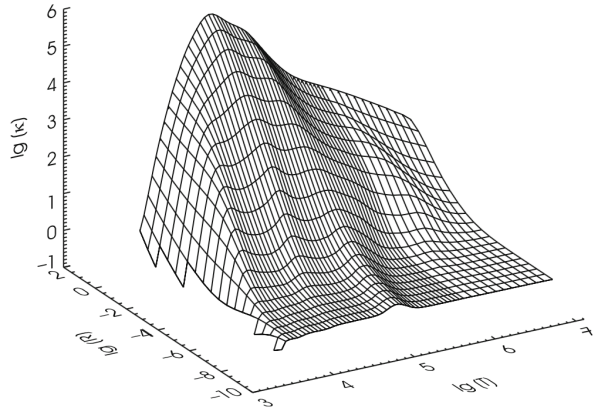

Figure 2.1: The OPAL radiative opacity κ as a function of temperature and $R = \rho/(T/10^6 \text{ K})^3$ after Fig. 17.6 of Kippenhahn et al. (2012). The bump around 2–3 $\times 10^6$ K determines the boundary between the surface convective zone and the radiative core of the low-mass stars.

2.2.3 Thermonuclear reactions

The thermonuclear reactions important in stellar evolution because they produce energy and affect the internal structure. In this section we describe the thermonuclear reactions relevant to this study.

The nuclei in the high temperature gas penetrate the Coulomb potential at the low possibility by the tunneling effect. Since the high energy elements at the high-end of the Maxwell distribution is important, this reaction is called thermonuclear reaction. The nuclear reaction rate per unit volume and time between the nuclei i and j, r_{ij}, is given by

$$r_{ij} = \frac{1}{1+\delta_{ij}} n_i n_j \langle \sigma v \rangle \ , \tag{2.25}$$

where δ_{ij}, n_i, σ and v is the Kronecker delta ($\delta_{ij} = 1$ if $i = j$, otherwise 0), the number density of element i, the cross-section, and the relative velocity. $\langle\ \rangle$ is the average over the energy under the Maxwell distribution. The energy production rate per unit volume and time is $r_{ij} q_{ij}$, where q_{ij} is the released energy per reaction. Therefore, the energy production rate per unit mass and time, $\varepsilon_{\rm nuc}$ which appears in Eq. (2.3), is given by

$$\varepsilon_{\rm nuc} = \frac{1}{1+\delta_{ij}} \frac{X_i X_j \rho}{m_i m_j} \langle \sigma v \rangle q_{ij} \ . \tag{2.26}$$

Note that $\varepsilon_{\rm nuc}$ is proportional to the density and the mass fraction of each element, and in general $\langle \sigma v \rangle$ is a complex function of temperature. This is because it is mainly determined by the product of the Maxwell distribution and the penetration probability through the Coulomb

barrier (so-called "Gamow peak") and sometimes affected by resonance. In MESA, the reaction rate and the energy per reaction is given by Caughlan & Fowler (1988) and Angulo et al. (1999, "NACRE").

Since we calculate the PMS evolution of low- and intermediate-mass stars, the relevant thermonuclear reactions to this study are deuterium (D), lithium (Li), and hydrogen (H) burning. In particular, the deuterium burning is the most important reaction for the PMS evolution.

Deuterium burning

Deuterium fusion occurs at the temperature above $\sim 10^6$ K. The reaction is as follows:

$$\mathrm{D} + {}^1\mathrm{H} \rightarrow {}^3\mathrm{He} + q_\mathrm{D} \ . \tag{2.27}$$

This reaction produces the energy $q_\mathrm{D} = 5.494$ MeV. With the mass fraction of deuterium, X_D, the number of deuterium atoms per gram is $X_\mathrm{D}/2.014 m_\mathrm{amu}$. Therefore, the total energy available from deuterium burning per gram, Q_D, is given by

$$Q_\mathrm{D} = q_\mathrm{D} X_\mathrm{D}/2.014 m_\mathrm{amu} = 5.26 \times 10^{13} \ \mathrm{erg/g} \left(\frac{X_\mathrm{D}}{2 \times 10^{-5}} \right) \ . \tag{2.28}$$

The total energy available from deuterium burning in the entire star, E_D, is

$$E_\mathrm{D} = M_\star Q_\mathrm{D} = 1.05 \times 10^{47} \ \mathrm{erg} \left(\frac{X_\mathrm{D}}{2 \times 10^{-5}} \right) \left(\frac{M_\star}{M_\odot} \right) \ . \tag{2.29}$$

As shown in Eq. (2.26), the reaction rate of deuterium burning is proportional to the density, hydrogen and deuterium abundance, and the averaged cross section as a function of temperature. The energy generation rate by deuterium fusion, ε_D, is given by

$$\varepsilon_\mathrm{D} \propto X_\mathrm{D} \, \rho \, T^{\nu_\mathrm{D}} \ . \tag{2.30}$$

Although ν_D depends on the temperature, typically $\nu \sim 11.8$ around 10^6 K (Stahler & Palla 2005). This strong dependence on the temperature is an important feature of deuterium burning.

Lithium burning

Lithium fusion occurs at the temperature above $\sim 3 \times 10^6$ K. The reaction is as follows:

$${}^7\mathrm{Li} + {}^1\mathrm{H} \rightarrow 2 \, {}^4\mathrm{He} \ . \tag{2.31}$$

This reaction is a part of the second branch of the pp chain. The energy produced by this reaction is 17.34 MeV [5]. The number abundance of ^{7}Li in the interstellar medium is measured to be $(\mathrm{Li/H})_{\mathrm{ISM}} = 2 \times 10^{-9}$ (Stahler & Palla 2005), which corresponds to the mass fraction $X_{\mathrm{Li}} \sim 1 \times 10^{-8}$. Therefore, the total energy available from the lithium burning in the entire star is about three orders of magnitude less than that from deuterium burning due to the small abundance, and then the energy production of the lithium burning can be neglected in the PMS evolution. However, if the lithium fraction of a young star is measured by the spectroscopic observation, it can be the indicator of the evolutional degree (e.g., Soderblom et al. 2014).

Hydrogen burning

Hydrogen fusion is basically the conversion of four protons to one helium nucleus:

$$4\,^1\mathrm{H} \rightarrow\ ^4\mathrm{He} + 2\,\mathrm{e}^+ + 2\,\nu\ . \tag{2.32}$$

There are two different chains of reactions. One is the proton-proton (pp) chain which occurs at the temperature above about 8×10^6 K [6] . The other is the CNO cycle which dominates in the higher temperature, $\gtrsim 1.5 \times 10^7$ K.

The pp chain's sensitivity to the temperature is not relatively strong, namely $\nu_{\mathrm{pp}} = 6$ at 3.5×10^6 K and 3.5 at 2.0×10^7 K, where $\varepsilon_{\mathrm{nuc,pp}} \propto T^{\nu_{\mathrm{pp}}}$. On the other hand, in the CNO cycle, it is 23–13 for 1.0–5.0$\times 10^7$ K (e.g., Kippenhahn & Weigert 1990). Thus, the CNO cycle also has the strong temperature sensitivity as in the case of deuterium burning.

2.3 Input parameters

There are free parameters for convection (α_{MLT} and f_{ov}) and the initial composition $X_{\mathrm{ini}}, Y_{\mathrm{ini}}$ and Z_{ini} which are the mass fractions of hydrogen (including deuterium), helium (both ^{3}He and ^{4}He) and metals, respectively. We choose the input parameters which reproduce the present Sun's values estimated by the helioseismic and spectroscopic observation.

The present solar radius and luminosity $R_\odot = 6.9598 \times 10^{10}$cm and $L_\odot = 3.8418 \times 10^{33}$ erg/s, respectively (Bahcall et al. 2005). From helioseismic analyses, the solar convective zone radius and the surface helium abundance are determined to be $R_{\mathrm{CZ}} = 0.713 \pm 0.001\ R_\odot$ and $Y_{\mathrm{surf}} = 0.2485 \pm 0.0035$, respectively (Bahcall et al. 2005, Basu & Antia 2004, and references therein).

[5] Mass of ^{1}H, ^{7}Li and ^{4}He are 1.00782503, 7.016003 and 4.00260323 m_{amu}, respectively. Using $m_{\mathrm{amu}}c^2 = 931.49$ MeV, the energy difference is 17.34 MeV in the reaction ^{7}Li(p,α)α.

[6] The pp chain is named after its first reaction ($\mathrm{p} + \mathrm{p} \rightarrow \mathrm{D} + \mathrm{e}^+ + \nu$) because this is the bottleneck (i.e., the slowest) reaction.

Table 2.1: Input parameters.

Quantity	Value
Converged Input Parameter	
$X_{\rm ini}$	0.7004553948
$Y_{\rm ini}$	0.2794811789
$Z_{\rm ini}$	0.0200634263
$\alpha_{\rm MLT}$	1.9050629261
$f_{\rm ov}$	0.0119197042
Properties of Converged Model	
$(Z/X)_{\rm surf}$	0.0253437100
$Y_{\rm surf}$	0.2533888539
$R_{\rm CZ}/R_\odot$	0.7127577753
$R_\star/R_\odot$	1.0000028225
$L_\star/L_\odot$	1.0000011373
$T_{\rm eff}$ [K]	5776.0231979
Target Values	
$(Z/X)_{\rm surf}$[a]	0.02313
$Y_{\rm surf}$[b]	0.2485 ± 0.0035
$R_{\rm CZ}/R_\odot$[c]	0.713 ± 0.001
$R_\odot$ [cm][c]	6.9598×10^{10}
$L_\odot$ [erg/s][c]	3.8418×10^{33}
$T_{\rm eff}$ [K]	5777

Notes. [a] Grevesse & Sauval (1998), [b] Basu & Antia (2004), [c] Bahcall et al. (2005).

The ratio of heavy element to hydrogen abundance on the solar surface, $(Z/X)_{\rm surf}$, is 0.02313 from spectroscopic analyses (Grevesse & Sauval 1998). Although the solar metallicity remains a matter of debate (see Asplund et al. 2009)[7], it is beyond the scope of this paper.

We have performed a χ^2 test to find the best initial settings using the "Nelder-Mead simplex algorithm" (Nelder & Mead 1965). The input parameters are the initial composition, the mixing-length parameter, $\alpha_{\rm MLT}$, and the overshoot mixing parameter, $f_{\rm ov}$ (Herwig 2000, Paxton et al. 2011). We calculate the 1 $M_\odot$ star's evolutions from PMS phase with changing these parameters to minimise the χ^2 value at the solar age. We assumed that the solar age is 4.567 Gyr after the star formation completes. The detailed composition used in the test is described in the following section. The results of the χ^2 test listed in Table 2.1 are used as the initial conditions in this paper.

[7]Using three-dimensional atmosphere model, the solar metallicity at the atmosphere is estimated to be $\sim$ 0.0134, which is reduced from the classical value (~ 0.02) by about 70%.

2.3.1 Chemical composition

In this thesis, we use the metal composition of Grevesse & Sauval (1998). This metal fraction and the metallicity in the Table 2.1 result in the ^{7}Li mass fraction $X_{\rm Li} = 1.2 \times 10^{-8}$, which is close to the interstellar value 1×10^{-8} (see Sec. 2.2.3). We assume that ^{3}He/^{4}He $= 10^{-4}$, which is similar to the value in the Jovian atmosphere as described below. Although $X_{\rm D}$ is usually set to be 20 ppm in mass, it remains uncertain as described below. The composition of the accreting material is assumed to be the same as the initial one.

(D/H) and ^{3}He/^{4}He in the presolar nebula

The present-day amount of ^{3}He and deuterium is changed from the primordial protosolar value by deuterium fusion, D(p,γ)^{3}He. Therefore, these values are indirectly inferred from observations of the Jupiter (e.g., Asplund et al. 2009). The fraction of ^{3}He/^{4}He in Jupiter's atmosphere is measured to be 166 ± 5 in parts per million (ppm) by the Galileo Probe Mass Spectrometer measurements (Mahaffy et al. 1998).

The number fraction of deuterium and light hydrogen in the protosolar nebula, $({\rm D/H})_{\rm PSN}$, is measured by two methods. First, the observation of hydrogen molecules (H_2 and HD) in the Jovian atmosphere by the Infrared Space Observatory gives $({\rm D/H})_{\rm PSN} = 21 \pm 4$ ppm with the correction concerning the enhancement of (D/H) ratio during planet formation[8] (Lellouch et al. 2001). Secondly, $({\rm D/H})_{\rm PSN}$ can be estimated by the enhanced ^{3}He in the solar wind. The ^{3}He/^{4}He ratio in the solar wind ($= 453 \pm 3$ ppm by the Genesis mission) is much higher than that in the Jovian atmosphere (Heber et al. 2008). If we assume that the Jovian ^{3}He/^{4}He ratio is the same as the protosolar value and that the enhanced ^{3}He/^{4}He ratio in the solar wind results from deuterium burning, then $({\rm D/H})_{\rm PSN}$ is estimated to be 19.6 ± 0.3 ppm [9]. From these estimates, we use $({\rm D/H})_{\rm PSN} = 20 \pm 2$ ppm in this thesis (Asplund et al. 2009).

[8] The injection of icy materials with the high (D/H) ratio similar to that observed in comets (30 ppm) enhances the Jovian one (Guillot 1999).

[9] If the helium mass fraction $Y = 0.28$, then the number of ^{4}He per gram is $\sim 0.07 m_{\rm amu}^{-1}$. In the case that $X_{\rm D}$=30 ppm, the increase of ^{3}He by deuterium burning is $1.5 \times 10^{-5} m_{\rm amu}^{-1}$ per gram. Thus, deuterium burning increases the ^{3}He/^{4}He ratio by ~ 200 ppm.

(D/H) and ^{3}He/^{4}He in the interstellar medium

Deuterium was formed only in the first three minutes after the big bang [10] and then converted to helium and other metals by the nuclear fusion in the stellar interior. The primordial value, $(\mathrm{D/H})_{\mathrm{prim}}$ is measured to be 24–30 ppm with the nucleosynthesis theory and the observations by the Wilkinson Microwave Anisotropy Probe (WMAP) satellite and other cosmic microwave background (CMB) experiments (Linsky et al. 2006). $(\mathrm{D/H})_{\mathrm{prim}}$ is the upper limit of the deuterium amount.

The (D/H) ratio in the present-day interstellar medium is under debate (Prantzos 2007). The estimated values by UV observation [11] with the Far Ultraviolet Spectroscopic Explorer (FUSE) satellite suggest large differences. For example, $(\mathrm{D/H})_{\mathrm{ISM}} = 9.8 \pm 3.8$ ppm in Hébrard et al. (2005), while $(\mathrm{D/H})_{\mathrm{ISM}} \geq 23.1 \pm 2.4$ ppm in Linsky et al. (2006).

Linsky et al. (2006) evaluated 47 values of (D/H) as a function of the hydrogen column density with UV observations (see Fig. 2.2). They showed that (D/H) spreads widely from 5 to 23 ppm. Within the Local Bubble [12] , namely, the hydrogen atom number density $\log N(\mathrm{HI}) < 19.2$, (D/H) is constant to be 15.6 ± 0.4 ppm. In the intermediate region, there is a wide range of (D/H) values. For the larger hydrogen column region, (D/H) is low. They claimed that this behavior is caused by the depletion onto the dust grain in the low temperature environment. The high (D/H) within the Local Bubble is caused by supplying deuterium from dust to gas phase due to the shock. Although they concluded that $(\mathrm{D/H})_{\mathrm{ISM}} = 23.1 \pm 2.4$ ppm, there can be a large difference in each star. For example, if a star is formed by a cloud highly affected by the deuterium-free stellar wind of a late type star, then the (D/H) ratio can be significantly different from that of the neighboring stars.

Compiling the values above, we obtain the (D/H) evolution in Fig. 2.3. As described above and shown in Fig. 2.3, X_{D} can be significantly different in each star. The impact of varying X_{D} on the PMS evolution is described in Sec. 3.2.3.

[10] Deuterium is formed in a pp-chain reaction,

$$^1\mathrm{H} + {}^1\mathrm{H} \rightarrow \mathrm{D} + \mathrm{e}^+ + \nu \ . \tag{2.33}$$

However, this reaction is quite rare because hydrogen has to experience a β^+ decay. This reaction is known to be the "bottleneck" of the pp chain and then the formed deuterium is quickly destroyed. Therefore, this reaction can not be the formation process of deuterium.

[11] The Lyman-α absorptions of HI and DI are located at 1215–1216 Å.

[12] The low-density cavity in the range of ~ 100 pc. This region was formed by a supernova several million years ago (e.g., Linsky et al. 2006). The solar system is now in this region.

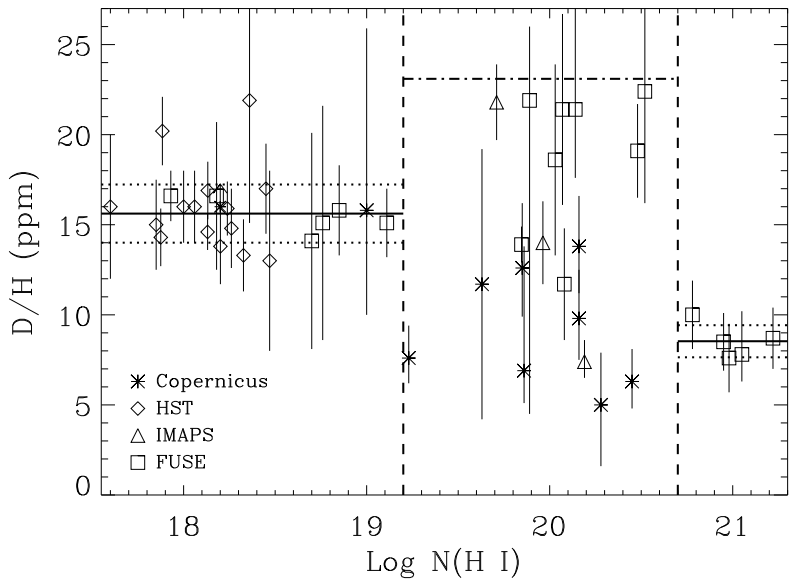

Figure 2.2: (D/H) ratio in number as a function of the distance from the solar system after Linsky et al. (2006). Inside the region where $\log N(\mathrm{HI}) < 19.2$, which indicates the Local Bubble, (D/H) is almost constant to be ~ 15.6. In this region the (D/H) ratio is almost constant. In the distant region, it is also constant to be ~ 8.5 but is lower than that in the Local Bubble. However, in the intermediate region, there is a large scatter from 5 to 23 ppm.

2.4 Initial condition

In this study we start the calculation at the point when a protostar, i.e., a second Larson's core, is formed. The envelope is still abundant and accreting vigorously.

We assume that the mass and the radius of the initial protostar are 0.01 $M_\odot$ and 1.5 $R_\odot$, respectively, as in Hosokawa et al. (2011). The radius and mass of the second Larson's core is still unclear. The currently available results by (magneto-) radiation-hydrodynamic simulation are compiled in Table 2.2.

Note that the initial structure of the protostar is constructed to be fully convective in MESA, although the hydrodynamic simulation shows that the protostar is radiative (e.g., Masunaga & Inutsuka 2000) because the entropy of accreting materials is higher than that of the stellar surface.

We discuss the impact of changing the initial condition on the evolution in Sec. 3.2.2.

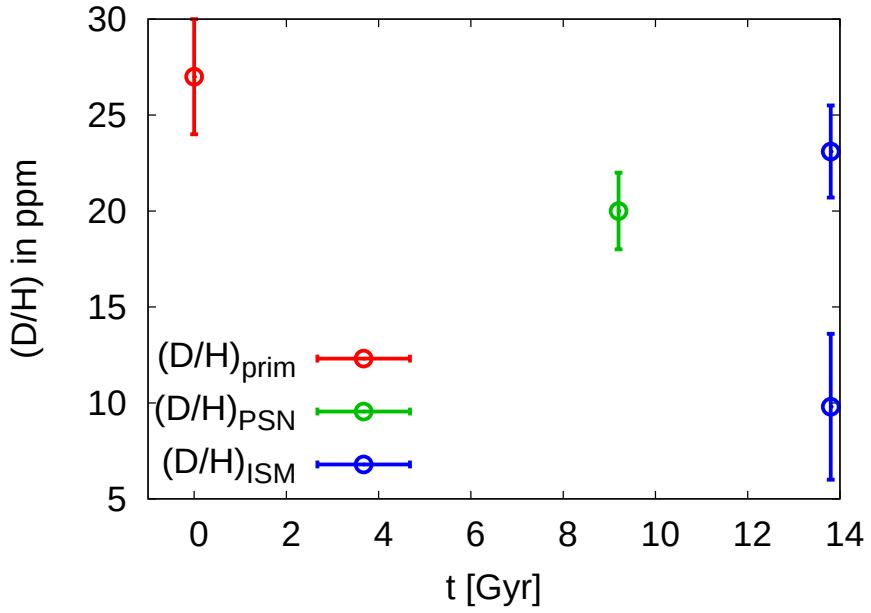

Figure 2.3: (D/H) ratio in number as a function of time. The red point indicates the primordial value (t=0) estimated with the nucleosynthesis theory and the CMB observation. (D/H) in the protosolar nebula, which is indirectly estimated by that in Jovian atmosphere and the difference between the solar and Jovian ^{3}He, is shown by the green point. (D/H) in the local interstellar medium is still a matter of debate. The high (Linsky et al. 2006) and low (Hébrard et al. 2005) values are shown by blue points.

Table 2.2: Properties of the second core.

Mass [$M_\odot$]	Radius [$R_\odot$]	Reference
0.003	~ 4.0	Masunaga & Inutsuka (2000)
0.01	3.45	Stahler et al. (1980b)

2.5 Mass accretion rate

In this study we especially focus on the effect of accretion on the PMS evolution. In this section we describe the mass accretion rate onto low-mass protostars.

During the main mass accretion phase, the accreting material is supplied by the natal cloud through free fall. Here we roughly estimate the mass accretion rate (e.g., Stahler et al. 1980a). If the magnetic field and rotation of the cloud are negligible, the cloud is supported by the thermal pressure. Thus, at the time when the gravitational collapse stars by a certain perturbation, the free-fall timescale, $t_{\rm ff} = \sqrt{3\pi/(32G\rho_0)}$ is comparable to the sound-crossing time, $t_{\rm sc} = \sqrt{R_c/c_{s,0}}$, where ρ_0, M_c and R_c denote the density, mass and radius of the cloud.

The subscript "$_0$" indicates the initial value. c_s is the isothermal sound speed given by

$$c_s = 1.85 \times 10^4 \mathrm{cm/s} \left(\frac{T}{10\ \mathrm{K}}\right)^{1/2} \left(\frac{\mu}{2.4}\right)^{-1/2} , \tag{2.34}$$

where μ is the mean molecular weight [13]. A crude estimate serves the characteristic mass accretion rate,

$$\dot{M} \sim M_c / t_{\rm ff} . \tag{2.36}$$

This is roughly evaluated as

$$\dot{M} \sim c_{s,0}^3 / G = 1.50 \times 10^{-6} M_\odot/\mathrm{yr} \left(\frac{T}{10\ \mathrm{K}}\right)^{3/2} \left(\frac{\mu}{2.4}\right)^{-3/2} . \tag{2.37}$$

For the cloud temperature in the interval from 10 to 30 K, the corresponding mass accretion rate is 2×10^{-6} to 1×10^{-5} $M_\odot$/yr.

In the case of massive star formation, the accretion rate $\sim 10^{-5} M_\odot$/yr is too low to form within its lifetime. If the gravity of the natal cloud is supported by not only thermal pressure but also magnetic pressure and turbulence as well just prior to the collapse, then the effective sound speed (pressure divided by density) can be large. If the characteristic turbulent velocity is as large as ~ 1 km/s, the mass accretion rate becomes more than 10^{-4} $M_\odot$/yr (e.g., Hosokawa & Omukai 2009, and references therein).

Although we have described the characteristic mass accretion rate, the mass accretion rate can be episodic.During the main mass accretion phase, the disk mass is larger than the central star and then the gravitational instability is caused in the disk (Inutsuka et al. 2010). The accretion of the clump formed by the gravitational instability results in the episodic variability of the mass accretion rate (e.g., Vorobyov & Basu 2010). Moreover, the larger disk mass may cause a gravo-thermal instability (Martin et al. 2012).

Therefore, the mass accretion rate can be different in each star and can be time-dependent. We explore the effect of the varying the mass accretion on the PMS evolution in Sec. sec:Mdot.

[13] The mean molecular weight is given by

$$\frac{1}{\mu} = \sum_i \frac{X_i}{A_i} , \tag{2.35}$$

where $A_i = m_i/m_{\rm H}$ is the atomic weight. In the case of the molecular gas with $X = 0.7, Y = 0.28, Z = 0.02$ and the averaged atomic weight for metals, $A_Z = 17$, $\mu \sim 2.37$.

2.5.1 Mass loss

In the main mass accretion phase, about 10% of the accreted material in mass is thought to be lost by outflow or jet. Furthermore, observations revealed that T Tauri stars have much higher mass loss rate than the Sun. Suzuki et al. (2013) suggested that the Sun at the T Tauri phase was as massive as 1.02 $M_\odot$. However, in this study we neglect the effect of mass loss.

2.6 Entropy of accreting materials

As described in Chap. 1, the accretion in which the entropy of the accreting material, $s_{\rm acc}$, is the same as that of the stellar surface, $s_\star$, is called as "cold accretion". On the other hand, $s_{\rm acc}$ can be higher than $s_\star$ as in the spherical accretion. In this study we parameterize this energy injection as

$$L_{\rm add} = \xi \frac{GM_\star \dot{M}}{R_\star}, \tag{2.38}$$

following Baraffe et al. (2009). ξ is a scaling factor up to one. As described in Sec. 1.2, we call the accretion with $\xi = 0$ "*cold accretion*" and that with $\xi > 0$ "*hot accretion*".

In Baraffe et al. (2009), $L_{\rm add}$ is distributed uniformly and instantaneously within the entire star. Although it is not unclear whether the accreting material's entropy enters the stellar interior quickly, we follow the prescription of Baraffe et al. (2009). Thus, $\varepsilon_{\rm add}$ in Eq. (2.3) is given as

$$\varepsilon_{\rm add} = L_{\rm add}/M_\star. \tag{2.39}$$

As discussed in Baraffe & Chabrier (2010), low-mass ($\lesssim 2\ M_\odot$) stars are fully convective during their PMS stage and the motion of convective parcels may deliver the entropy into the deep interior quickly. In the case of the star with a large radiative core, the convection does not transport the entropy into the star. However, another physical mechanism of transporting entropy may exist [14]. Although this may be an important issue, this is beyond the scope of this study.

[14] For example, it is recently suggested that the internal gravity wave is important for the tidal dissipation rather than the turbulent eddy viscosity in the convective zone (Barker & Ogilvie 2010). There can be a physical process to transport entropy into the deep interior.

2.7 Computational method

In this chapter we have already described the basic equations in the stellar evolution calculation, the input physics and the input parameters in this study. At last, in this section the details of the computation method is described. Although these are important for the convergence, the results are not affected by them.

2.7.1 A stellar evolution code MESA

MESA is an open source code [15] for a stellar evolution simulation written in Fortran 95. MESA combines many numerical and physical modules such as EoS, opacity, nuclear reaction rates, element diffusion data, and atmosphere boundary conditions described below. Shared memory parallelism based on OpenMP is supported. Although the current version of MESA can simulates a wide range of stellar evolution such as giant planets, massive stars, pulsating stars, accreting compact objects, etc. from the PMS to late stage, MESA is continually updated to implement a variety of new numerical or physical modules. In this study we use MESA version 6596.

The modifications and additions to MESA in order to calculate the evolution of accreting PMS stars in this study is as follows : the input parameters determined by the χ^2 test which reproduce the observed solar values (see Sec. 2.3), the addition of the extra heat by the accreting materials (Sec. 2.6) and the boundary conditions which improve the convergence (Sec. 2.7.2).

2.7.2 Boundary conditions

There are two central boundary conditions: $r(m = 0) = 0$ and $l(m = 0) = 0$. The outer boundary conditions, i.e., the pressure P_s and temperature T_s at the top of the outermost cell, are specified in the three ways in MESA: (1) interpolation of model atmosphere, (2) integration of hydrostatic equation and (3) specifying the optical depth, τ_s. We use the interpolation of the atmosphere model with $M_\star, R_\star$ and $L_\star$.

In the case of accreting star, we assume that materials accrete onto the small fraction of stellar surface from the thin disk and do not affect the photospheric condition. Therefore, we use the photospheric boundary condition in this study.

[15] http://mesa.sourceforge.net

Atmosphere tables

We found that the choice of the atmosphere table affects the convergence significantly especially in the case of accreting young stars. We chose the most stable table in this study.

In MESA, the plane parallel atmosphere is assumed, so that the surface gravity, $g = GM_\star^2/R_\star$, and the effective temperature, $T_{\rm eff} = L_\star/4\pi R_\star^2$, are relevant to the atmosphere model. We use the two model atmosphere tables. One is the photospheric table, where $\tau_s = 2/3$ and $T_s = T_{\rm eff}$. P_s is set by the two model atmospheres: PHOENIX (Hauschildt et al. 1999a,b), where $-0.5 < \log(g) < 5.5$ and 2,000 K $< T_{\rm eff} <$ 10,000 K, and ATLAS9 (Castelli & Kurucz 2004), where $0 < \log(g) < 5$ and 3,500 K $< T_{\rm eff} <$ 50,000 K.

The second table is the "$\tau_s = 100$" table, which specifies P_s and T_s at $\tau_s = 100$. This is primarily used for low-mass stars and giant planets in order to avoid the convergence problem. This consists of the two model atmospheres: ATLAS9 and COND (Allard et al. 2001). The latter atmosphere includes gravitational setting of dust elements and then the depletion of them from atmosphere. The region in which the model atmosphere is used is shown in Fig. 2.4. In the region where neither table is available, we use integration method with the *Eddington approximation* described below.

In this study, we use the "$\tau_s = 100$" table for the low-mass or small stars ($M_\star < 1\ M_\odot$ or $R_\star < 0.7\ R_\odot$) and the photosphere table for the rest. We choose this condition because the "$\tau_s = 100$" table is better for the convergence.

2.7.3 Integration of hydrostatic equation

In the integration method, the hydrostatic equation,

$$\frac{{\rm d}P_{\rm gas}}{{\rm d}\tau} = \frac{g}{\kappa} - \frac{a}{3}\frac{{\rm d}T^4}{{\rm d}\tau} \ , \tag{2.40}$$

is integrated with the optical depth, τ,

$$\frac{{\rm d}\tau}{{\rm d}r} = -\kappa\rho \tag{2.41}$$

and the *Eddington approximation* (Eddington 1926),

$$T^4(\tau) = \frac{3}{4}T_{\rm eff}^4\left(\tau + \frac{2}{3}\right) \ . \tag{2.42}$$

The second term in the right-hand side of Eq. (2.40) comes from the radiation pressure.

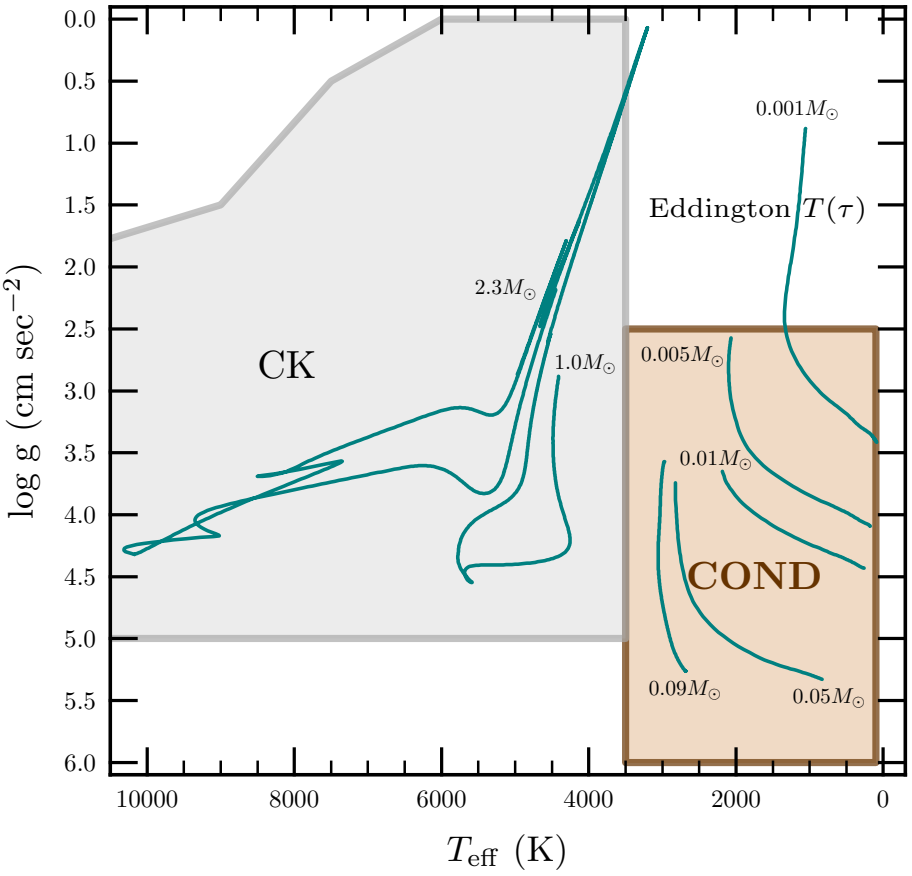

Figure 2.4: Range of model atmospheres in the "$\tau_s = 100$" table after Fig. 6 of Paxton et al. (2011). In the CK and COND region, the ATLAS9 and COND model atmosphere is used, respectively.

2.7.4 Mesh adjustment

In the case of non-accreting stars, the numerical mesh is usually fixed with time, even though sometimes cells are split or merged in order to improve convergence. The criteria for mesh adjustment in the case of non-accreting star are the difference of thermodynamics quantities, composition, the thermonuclear reaction rate, and so on.

On the other hand, in the case of the star whose mass changes with time, mesh adjustment is done at each timestep before solving the evolution. The change in the total mass is treated as the mesh size change instead of adding new cells to the surface. There are three regions in the remapping as shown in Fig. 2.5: the constant mass (Lagrangian mesh) region in the interior, the constant relative mass in the envelope and the transition region. In the inner region, the mass location of cells is not affected by the accretion. Therefore, we use the constant mesh with time and this scheme prevents advection term and the numerical mixing caused by the element transfer of elements among the cells. Here we define the relative mass dq. For the cell k, dq_k is defines as $\mathrm{d}q_k \equiv \mathrm{d}m_k/M_\star$, where d$m_k$ is the mass in the cell k. In the inner region, dq_k

is rescaled by $M_\star/(M_\star + \Delta M)$, where ΔM is the mass just accreted in the current timestep. On the other hand, in the outer region, cells are remapped to maintain $\mathrm{d}q_k$, namely the mass location is rescaled by $(M_\star + \Delta M)/M_\star$. In the intermediate region the mesh is adjusted so as to $\sum_k \mathrm{d}q_k = 1$. The composition is also changed in the outer and intermediate regions.

The Lagrangian mesh region needs to be large in order to avoid the numerical mixing. The boundary is defined by temperature and mass. The base of the outer region is located at $T = 10^5$ K. The top of the inner region is defined by the larger mass of the two criteria: $T = 10^6$ K and $m = 0.99 M_\star$ [16].

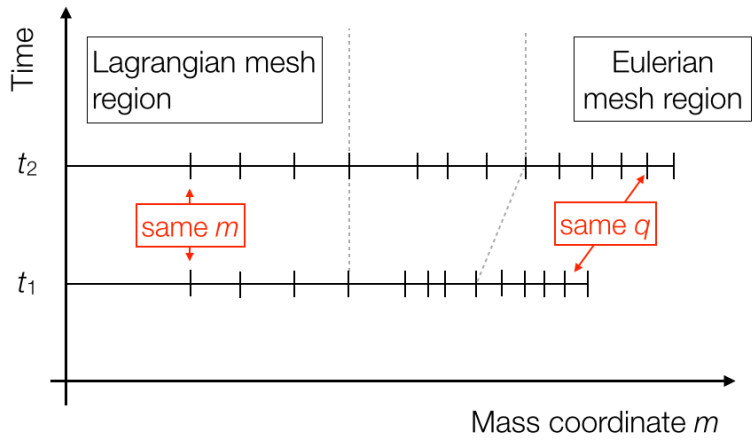

Figure 2.5: A schematic picture of how mesh is constructed in the accreting star.

2.7.5 Evaluation of $\varepsilon_{\mathbf{grav}}$

The evaluation of $\varepsilon_{\mathrm{grav}}$ needs careful a consideration in the accreting star. The accreting material at the surface does not exit in the previous timestep and then the time difference of its entropy cannot be directly evaluated.

Before version 5527, MESA used the "compressional heating" (Townsley & Bildsten 2004). In this scheme, the mass accretion timescale, $t_{\dot{M}} = \Delta M/\dot{M}$, is assumed to be much longer than the thermal timescale, $t_{\mathrm{th}} = c_P T \Delta M/L_\star$. In other words, it is assumed that the accreting

[16] The latter is not the default setting. In our study the mass accretion rate is intense and this setting improves the convergence.

material is thermally well relaxed with the environment quickly and that the accretion is not adiabatic but quasi-steady. In this case, the leak of heat of the accreting materials is able to affect the environment and to be used to evaluate $\varepsilon_{\rm grav}$. However, the assumption, $t_{\dot{M}} \gg t_{\rm th}$, is not valid in this study due to the intense mass accretion rate [17].

A new scheme was implemented in version 5527 [18]. In this scheme the star is divided into three regions: the Lagrangian region in the interior, the Eulerian region in the surface and the transition region in the middle. Note that these regions are independent of those used to mesh adjustment in Sec. 2.7.4.

Lagrangian scheme

In the deep interior, we use the Lagrangian mass coordinate as usual. Straightforwardly, $\varepsilon_{\rm grav}$ is evaluated by

$$\varepsilon_{\rm grav} = -T\left(\frac{\partial s}{\partial t}\right)_m = -T\left(\frac{s_{\rm new} - s_{\rm pre}}{\Delta t}\right)_m , \tag{2.43}$$

where $s_{\rm new} - s_{\rm pre}$ are the entropy change in a time step. However, since the difference in a time step can be extremely small, this scheme can produce the round-off error for the estimation of $\varepsilon_{\rm grav}$. In order to reduce it, we transform Eq. (2.43) using the basic thermodynamic variables [19]:

$$\varepsilon_{\rm grav} = -Tc_P\left[\left(1 - 4\nabla_{\rm ad}\frac{P_{\rm rad}}{P}\right)\left(\frac{\partial \ln T}{\partial t}\right)_m - \nabla_{\rm ad}\frac{P_{\rm gas}}{P}\left(\frac{\partial \ln P_{\rm gas}}{\partial t}\right)_m\right] . \tag{2.44}$$

This equation can be derived with radiation pressure, $P_{\rm rad} = aT^4/3$ ($P = P_{\rm gas} + P_{\rm rad}$), and the first law of thermodynamics, $T{\rm d}s = c_V T + P{\rm d}\rho/\rho^2$. Note that $\varepsilon_{\rm grav}$ is the first order time derivative.

Eulerian scheme

Secondly, in the stellar surface, we have the new cells which do not exist in the previous timestep. If we assume that the entropy of these cells in the previous timestep is equal to that of the stellar surface, then we can calculate $\varepsilon_{\rm grav}$ using Eq. (2.43) or (2.44). However, here we use another

[17] The compressional heating is originally developed for the calculation of accreting white dwarfs, namely the classical novae, in which usually $t_{\dot{M}} \ll t_{\rm th}$.

[18] This was implemented after paper II. Therefore this has currently not been written in Paxton et al. papers. See the mailing list (http://sourceforge.net/p/mesa/mailman/).

[19] We use temperature and gas pressure as thermodynamic variables, instead of density. While these quantities are calculated by the newton solver, the entropy is calculated with these variables and EoS.

scheme: the "Eulerian" scheme following Sugimoto & Nomoto (1975) [20], in which the mass ratio (relative mass) $q = m/M_\star$ is used as a spatial coordinate. The time derivatives between the Lagrangian and Eulerian coordinate are transformed as

$$\begin{aligned}\left(\frac{\partial}{\partial t}\right)_m &= \left(\frac{\partial}{\partial t}\right)_q - \left(\frac{\partial q}{\partial t}\right)_m \left(\frac{\partial}{\partial q}\right)_t \\ &= \left(\frac{\partial}{\partial t}\right)_q - \frac{\partial \ln M_\star}{\partial t}\left(\frac{\partial}{\partial \ln q}\right)_t \\ &= \left(\frac{\partial}{\partial t}\right)_q - \left(\frac{\partial m}{\partial t}\right)_q \left(\frac{\partial}{\partial m}\right)_t , \end{aligned} \tag{2.45}$$

where the second term on the right-hand side is the "advection term", i.e., the change of the mass coordinate in the same cell while q is the same.

In using this equation to evaluate $\varepsilon_{\rm grav}$, the round-off error can appear on both terms. On the first term on the right-hand side (RHS), as in the Lagrangian scheme Eq. (2.44), the entropy difference is replaced by the differences of basic thermodynamic variables at the same q. On the second term, in the case that the entropy difference between the neighboring cells can be extremely small, the round-off error can matter. To avoid it, we rewrite $(\partial s/\partial m)_t$ as

$$\left(\frac{\partial s}{\partial m}\right)_t = \left(\frac{\partial s}{\partial P}\right)_t \left(\frac{\partial P}{\partial m}\right)_t = \frac{c_P}{P}\left(\nabla - \nabla_{\rm ad}\right)\left(-\frac{GM_\star}{4\pi r^4}\right) . \tag{2.46}$$

With the equations above, $\varepsilon_{\rm grav}$ can be evaluated as

$$\varepsilon_{\rm grav} = -Tc_P\left[\left(1 - 4\nabla_{\rm ad}\frac{P_{\rm rad}}{P}\right)\left(\frac{\partial \ln T}{\partial t}\right)_q - \nabla_{\rm ad}\frac{P_{\rm gas}}{P}\left(\frac{\partial \ln P_{\rm gas}}{\partial t}\right)_q\right] \tag{2.47}$$

$$-\frac{Tc_P}{P}q\dot{M}\left(\nabla - \nabla_{\rm ad}\right)\left(\frac{GM_\star}{4\pi r^4}\right) . \tag{2.48}$$

Note that the second term is not the time derivative and the precision is better than the first term, which is the time derivative.

Transition region

Finally, in the transition region, the two schemes are linearly combined in order to make a smooth transition.

The region in which the Eulerian scheme is used is defined as ten times as large as the mass just added in the timestep. The transition region is constructed by ten cells. Note that since in the Eulerian scheme, the material moves between cells and as a result the numerical diffusion

[20] Note that this "Eulerian" scheme is not the same as the exact meaning of it, namely it usually means the spatial coordinate is fixed in the spatial points in the sense of classical hydrodynamics.

is caused, it is better to take the large Lagrangian region.

2.7.6 Assumptions

Here the assumptions in this study are summarized:

- The effects of the stellar rotation and the magnetic fields are neglected
- No mass loss
- The initial mass of the protostar is 0.01 $M_{\odot}$
- The heat injected by the accreting materials is distributed uniformly in the entire star

Chapter 3

Results

In this chapter we explore the PMS evolution with accretion, particularly focusing on the radius, evolutionary track on the H-R diagram, and the internal structure. We demonstrate that the evolutions with the cold accretion are dramatically different from the classical ones in Sec. 3.1. We have found that the heat injection efficiency and the deuterium content are the important parameters in the PMS evolution as described in Secs. 3.2 and 3.3.

Note that our calculations with the stellar evolution code MESA is reliable. We show that the energy conservation is well satisfied in Appendix A.

3.1 Cold accretion

In this section, we show the results of the PMS evolution in the case of the cold accretion, in which the heat injection by the accreting material is negligible (i.e., $\xi = 0$ in Eq. 2.38). After explaining the basic behavior of the evolution in Sec. 3.1.1, we show the influence of the mass accretion rate, the initial condition and the deuterium content.

3.1.1 Overview of the typical case

In this section we show the results of the typical case, that is, the steady cold accretion with $\dot{M} = 10^{-5}\,M_\odot/\mathrm{yr}$. The settings are listed in Table 3.1. The radius evolution is shown in Fig. 3.2. The evolution can be split into five phases: (I) the contraction phase, (II) the deuterium-burning phase, (III) the second contraction phase (IV) the swelling phase and (V) the main sequence from $\sim 2 \times 10^7$ yr. We explain the evolution in the individual phases in detail.

Contraction phase. In this phase, the star shrinks as increasing mass. The radius evolution

Table 3.1: Settings of the results in Sec. 3.1.1.

Initial mass	0.01 $M_\odot$
Final mass	1 $M_\odot$
Initial radius	1.5 $R_\odot$
Mass accretion rate	1.0×10^{-5} $M_\odot$/yr
Duration of accreting phase	9.9×10^4 yr
Deuterium mass fraction, $X_{\rm D}$	2.0×10^{-5}
Heat injection, ξ	0 (cold accretion)

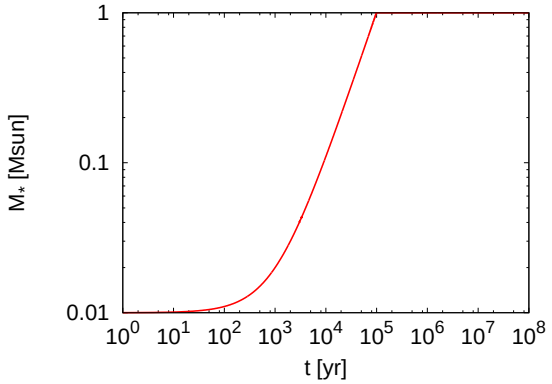

Figure 3.1: Evolution of the stellar mass as a function of time under the settings in Table 3.1.

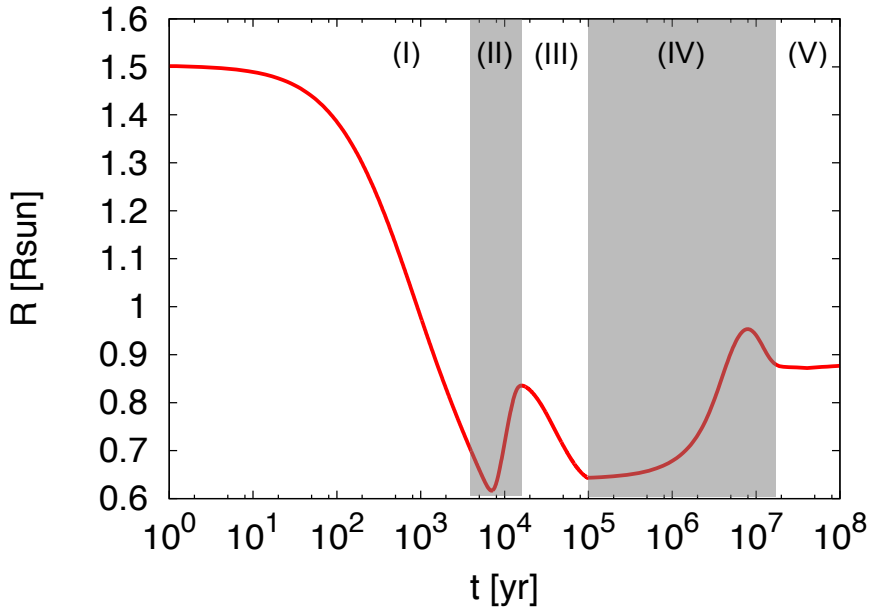

Figure 3.2: Radius evolution under the settings in Table 3.1. There are five phases: (I) the contraction phase, (II) the deuterium-burning phase, (III) the second contraction phase, (IV) the swelling phase and (V) the main sequence from $\sim 2 \times 10^7$ yr.

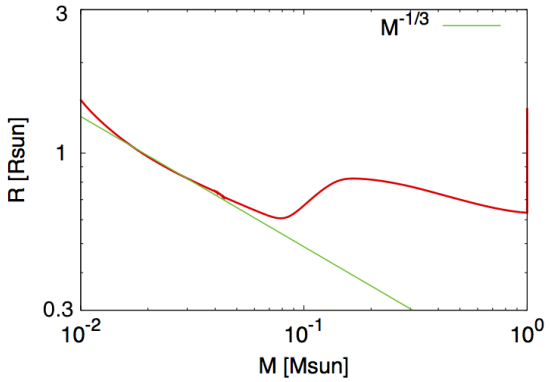

Figure 3.3: Mass-radius relation. In the contraction phase, the radius is proportional to the minus one third of the mass. This corresponds to the adiabatic contraction.

can be fitted by

$$R_\star \propto M_\star^{-1/3} \ . \tag{3.1}$$

as shown in Fig. 3.3. This relation represents the adiabatic contraction and is derived by two approaches using gravo-thermodynamic relation or polytropic analysis (e.g., Hosokawa et al. 2010, Hartmann et al. 1997).

First, the characteristic density and pressure of the star in the hydrostatic equilibrium are given by

$$\tilde{\rho} \propto M_\star / R_\star^3 \ , \qquad \tilde{P} \propto M_\star^2 / R_\star^4 \ . \tag{3.2}$$

The entropy is given by

$$s = c_V \ln \left(\frac{P}{\rho^{\gamma_{\rm ad}}} \right) + s_0, \tag{3.3}$$

where c_V is the specific heat at constant volume and $\gamma_{\rm ad} (= c_P/c_V)$ is the specific heat ratio. Substituting Eq. (3.2) into this equation,

$$R_\star = M_\star^{-(2-\gamma_{\rm ad})/(3\gamma_{\rm ad}-4)} \exp \left(\frac{1}{3\gamma_{\rm ad}-4} \frac{s-s_0}{c_V} \right), \tag{3.4}$$

In the case of the monatomic ideal gas, we obtain

$$s = \frac{2}{3} \frac{\mu}{\mathcal{R}} \ln \left(\frac{P}{\rho^{5/3}} \right) + s_0 \tag{3.5}$$

and

$$R_\star \propto M_\star^{-1/3} \exp\left[\frac{2}{3}\frac{\mu}{\mathcal{R}}(s-s_0)\right] \ . \tag{3.6}$$

In the case of the isentropic evolution, this gives Eq. (3.1).

Secondly, Eq. (3.1) is also derived from the energy conservation. The total energy is given by the sum of the internal and gravitational energy: $E_{\rm tot} = E_{\rm int} + E_{\rm g}$ (Eq. 2.11). From the Virial theorem,

$$E_{\rm tot} = (4-3\gamma_{\rm ad})E_{\rm int} = \frac{3\gamma_{\rm ad}-4}{3(\gamma_{\rm ad}-1)}E_{\rm g} \tag{3.7}$$

If we assume the polytropic relation, that is, $P(\rho) = K\rho^{1+1/n}$, then,

$$E_{\rm g} = -\frac{3}{5-n}\frac{GM_\star^2}{R_\star} \ . \tag{3.8}$$

Therefore,

$$E_{\rm tot} = -\frac{3\gamma_{\rm ad}-4}{(\gamma_{\rm ad}-1)(5-n)}\frac{GM_\star^2}{R_\star} \ . \tag{3.9}$$

In the fully convective star which consists of monatomic ideal gas, $n = 2/3$ and $\gamma_{\rm ad} = 5/3$ and then we obtain

$$E_{\rm tot} = -\frac{3}{7}\frac{GM^2}{R} \ . \tag{3.10}$$

Using Eq. (3.9), the total energy evolution in Eq. (2.16) is transformed as follows:

$$\begin{aligned}
&\frac{\rm d}{{\rm d}t}\left(-C\frac{GM^2}{R}\right) = -L_\star + L_{\rm nuc} - \frac{GM_\star\dot{M}}{R_\star} + L_{\rm add} \ , \\
&-C\frac{GM^2}{R}\left(2\frac{\dot{M}}{M_\star} - \frac{\dot{R}}{R_\star}\right) = -L_\star + L_{\rm nuc} - \frac{GM_\star\dot{M}}{R_\star}\left(1-\xi\right) \ , \\
&-C\frac{GM^2}{R}\left[\frac{\dot{M}}{M_\star}\left(2-\frac{1-\xi}{C}\right) - \frac{\dot{R}}{R_\star}\right] = -L_\star + L_{\rm nuc} \ .
\end{aligned} \tag{3.11}$$

where $C \equiv (3\gamma_{\rm ad}-4)/(\gamma_{\rm ad}-1)(5-n)$. In the quasi-static star, $\gamma_{\rm ad} > 4/3$ and then $C > 0$. Therefore,

$$\frac{\dot{R}}{R_\star} = \left(2-\frac{1-\xi}{C}\right)\frac{\dot{M}}{M_\star} - \frac{RL_\star}{CGM^2} + \frac{RL_{\rm nuc}}{CGM^2} \ . \tag{3.12}$$

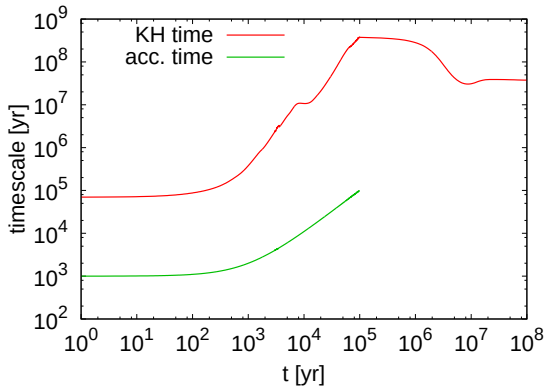

Figure 3.4: Comparison between the accretion timescale (green line) and the K-H timescale (red line). The K-H timescale is always much longer than the accretion timescale.

The second term of RHS corresponds to the inverse of the Kelvin-Helmholtz (K-H) timescale $\tau_{\rm KH}$, which is defined as the typical timescale to lose the total energy by radiation (i.e., $\tau_{\rm KH} \equiv |E_{\rm tot}|/L_\star$).

During the protostar phase in the case of the cold accretion, $\tau_{\rm KH}$ is much longer than the accretion timescale $\tau_{\dot{M}} = M/\dot{M}$, as shown in Fig. 3.4. This means that the accretion is adiabatic. Therefore, the second term of RHS of Eq. (3.12) can be neglected when the first term of RHS is not zero, namely $1 - \xi \neq 2C$. In the case that $L_{\rm nuc} = 0$, $\xi = 0$ (cold accretion) and $C = 3/7$ (fully convective star constructed by monoatomic gas), we obtain Eq. (3.1).

As the contraction proceeds, the central temperature becomes higher. From the Virial theorem, the internal energy, which is roughly $\sim k\tilde{T}M_\star$, is minus one-half of the gravitational energy, $\sim -GM_\star^2/R_\star$, where $\tilde{T}$ is the characteristic temperature. Thus, if $T_c \propto \tilde{T}$, then the central temperature is proportional to the stellar mass over radius,

$$T_{\rm c} \propto M_\star/R_\star \ . \tag{3.13}$$

Combining Eq. (3.1), the mass accretion results in increasing the central temperature as $T_{\rm c} \propto M_\star^{4/3}$.

Deuterium-burning phase. After the central temperature exceeds $\sim 10^6$ K, deuterium fusion affects the evolution (see Sec. 2.2.3). In the current settings, it happens at $t = 7 \times 10^3$ yr and $M_\star \simeq 0.08\ M_\odot$. As described in Sec. 2.2.3, the energy production rate of deuterium burning has a strong temperature dependence, that is, $\varepsilon_{\rm nuc} \propto (T/10^6\ {\rm K})^{11.8}$. This strong temperature sensitivity of deuterium burning is important in the two aspects: the "thermostat" effect and convection (e.g., Stahler 1988).

The thermostat effect causes the expansion. After the ignition of deuterium, the central temperature stays at about 10^6 K. This is because of the strong sensitivity of deuterium fusion to the temperature. If the temperature increases over 10^6 K, $\varepsilon_{\rm nuc}$ substantially increases. The energy production results in the expansion of the deuterium-burning region and then the temperature decreases. On the contrary, if the temperature and $\varepsilon_{\rm nuc}$ decrease, the central region shrinks and then the temperature decreases. Therefore deuterium burning adjusts the central temperature and this effect is called the "thermostat" effect. From Eq. (3.13), the constant central temperature in accreting stars results in the expansion.

Additionally, the energy produced by deuterium burning is sufficient to the expansion. From the energy balance (Eq. 3.12), the critical energy production rate by the nuclear reaction for the expansion can be derived. If the bolometric luminosity is negligible and the star is fully convective,

$$\frac{\dot{R}}{R_\star} = -\frac{1}{3}\frac{\dot{M}}{M_\star} + \frac{7}{3}\frac{RL_{\rm nuc}}{GM^2} \ . \tag{3.14}$$

Note that in the current settings, the K-H timescale is always much longer than the accretion timescale (see Fig. 3.4). Therefore, the condition for the expansion is given by

$$L_{\rm nuc} > \frac{1}{7}L_{\rm acc} \ , \tag{3.15}$$

where $L_{\rm acc} = GM_\star\dot{M}/R_\star$. In the current result, the ratio $L_{\rm nuc}/L_{\rm acc}$ is large (up to about 0.4 at $\sim 10^4$ yr) due to the rapid vigorous burning of the pre-existent deuterium. Thus, $\dot{R} > 0$ in this phase.

Moreover, the strong temperature dependence in deuterium burning is also important for the interior structure. It makes the deuterium burning region confined to only the tiny region. Since the energy produced by deuterium fusion results in the sharp increase of the entropy in the deuterium burning region, the convective instability (Eq. 2.23) is caused (Kippenhahn & Weigert 1990). Thus, in the star with the sufficient deuterium at the center, deuterium fusion results in the fully-convective structure. However, if deuterium accretes to the star with the deuterium-free radiative core, the newly accreted deuterium is burned at the base of the convective zone and then the fully convection does not occur.

Second contraction phase. Pre-existent deuterium is exhausted by $\sim 1.5\times10^4$ yr as shown in Fig. 3.6. After the deuterium is exhausted, the star shrinks again. This is because the mass of the freshly accreted deuterium, $\dot{M}_{\rm D} = \dot{M}X_{\rm D}$, is not sufficient to compensate for the compression

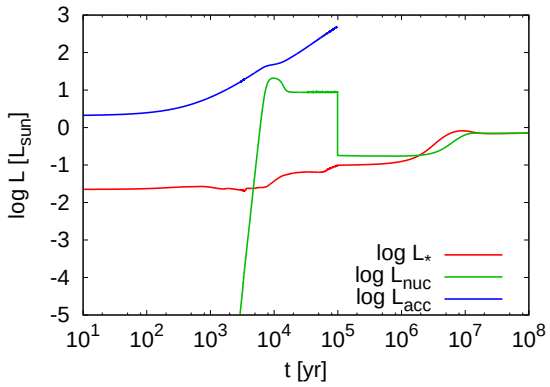

Figure 3.5: Evolution of the bolometric luminosity ($L_\star$, red line), the energy production rate by thermonuclear reaction ($L_{\rm nuc}$, green) and the accreting material's gravitational energy ($L_{\rm acc}$, blue). Although $L_{\rm acc}$ is always the largest, $L_{\rm nuc}$ is close to it around 10^4 yr. This causes the expansion of the star. The flat $L_{\rm nuc}$ from $\sim 2\times10^4$ to 10^5 yr results from the instantaneous fusion of the newly accreted deuterium.

by accretion. If this is instantaneously completely burned, then, using Eq. (2.29), the energy production rate by deuterium burning, $L_{\rm D}$, is constant as

$$L_{\rm D} = 8.65\ L_\odot \left(\frac{\dot{M}}{10^{-5}\ M_\odot/{\rm yr}}\right)\left(\frac{X_{\rm D}}{2.0\times10^{-5}}\right)\ . \tag{3.16}$$

This estimation reproduces the result well in Fig. 3.5. Note that $L_{\rm nuc}$ is dominated by the deuterium burning and then $L_{\rm nuc} \simeq L_{\rm D}$ until the accretion ceases at 10^5 yr. Although $L_{\rm nuc}$ is much larger than $L_\star$, $L_{\rm acc}$ is even larger:

$$L_{\rm acc} = 31.3\ L_\odot \left(\frac{M_\star}{0.1\ M_\odot}\right)\left(\frac{R_\star}{R_\odot}\right)^{-1}\left(\frac{\dot{M}}{10^{-5}\ M_\odot}\right)\ . \tag{3.17}$$

Since in this phase the ratio $L_{\rm nuc}/L_{\rm acc}$ ($\sim 0.3(M_\star/0.1M_\odot)^{-1}$) ranges about 0.03 to 1/7, the effect of the thermonuclear energy production is suppressed by the adiabatic contraction and then the star shrinks. This phase lasts until the accretion ceases.

Swelling phase. After the accretion ceases, the radius remains nearly constant for several million years. This timescale is determined by the thermal timescale in the deep interior. Although in this phase the K-H timescale at the surface is $\sim 10^7$–10^8 years, the thermal timescale in the interior is shorter. This is because the luminosity in the deep interior is much larger than that at the surface due to the absorption of energy in the stellar interior. Figure 3.7b shows the luminosity at the interior can be larger than that at the surface by a factor of several to ten. Thus, the thermal timescale in the interior, $\sim Gm^2/(2rl)$, is down to about several million years in the deep interior as shown in Fig. 3.7a. Note that the dominant source of the luminosity

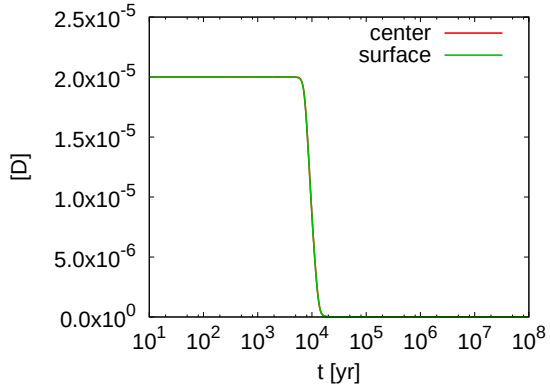

Figure 3.6: Evolution of the mass fraction of deuterium, $X_{\rm D}$, at the center (red line) and at the surface (green line). The same behavior of the two lines comes from the fully convective structure.

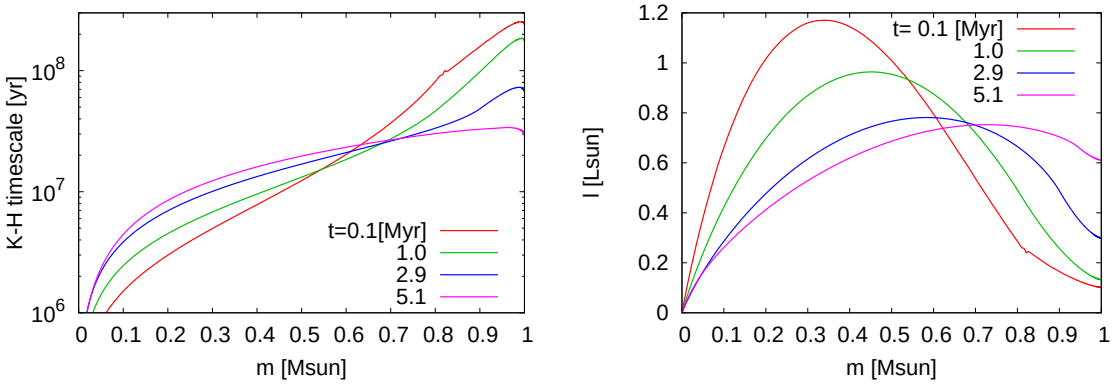

Figure 3.7: (a) *Left panel.* K-H timescale, $Gm^2/2rl$, as a function of the mass coordinate. (b) *Right panel.* Luminosity distribution as a function of the mass coordinate. The luminosity appears to propagate with time (so-called "luminosity wave").

is the energy release in each mass shell, namely $\varepsilon_{\rm grav}$ of the interior material rather than the hydrogen burning, which is confined to the central region with the mass $\lesssim 0.1\ M_\odot$. In this phase the central temperature already exceeds 10^7K due to the small radius. Thus, hydrogen burning takes place although it is not vigorous ($L_{\rm nuc} \sim 0.1 L_\odot$) at this phase.

After several million years, the star expands. This is because the internal structure is adjusted after the K-H timescale and then the temperature becomes high enough, namely the opacity becomes low enough to transport the luminosity toward the surface. As shown in Fig. 3.7b, the luminosity propagates from the interior to the surface rapidly (so-called "luminosity wave", Stahler et al. 1986). Therefore the surface gains the entropy and the star expands.

Main sequence. After the swelling phase, the star shrinks and enters its main sequence (MS). The bolometric luminosity is the same as the nuclear energy production rate and the rapid structure evolution does not occur any more until leaving its MS due to the exhaustion

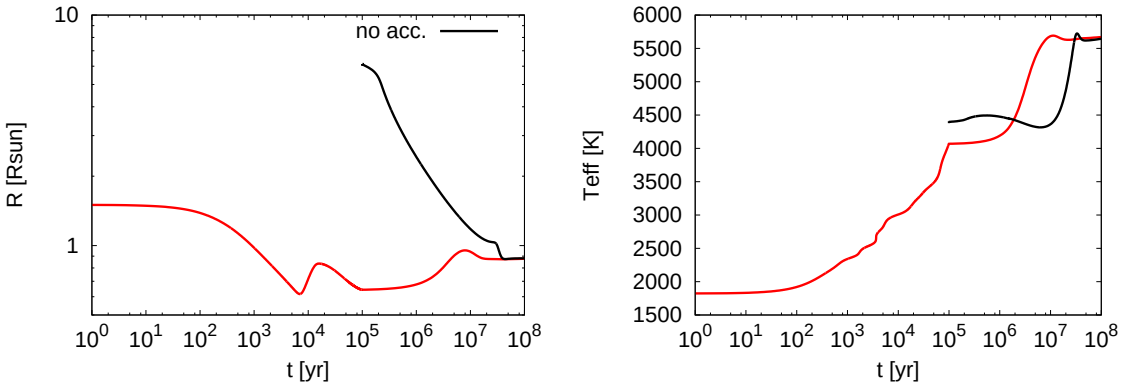

Figure 3.8: *Left panel.* Comparison of the radii of the cold accretion (red line) and the classical 1 $R_\odot$ evolution (black). In the non-accreting classical model the initial radius is assumed to be 6.1 $R_\odot$ and the duration of the accretion phase is 10^5 yr. *Right panel.* Comparison of the effective temperature evolution.

of hydrogen at the central region. For a 1 $M_\odot$ star, its MS lasts about 10 Gyr.

3.1.2 Comparison with the classical model

We compare the radius evolution in the case of the cold steady accretion with that in the classical model. Since in the classical hydrodynamic simulation, contraction of a gas sphere of a mass equal to the final mass is assumed without any mass addition through disk accretion, a large amount of heat is injected by the accreting material. Thus, the radius of a 1 $M_\odot$ star when the accretion is completed is for example ~ 4.7 $R_\odot$ in Stahler et al. (1980a) and 6.2 $R_\odot$ in Behrend & Maeder (2001). Here we adopt their results: the initial radius of the classical model is ~ 6.1 $R_\odot$ at 10^5 yr.

Figure 3.8 shows that the radius in case of the cold accretion is smaller than that in the classical evolution by an order of magnitude, which results in the different internal structure evolution and the evolutionary track, as we will discuss in the following (Secs. 3.1.3 and 3.1.4). Moreover, due to the small radius and then the high temperature, the K-H timescale in the interior is shorter in the case of the cold accretion. Thus, the star with the cold accretion enters its main sequence earlier.

3.1.3 Internal structure

As we will show, the small radius in the cold accretion leads to an important result that surface convective zone shrinks on a timescale of a few million years. The smaller radius makes the central temperature higher and consequently develops a radiative core. Figure 3.9 shows the

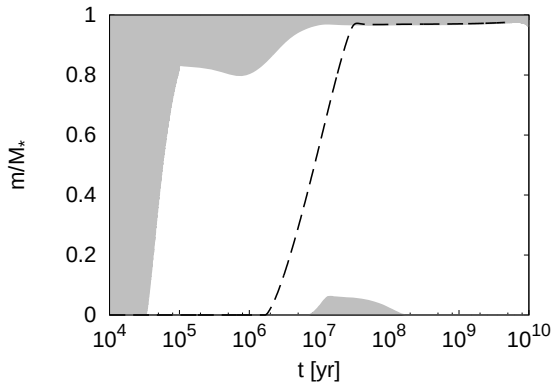

Figure 3.9: Internal structure evolution. The shaded region indicates the convective region. The high central temperature due to the small radius develops the radiative core even in $\sim 10^5$ yr. Note that the accretion is completed at 10^5 yr. The convective core temporarily appears due to the CNO cycle from 10^7 to 10^8 years. The dashed line indicates the base of the surface convective region in the case of the classical non-accreting 1 $M_\odot$ star.

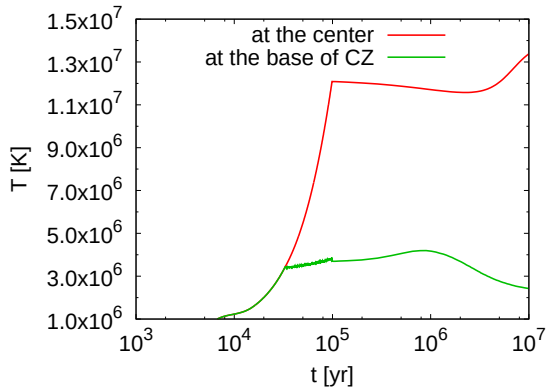

Figure 3.10: Temperature at the center (red line) and at the base of the surface convective zone, namely the top of the radiative core (green). The central temperature exceeds 10^7 K after the accretion. The radiative zone extends to the temperature about 2–4 $\times$ 10^6 K due to the opacity bump (see Sec. 2.2.2).

internal structure evolution. The star develops the large radiative core even in several 10^4 years. This is because the central temperature exceeds several million kelvin even in tens of thousand years as shown in Fig. 3.10. As described in Sec. 2.2.2, at the temperature greater than a few million kelvin, the opacity decreases and then the radiative core tends to develop. Therefore, the radiative core starts to develop at several 10^4 years.

After the accretion is completed at 10^5 yr, the surface convective region becomes slightly large. This is because the entropy propagating from the deep interior in the radiative zone accumulates at the base of the convective zone. Since the convective instability occurs when $\partial s/\partial m \leq 0$, the extension of the constant entropy region as shown in Fig 3.11 leads to the extension of the convective zone.

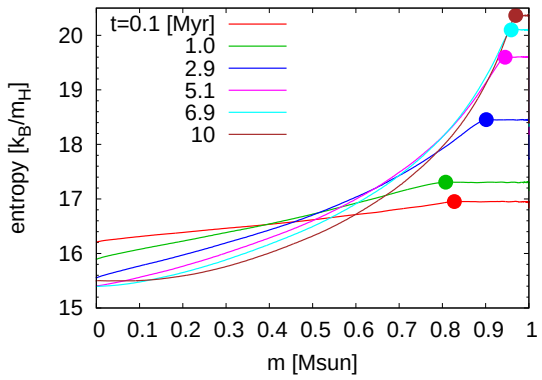

Figure 3.11: Entropy profile at 0.1 million years (hereafter Myr, red line), 1 Myr (green), 3 Myr (blue), 5 Myr (magenta), 7 Myr (cyan) and 10 Myr (brown). The points indicate the base of the surface convective zone. The convective zone spreads from 0.1 to 1 Myr, while after 1 Myr it shrinks.

As the temperature there increases, the opacity decreases and then the accumulated entropy is able to flow toward the surface. Thus, after $\sim 10^6$ yr, the convective region shrinks again.

The mass of the surface convective zone, $M_{\rm CZ}$, becomes 0.1 $M_\odot$ at 2.74 Myr and 0.03 $M_\odot$ at 10.6 Myr. Here we define the time when $M_{\rm CZ} = 0.1\ M_\star$ as $t_{\rm CZ}$. The fact that $t_{\rm CZ}$ is as short as 2.74 Myr is very important because it is shorter than the typical disk lifetime, 3–6 Myr (e.g., Haisch et al. 2001). The impact of this result on a link between planet formation and stellar surface compositions is discussed in Sec. 4.3.2.

On the other hand, in the classical model based on the spherical accretion, the surface convective zone of a 1 $M_\odot$ star shrinks much later, namely $M_{\rm CZ}$, becomes 0.1 $M_\odot$ at 23.8 Myr and 0.03 $M_\odot$ at 32.2 Myr. Surprisingly, the difference in $t_{\rm CZ}$ is about one oder of magnitude. At 24 Myr, the disk has most likely already dissipated.

3.1.4 Evolutionary track

The pre-main-sequence evolutionary tracks in the case of steady cold accretion and classical non-accreting model are shown in Fig. 3.12. Again, they are also drastically different. In the former case, it is roughly horizontal because the accretion does not inject energy and then the stellar luminosity remains small. On the other hand, in the classical case, when the accretion is completed, the star has a lot of entropy and then appears at the top of its *Hayashi track*. The star evolves through the vertical Hayashi track followed by the horizontal *Henyey track* on the Herzsprung-Russell (H-R) diagram. The impact of this result is described in Sec. 4.2.

Note that the evolutionary track in the case of steady cold accretion in Fig. 3.12 does not include the accretion luminosity. We assume it is radiated away from the disk surface or at

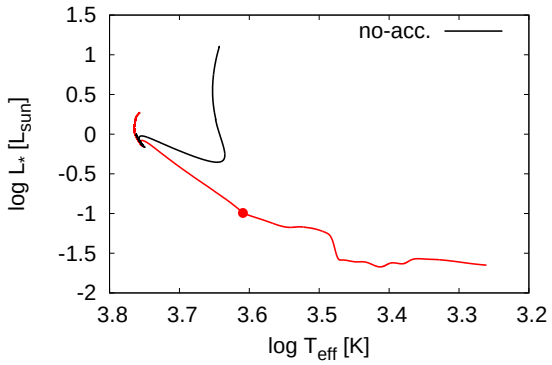

Figure 3.12: evolutionary tracks of the cold steady accretion model (red line, until 10^{10} yr) and the non-accreting 1 $M_\odot$ star (black, until the solar age) on the H-R diagram. The point indicates the location where the accretion is completed. While in the classical model the evolution has the Hayashi and Henyey tracks, in the cold accretion model the evolution proceeds roughly from bottom right (namely less luminous and cold) to the top left region on the H-R diagram. Although deuterium burning enlarges it where $\log(T_{\rm eff}) \simeq 3.5$, it is smaller than the Henyey track of the non-accreting 1 $M_\odot$ star.

the stellar surface. If the disk and stellar surface to the space is optically thin for the short-wavelength photons, the accretion luminosity can be excluded from the bolometric luminosity because it is originally emitted by UV or X-rays and then we can exclude its component in the spectral energy distribution. However, if it is absorbed by the natal cloud and re-emitted in the longer wavelength, it is difficult to distinguish the accretion luminosity from the intrinsic one because the stellar intrinsic luminosity is also emitted in the primarily infrared wavelength. In the latter situation, the location of a star is shifted upward (Hosokawa et al. 2011).

3.2 Cold accretion with various settings

In the following three sections, we explore the impact of changing three settings: the accretion history, the initial condition, and the deuterium content. The impact of the heat injection and the final mass is discussed in Secs. 3.3 and 4.2.1, respectively. The factor which affects the evolution is the stellar entropy as shown in Eq. (3.6). We show that the initial condition, the deuterium content and the heat injection affect the evolution. This is because the different initial condition results in the different accreting material's entropy in the case of the cold accretion, because the deuterium content affects the entropy produced by the thermonuclear reaction, and because the injected heat is equivalent to the entropy injection.

3.2.1 Dependence on the mass accretion rate

In this section we investigate the effect of varying the accretion history. As described in Sec. 2.5, the mass accretion rate can be different in each star and time-dependent in a star, depending on the condition of the parent cloud or the disk. It ranges typically $\sim 10^{-6}$–10^{-4} $M_\odot$/yr. Here we explore the influence of the mass accretion rate on the evolution.

Figure 3.13 shows the radius evolution as a function of time and mass with varying the mass accretion rate in the case of cold steady accretion. Note that the varying mass accretion rate results in the different duration of the accretion phase since the initial and final mass are fixed to be 0.01 and 1 $M_\odot$, respectively. We find three features: First, the difference in the radii at the same mass is at most 0.2 $R_\odot$. Secondly, the radius in the case of 10^{-6} $M_\odot$/yr is smaller than that at the same mass before deuterium burning. Finally, the radius in the case of 10^{-4} $M_\odot$/yr is the smallest at the same mass after deuterium ignites.

First and most importantly, the difference in the radii at the same age after the accretion is at most $\sim$ 10%. As we describe later, this difference is much smaller than the difference from other effects such as the initial condition, the chemical composition and the heat injection efficiency. This is because in the cold accretion the accreting material's entropy is the same as the stellar surface and then the total injected energy throughout the accretion does not change largely.

Secondly, as shown in Fig. 3.4, at first the K-H timescale is about 10^5 yr. Thus, in the case that $\dot{M} = 10^{-6}$ $M_\odot$/yr, the accretion timescale is comparable and then the effect of the radiative cooling is not negligible. Therefore, the radius is smaller than the other adiabatic cases.

Finally, the larger the mass accretion rate is, the smaller the radius is after deuterium burning. This is caused by the short duration of the expansion phase by deuterium burning. It lasts from 0.093 to 0.174 $M_\odot$ in the case that $\dot{M} = 10^{-4}$ $M_\odot$/yr while from 0.065 to 0.176 $M_\odot$ in the case that $\dot{M} = 10^{-6}$ $M_\odot$/yr. In case of the larger mass accretion rate, $L_{\rm acc} = GM_\star\dot{M}/R_\star$ is larger. Since the expansion occurs only when $L_{\rm nuc} > (1/7)L_{\rm acc}$ (3.15), the larger $L_{\rm acc}$ tends to suppress the expansion effect of deuterium burning and then the radius when the deuterium burning phase finishes is smaller.

Episodic accretion

Here we explore the effect of the time variability of the accretion following the pioneering works such as Baraffe et al. (2009) and Hosokawa et al. (2011). This is because the recent

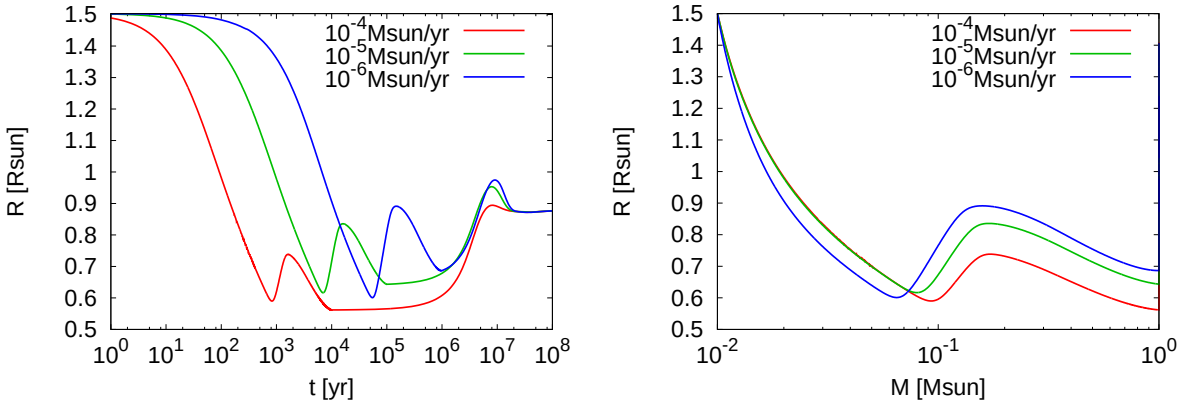

Figure 3.13: (a) *Left panel.* Radius evolution with time with cold steady accretion varying the mean mass accretion rate. The red, green and blue lines indicate the cases that $\dot{M} = 10^{-4}, 10^{-5}$ and 10^{-6} $M_\odot$/yr, respectively. Thus, the accreting phase lasts $\simeq 10^4, 10^5$ and 10^6 yr, respectively. The difference is only slight even if the mass accretion rate changes two orders of magnitude. The larger mass accretion rate leads to the slightly smaller radius. (b) *Right panel.* Radius evolution with mass. Before deuterium ignites, the radii of $\dot{M} = 10^{-4}$ and 10^{-5} $M_\odot$/yr are exactly the same at the same mass, while in the case of 10^{-6} $M_\odot$/yr the star is smaller. This is because the radiative cooling have effect only in the latter case.

Table 3.2: The accretion history in the case of the episodic accretion.

Mass accretion rate in the accretion phases	5.0×10^{-4} $M_\odot$/yr
Mass accretion rate in the quiescent phases	0
Duration of each accretion phase	10^2 yr
Duration of each quiescent phase	10^3 yr
Number of accretion phases	20

hydrodynamic simulations show that the accretion around the young stars can be episodic as described in Sec. 2.5. Moreover, Baraffe et al. (2009) claimed that the importance of the episodic accretion for the small radius, whereas Hosokawa et al. (2011) claimed that the low entropy in the cold accretion is essential. Our results support the Hosokawa et al. (2011)'s conclusion, i.e., the accretion history is not important.

Figure 3.14c shows the radius evolution under the accretion history summarized in Table 3.2 and illustrated in Fig. 3.14a, following Baraffe & Chabrier (2010). They adopted this accretion history referring to the results of the hydrodynamic simulation in Vorobyov & Basu (2010) [1]. The other settings are the same as in the preceding sections.

The radius evolution is highly affected by the energy production rate of deuterium burning, $L_{\rm D}$. Basically, during the accreting phase the star expands if $L_{\rm nuc} \gtrsim (1/7)L_{\rm acc}$, while during

[1]The magnetic field was not included in their simulation. The time variability of the accretion rate comes from the accretion of clumps formed by the gravitational instability.

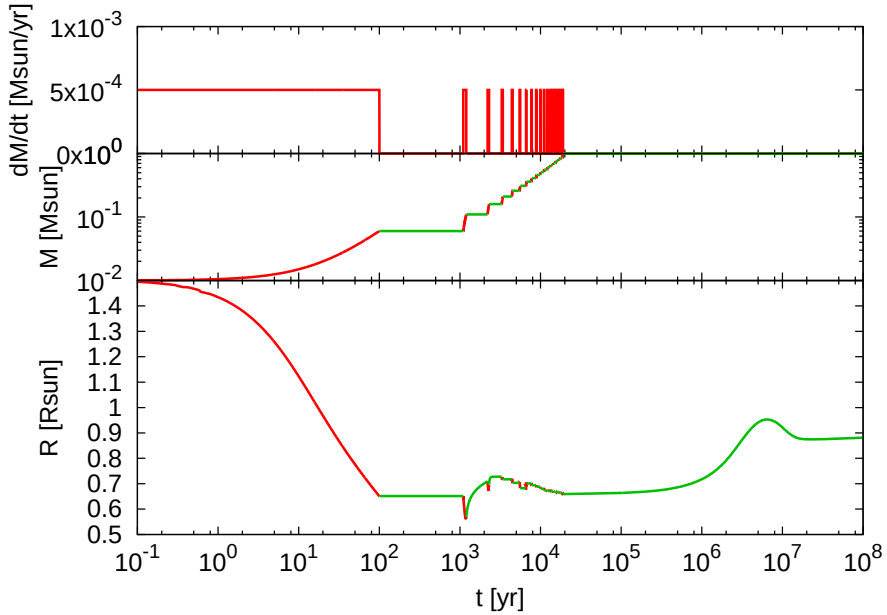

Figure 3.14: The lower panel (c) shows the radius evolution with the episodic mass accretion. The upper (a) and middle (b) panels show the evolution of the mass accretion rate and the stellar mass. The red and green lines indicate the accretion and quiescent phases, respectively.

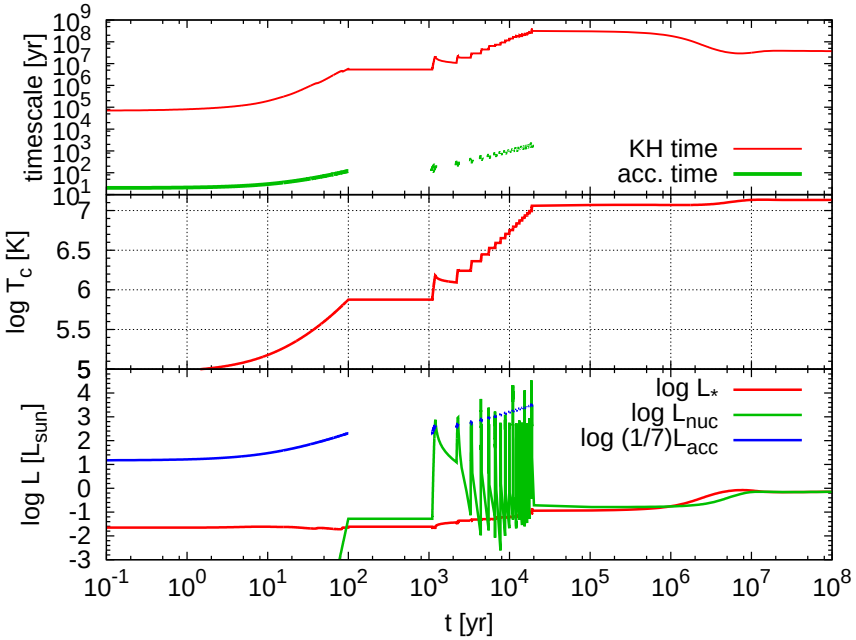

Figure 3.15: The upper (a), middle (b) and lower (c) panels show the K-H and accretion timescale, the central temperature, and the luminosity as a function of time in the case of the episodic accretion.

the quiescent phase $L_{\rm nuc} > L_\star$ as described in Sec. 3.1.1. The timescale for the radius evolution is determined by the total energy divided by $L_{\rm acc}, L_\star$ or $L_{\rm nuc}$. The K-H timescale and accretion timescale is shown in Fig. 3.15a.

For example, in the first quiescent phase from 100 to 1100 years, already $L_{\rm nuc} \simeq L_\star$ since the central temperature is close to 10^6 K as shown in Fig. 3.15b, and then deuterium burning partly occurs. The stellar mass at this phase is 0.06 $M_\odot$. However, the radius does not change because the timescale for the radius evolution, $R_\star/\dot{R}$, is much longer than the duration of the quiescent phase, 10^3 yr. On the contrary, in the second quiescent phase the star expands because $L_{\rm nuc}$ is about four orders of magnitude larger than $L_\star$ and $R_\star/\dot{R}$ is shorter than 10^3 yr.

In the accretion phase, sometimes $L_{\rm nuc}$ becomes larger than $(1/7)L_{\rm acc}$ as shown in Fig. 3.15c. Although the star expands temporarily, the expansion quickly suppresses deuterium burning and then the star shrinks.

Note that the radius evolution with the episodic accretion is almost the same as that with the steady accretion. The radius is about 0.7 $R_\odot$ after the accretion.

Compiling the results of the varying the mean mass accretion rate and its time dependence, from Figs. 3.13 and 3.14, we conclude that the varying mass accretion rate does not have a large impact on the evolution.

On the interpretation of the small radius in the case of the cold accretion, there was a discrepancy between Hosokawa et al. (2011) and Baraffe et al. (2009). Hosokawa et al. (2011) claimed that the accretion history does not affect the evolution largely, while Baraffe et al. (2009) claimed the importance of the episodic accretion. Our results support the Hosokawa et al.'s conclusion. The reason why the episodic accretion was thought to be important in Baraffe et al. (2009), is because they change many settings simultaneously, as claimed in Hosokawa et al. (2011). Rather, the smaller entropy of the accreting material in the cold accretion matters. In the cold accretion it is assumed to be the same as the stellar surface, while it is determined by the fraction of the injection of the accreting material's gravitational energy in the classical spherical accretion. Therefore, the smaller entropy results in the smaller radius and the accretion history does not matter.

The evolutionary tracks are also not affected by the variation of the accretion history as shown in Fig. 3.16.

3.2.2 Dependence on the initial condition

In this section we change the initial condition. As we described in Sec. 2.4, the seed protostar's radius and mass have not accurately determined by the hydrodynamic simulations yet. Therefore here we explore for a wide range of the initial radius and mass.

Here the initial mass is fixed to be 0.01 $M_\odot$, while the initial radius is changed from 0.25 $R_\odot$ to 3 $R_\odot$. The initial mass of the second core can be down to 10^{-3} $M_\odot$ (e.g., Inutsuka et al.

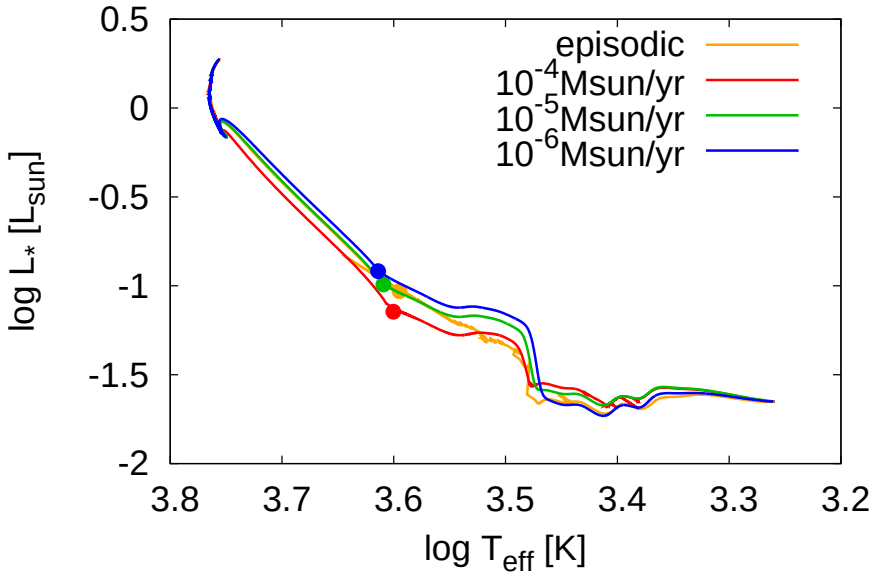

Figure 3.16: evolutionary tracks with varying the accretion history on the H-R diagram. The points show the locations where the accretion is completed.

2010). Variation in the initial mass can be translated via the adiabatic relationship $R_\star \propto M_\star^{-1/3}$, which holds in the first contraction phase, to the initial radius (see Sec. 3.1.1). Therefore, the calculation with the different initial mass approximately corresponds to the different initial radius in the fixed initial mass. For example, the difference in mass by a factor of ten is the same as that in radius by a factor of 2.16.

As shown in Eq. (3.6), the different initial radius in the fully convective star at the same mass corresponds to the different entropy, namely the larger entropy for the larger radius. We assume that in the cold accretion, the entropy of the accreting material, $s_{\rm acc}$, is the same as that of the stellar surface, $s_\star$. Therefore, if the protostar is initially large, $s_\star$ and then $s_{\rm acc}$ are large. The large $s_{\rm acc}$ results in the large radius in the entire evolution.

The smaller initial radius affects the age when deuterium burning starts. Since the smaller radius at the same mass results in the higher central temperature (approximately $T_{\rm c} \propto M_\star/R_\star$, Eq. 3.13), the star with the smaller initial radius starts deuterium burning earlier as shown in Fig. 3.18. Therefore, the adiabatic contraction before deuterium burning is short and then has only a little effect on the star with smaller radius. It starts at $\sim 0.03\ M_\odot$ in the case of the initially $0.25\ R_\odot$ star.

The initially $3\ R_\odot$ star shrinks more rapidly than $R_\star \propto M_\star^{-1/3}$. This is because the large luminosity results in the short K-H timescale ($\sim 10^4$ yr) and then the star shrinks due to the

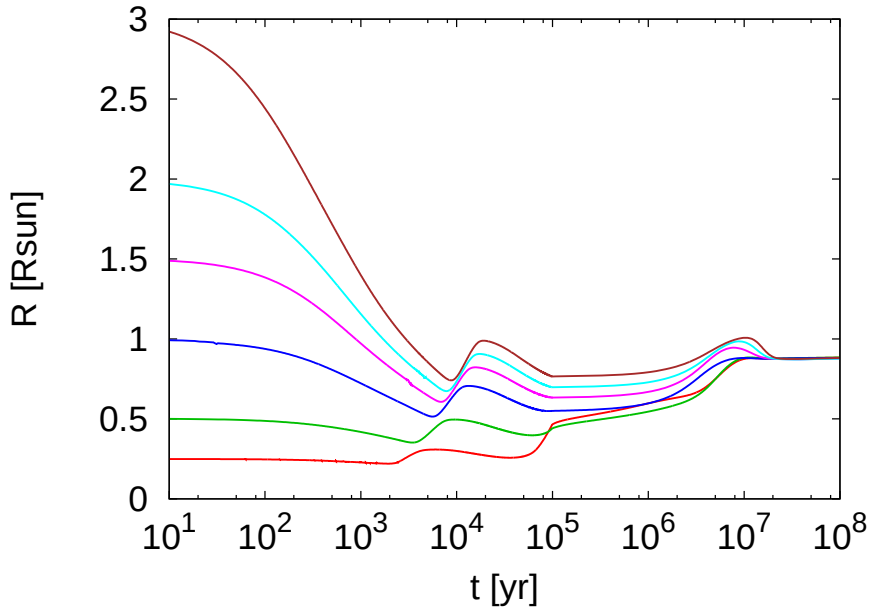

Figure 3.17: Radius evolution with varying the initial radius, $R_{\rm ini}$. From the bottom, the initial radius is 0.25 $R_\odot$ (red), 0.5 $R_\odot$ (green), 1 $R_\odot$ (blue), 1.5 $R_\odot$ (magenta), 2 $R_\odot$ (cyan) and 3 $R_\odot$ (brown). The initial condition is not lost until ZAMS, namely for example the initially 3 $R_\odot$ star is always the largest during the PMS phase. The evolution with $R_{\rm ini} = 0.25\ R_\odot$ becomes larger from $\sim 10^5$ yr than the star with $R_{\rm ini} = 0.5\ R_\odot$ because the extremely small radius makes hydrogen burning occur.

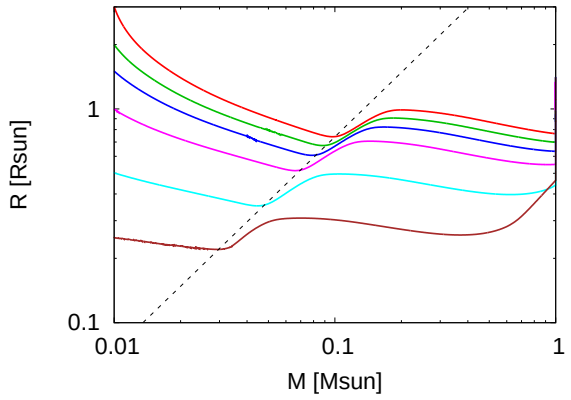

Figure 3.18: Mass-radius relation with varying the initial radius. The legend for the solid lines is the same as Fig. 3.17. The dashed line indicates the location where $R_\star \propto M_\star$, namely the central temperature is almost the same.

contraction by both the accretion and the radiative cooling.

The evolutionary tracks are also highly affected by the initial condition. The large initial radius corresponds to the large stellar entropy, which results in the large accreting material's entropy. The large radius and entropy enhance the luminosity. Figure 3.19 shows that the luminosity can be different by at most two orders of magnitude. We stress that the difference is

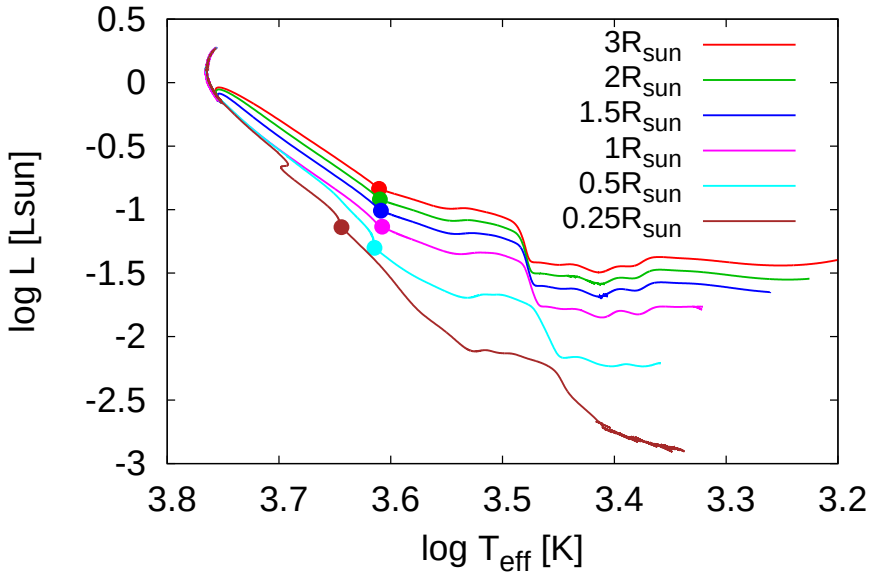

Figure 3.19: evolutionary tracks with varying the initial radius. The legends for the solid lines are the same as Fig. 3.17. The points show the location where the accretion is completed. The difference of the luminosity in the low-temperature region ($\log T_{\rm eff} \lesssim 3.5$) can be large by about two orders of magnitude.

much larger than that by the accretion history and tends to be larger in the lower temperature region.

Since the initial radius of the second core is important, it has not been precisely determined in the radiation-hydrodynamic simulations (see Sec. 2.4). In order to understand the PMS evolution, such a simulation is expected.

3.2.3 Dependence on the deuterium content

As described in Sec. 2.3.1, there can be a large variety in deuterium content in each star. However, the dependence of the PMS evolution on the deuterium content has not been investigated in the case of the cold accretion. In this section we explore the effect of the variation in the deuterium fraction. The other settings are the same as Sec. 3.1.1.

Figure 3.20 shows the radius evolution with the deuterium mass fraction from zero to 40 ppm[2]. While the evolutions before deuterium burning are totally independent of the deuterium content, those after deuterium burning are significantly different. This means the importance of deuterium burning in the PMS evolution.

The extent of the expansion due to deuterium burning is determined by the duration of

[2]The deuterium content of $X_{\rm D} = 40$ ppm, that is, (D/H) ~ 29 ppm, roughly corresponds to the cosmic primordial value.

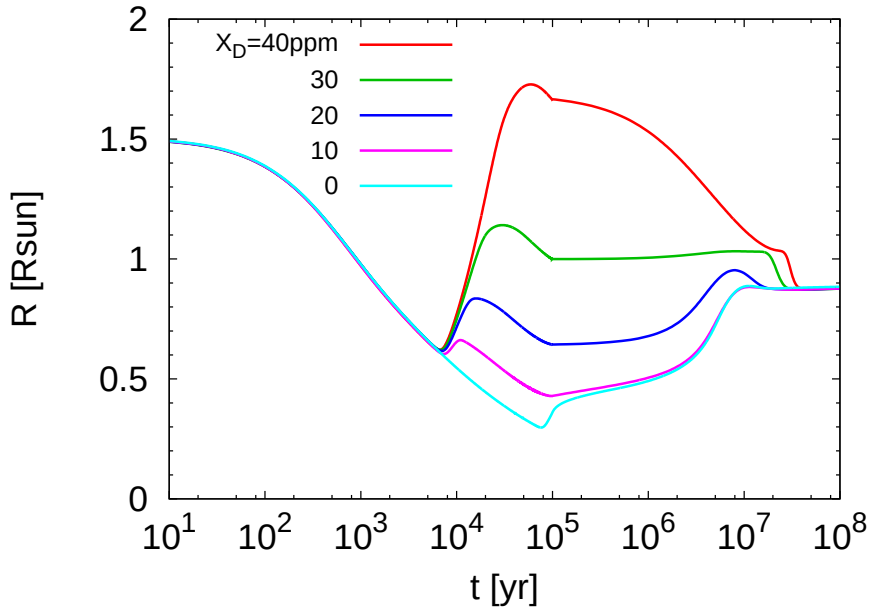

Figure 3.20: Radius evolution with varying the deuterium content ranging $X_{\rm D}$=40 (red line), 30 (green), 20 (blue), 10 (magenta) and 0 (cyan) ppm. The large deuterium content makes the duration of deuterium fusion long and then the radius large.

deuterium burning phase, $t_{\rm D}$ as described in Sec. 3.1.1. During deuterium burning, the thermostat effect makes the accreting star expand. We found that $t_{\rm D}$ is approximately proportional to $X_{\rm D}$ as shown in Fig. 3.21. $t_{\rm D}$ is determined by the deuterium content over the destruction rate of deuterium in Eq. (2.30), namely $t_{\rm D} \propto X_{\rm D}/(X_{\rm D}\rho T_6^{11.8})$. If the central temperature and density are independent of the deuterium fraction, $t_{\rm D}$ should be independent of the deuterium content. However, the higher deuterium fraction results in the higher energy production rate, and then the center density and temperature slightly decrease due to the expansion. As a result, the energy production rate is adjusted to be independent of the deuterium content and then approximately $t_{\rm D} \propto X_{\rm D}$. The longer duration of the deuterium burning phase leads to the larger radius.

In the extreme case, $X_{\rm D} = 0$, the contraction phase lasts until hydrogen burning occurs. The radius reaches $\sim 0.3 R_\odot$ and the central temperature becomes high enough to ignite hydrogen.

The evolutionary tracks are also largely changed. The difference in luminosity is at most two orders of magnitude. Contrary to the initial condition variation, the deuterium fraction has a great impact only in the region where $\log T_{\rm eff} \gtrsim 3.5$.

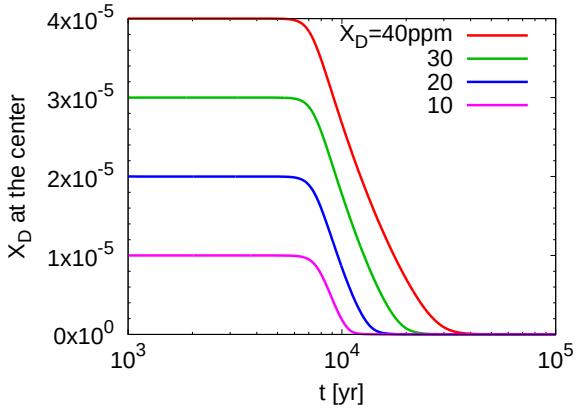

Figure 3.21: Deuterium mass fraction at the center with time. The duration of deuterium burning is roughly proportional to the deuterium fraction.

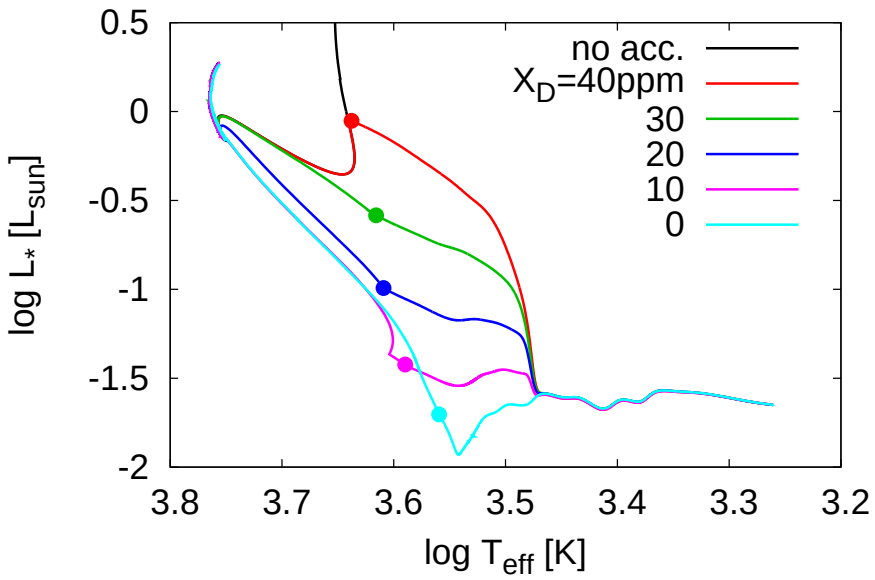

Figure 3.22: evolutionary tracks with varying the deuterium content. While the evolutions are independent of the deuterium content in the low temperature region, they deviate after deuterium ignites. The difference of the luminosity is at most two order of magnitude.

3.3 Hot accretion

In this section we explore the effect of the varying heat injection by the accreting materials. We parameterized the heat injection using a scaling parameter ξ as $L_{\rm add} = \xi L_{\rm acc}$ (Eq. 2.38). The varying ξ corresponds to the different environment of the star formation. The small ξ results from the accretion through the disk in which the entropy is lost efficiently or the accretion accompanying the efficient radiative cooling at the stellar surface. On the other hand, the high

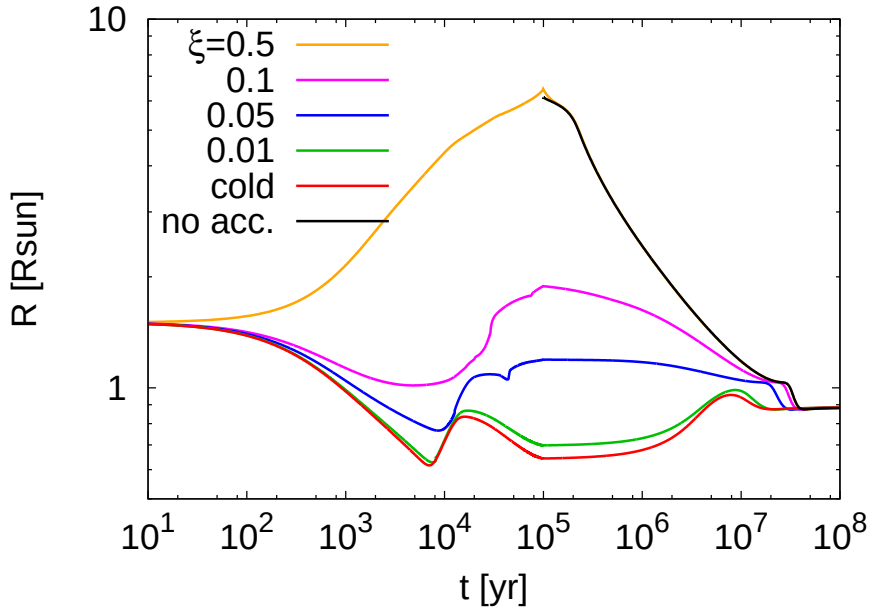

Figure 3.23: Dependence of the radius evolution on the injected heat content.

ξ results from the spherical accretion or the accretion in which the radiative cooling of the energy generated by the viscous heating is inefficient.

Figure 3.23 shows the radius evolution with the injected heat content ranging $\xi = 0.01$–0.5. We find that the variation of the heat injection has the strongest impact on the radius evolution compared to the accretion history, the initial condition and the deuterium content. This is because varying the heat injection efficiency ξ corresponds to changing the accreting material's entropy as

$$\int_0^{M_\star} \left(T \frac{\partial s}{\partial t} \right) dm = \xi \frac{G M_\star \dot{M}}{R_\star} \ , \tag{3.18}$$

and the total injected energy by the accreting materials, $\int (\xi L_{\rm acc}) dM$, is larger than either the energy injected by the deuterium burning or the energy which results form the different accreting material's entropy in the case of the cold accretion due to the different initial stellar entropy.

In the case of $\xi = 0.5$, the radius when the accretion is completed (i.e., at 10^5 yr) is almost the same as the result of the classical hydrodynamic simulation with the spherical accretion by Behrend & Maeder (2001). The difference of the radius between $\xi = 0.5$ and the cold accretion is about one order of magnitude.

There are three features in the radius evolution. Firstly, in the cases with the small $\xi \lesssim$

0.05, the stars contract before deuterium ignites, while the radius in the case that $\xi = 0.5$ is monotonically increases. In the case that $\xi = 0.1$, the star only slightly shrinks. Again, this behavior can be understood from the energy balance equation (3.12). Equation (3.12) shows that in the case with $\xi_{\rm crit} = 1-2C$, the radius evolution is not affected by the mass accretion and is determined only by the thermal timescale. If ξ exceeds this critical value and the bolometric luminosity is negligible, the mass accretion results in the expansion as

$$R_\star \propto M_\star^{2+(\xi-1)/C} \ . \tag{3.19}$$

In the case of the fully convective star with monoatomic gas, $\xi_{\rm crit} = 1/7$. Therefore, the monotonic increase in the case of $\xi = 0.5$ is only caused by $L_{\rm acc}$.

Secondly, in the case of $\xi = 0.5$, due to the large radius, deuterium fusion starts at $\sim 1.2 \times 10^5$ yr, namely after the accretion is completed. Moreover, at this time the luminosity exceeds 10 $L_\odot$ and $L_{\rm nuc}$ does not reach $L_\star$ contrary to the cold accretion. Therefore, deuterium burning only delays the shrink rather than expansion. At last it converges the classical model. In the spherical accretion, the accreting material forms the shock front at the stellar surface and its gravitational energy is thermalized. Although the radii when the accretion is completed in the classical simulations have a little variety, the our result with the hot accretion with $\xi = 0.5$ seems to correspond to them.

Finally, in the case of $\xi = 0.1$, the expansion at $\sim 3 \times 10^4$ yr is sharp. This is because that the heat injection suppresses the contraction effect by accretion and then deuterium burning tends to produce the rapid expansion. From the energy balance equation,

$$\frac{\dot{R}}{R_\star} = -\frac{1}{10}\frac{\dot{M}}{M_\star} + \frac{7}{3}\frac{RL_{\rm nuc}}{GM^2} \ . \tag{3.20}$$

Thus, compared to the cold accretion (Eq. 3.14), the impact of accretion is suppressed by a factor of 3/10 in the case that $\xi = 0.1$.

The evolutionary tracks are also largely changed by the heat injection as shown in Fig. 3.24. The difference is large in the wide range of the effective temperature contrary to the variations of the deuterium content or the initial condition. However, the variation in the heat injection does not shift the evolutionary tracks downward on the H-R diagram. The less luminous region is only reached by the initial condition variation.

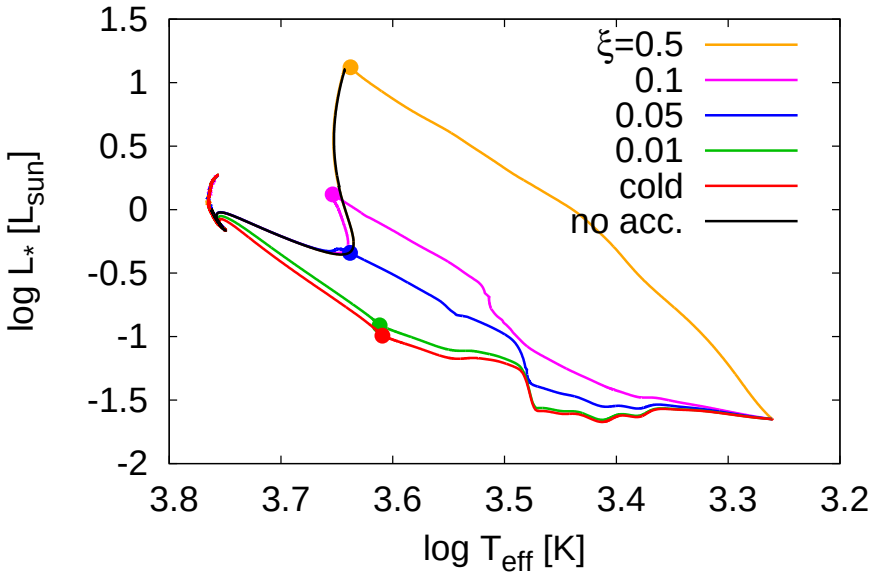

Figure 3.24: Evolutionary tracks with varying the injected heat content.

3.3.1 Changing the heat injection with time

The heat injected to the star by the accreting materials has been poorly understood. Since it is difficult to determine ξ from the observation, theoretical study using the (magneto-) radiation-hydrodynamic simulation is highly encouraged. Baraffe et al. (2012) speculated that ξ is correlated to the mass accretion rate as follows. They assumed that the higher mass accretion rate resulted in the higher fraction of the stellar surface is covered by the accreted materials. Thus, a large amount of the accreting materials prevent stars from losing the entropy and ξ is large.

Since the mass accretion rate decreases with time, here we explore the effect of the large ξ only at the beginning following Hosokawa et al. (2011). Figure 3.25 shows the evolutions with switching ξ from 0.5 to 0. We have found that the evolution with $\xi = 0.5$ even until 0.05 $M_\odot$ deviates the cold accretion and does not converge before reaching their main sequence. This is because of the large K-H timescale and of the setting in the cold accretion. Once the evolutions deviate, it takes long time for them to converge because the difference of their total energies remains in the K-H timescale. Furthermore, once the star gets the large entropy, the accreting material's entropy increases because we assume that the entropy of the accreting materials is equal to that of the star. Note that although this assumption may not be appropriate, the determination of the entropy of the accreting materials is beyond the scope of this study.

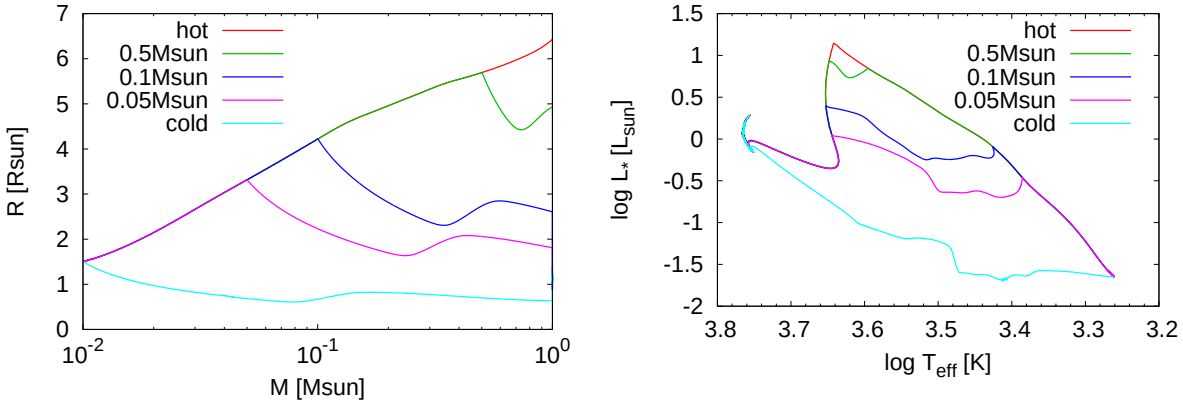

Figure 3.25: (a) *Left panel.* Radius evolutions with mass. Red and cyan lines show the evolutions with ξ is always 0.5 and 0, respectively, while the evolutions with time-dependent ξ are shown by the green, blue and magenta lines. The masses at which ξ changes from 0.5 to 0 abruptly are 0.5, 0.1 and 0.05 $M_\odot$, respectively. (b) *Right panel.* Evolutionary tracks with varying the injected heat content.

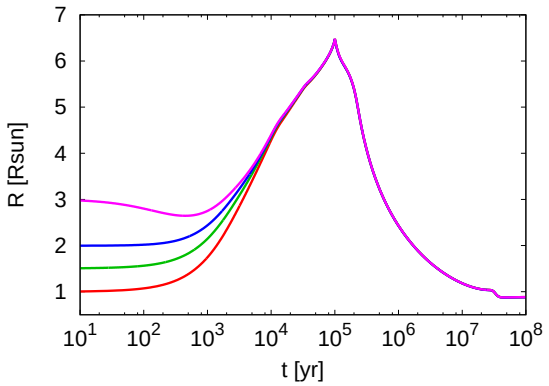

Figure 3.26: Dependence on the initial radius in the case of hot accretion $\xi = 0.5$, [D] $= 2.0 \times 10^{-5}$ and $\dot{M} = 1.0 \times 10^{-5}$ $M_\odot$/yr.

3.3.2 Varying initial condition with hot accretion

Although we described the importance of the initial condition variation in Sec. 3.2.2, it does not have an impact in the case that ξ is large (e.g., Stahler 1988). Since the large initial radius results in the low $L_{\rm acc}$ at the same mass, the star does not receive a large amount of the heat injection where $L_{\rm add} = \xi L_{\rm acc}$. Moreover, the K-H contraction has effect due to the large luminosity. On the other hand, the small initial radius enhances the $L_{\rm acc}$ and then the star expands more quickly. Therefore, the evolutions converge. We stress that this happens only in the case of the sufficiently large ξ.

Chapter 4

Discussion

In the previous chapter we have shown the big difference between the classical PMS evolution and that with the cold accretion. In this chapter we discuss whether the cold accretion is possible in reality from the two approaches using the disk model in Sec. 4.1 and the observational results in Sec. 4.2. Secondly, we describe the application of the cold accretion for the stellar surface composition, including our Sun. Finally, as an application to the planet formation, we investigate the disk evolution including the PMS evolution.

4.1 Validity of the cold accretion

Here we verify the assumption of the cold accretion that the entropy of the accreting material, $s_{\rm acc}$, is the same as that of the stellar surface, $s_\star$. There are two possible mechanisms to satisfy this condition (Hartmann et al. 1997):

1. the efficient energy loss in the disk, no disk inner edge, and the rapid rotation of the star
2. high-velocity accretion (e.g., through the magnetospheric accretion) and the energy loss at the stellar surface

In the first, it is assumed that the accreting material's entropy is the same as the stellar surface and there is no gravitational and kinetic energy difference between the disk inner edge and the stellar surface. In the latter, it is assumed that the efficient energy loss by the irradiation at the shock front adjusts the accreting material's entropy.

First, we estimate the temperature and density at the disk inner edge using a simple disk model. Using the typical temperature, $T_{\rm eff}$, and density, $\rho_\star$, at the stellar surface, the entropy difference between the stellar surface and the disk inner edge, $\Delta s \equiv s_{\rm acc} - s_\star$, is evaluated.

As a result, the entropy of the disk material is higher than that of the stellar. Secondly, we discuss another possibility of the origin of the cold accretion. Note that in this section we suppose the typical values in the mass accretion phase, namely $M_\star \sim 0.1\ M_\odot, R_\star \sim 2\ R_\odot$, $\dot{M} = 10^{-5}\ M_\odot/\mathrm{yr}, T_{\mathrm{eff}} = 2000$–$4000$ K, and $\rho_\star \sim 10^{-6}$ g/cm^3.

4.1.1 Entropy at the disk inner edge

We evaluate the entropy at the disk inner edge, i.e. temperature and density, using a simple disk model. The detail of the estimation is described in Appendix B and here we summarize the estimation. As a result, the entropy at the disk inner edge can be higher than the stellar surface.

Here we describe the procedure of essential points of the estimation. The temperature is determined by the viscous heating and the irradiation from the central star. In the former mechanism, the temperature at the disk surface, T_{vis} is determined by the accreting material's gravitational potential. In the strong accretion, the former dominates. Considering the energy is transported vertically by the radiation, in the diffusion approximation, the temperature at the midplane is determined by $T_{\mathrm{vis,mid}}$ and the optical thickness, τ, from the midplane to the disk surface. Note that the optical thickness is determined by the sum of the opacity and the surface density, Σ. In addition, if we assume the so-called α-viscosity, $\alpha = \alpha c_s^2/\Omega_{\mathrm{K}}$, and the accretion is steady state, namely $\dot{M} = 3\pi\Sigma\nu \neq \dot{M}(r)$, then the surface density is linked to the temperature. Therefore, we obtain the solutions for $T_{\mathrm{vis,mid}}$ and Σ. Finally, using the surface density and temperature, the density at the midplane, ρ_{mid}, is determined. if we assume the hydrostatic equilibrium in the vertical direction, the pressure scale hight, h, is given by $h = c_s/\Omega_{\mathrm{K}}$. We obtain ρ_{mid} by dividing the surface density by the vertical hight, $\sim 2h$.

From the estimation described in Appendix B, we have found that the density at the disk inner edge is close to the stellar surface value ($\sim 10^{-6}$ g/cm^3), while the temperature there is much higher ($\sim 10^5$ K) than the stellar surface. This is mainly due to the large mass accretion rate ($\sim 10^{-5} M_\odot$/yr) and the small surface area to radiate the energy at the disk inner edge ~ 0.01 AU. The high temperature leads to the high heat injection efficiency, $\xi \sim 0.24$. Therefore, we conclude that the accreting material brings much energy to the stellar surface and then the cold accretion is not realized in the case of the Keplerian disk which does not have the inner edge.

Our estimation is consistent with the results in Popham et al. (1993). They calculated the temperature at the inner boundary layer of the disk with varying the mass accretion rate and found that it becomes much higher than the stellar surface in the case of the strong

$\gtrsim 10^{-5}\ M_\odot$/yr. They suggested that in such a case the entropy is advected in the radial direction, rather than dissipated in the vertical flux. Although the settings are different (e.g., they supposed the disk around 1 $M_\odot$ star), our rough estimation is in agreement with their results.

Moreover, the radiative heating from the disk surface may have effect due to the higher disk surface temperature ($\sim 10^4$ K) than the stellar temperature (~ 3000 K), although Adams & Shu (1986) claimed that this is a second-order effect. This may also increases the heat injection efficiency, ξ.

4.1.2 Entropy loss at the stellar surface

Another possibility is that the entropy of the accreting material is lost at the stellar surface and adjusted to be equal to that of the stellar surface.

If the material accretes with the supersonic velocity in the radial direction[1] , the shock front is formed at the stellar surface. The kinetic energy is thermalized at the shock front and then the temperature of the accretion column is high ($\sim 10^4$ yr; e.g., Hartigan et al. 1991).

Hartmann et al. (1997) claimed that most of this energy is lost via radiation to space in the case of the thin disk accretion. They showed that the optical thickness toward the stellar interior is much greater than that to space in the thin disk and claimed that the accreting material's entropy is adjusted to that of the stellar surface.

Although Hartmann et al. (1997) claimed the validity of the cold accretion with a simple estimate, it is still unclear whether both the kinetic energy and the extra internal energy of accreting material can be lost even if the entropy of the accreting material is higher than the stellar surface. The classical PMS evolution assumes the spherical accretion. On the other hand, in the multi-dimensional hydrodynamic simulations of the disk around protostars, the stellar surface region does not solved because it is the computationally expensive (Vorobyov & Basu 2010). Therefore, it is highly encouraged to investigate the accreting material's entropy onto a protostar through the disk accretion via a multi-dimensional radiative-hydrodynamic simulation.

[1]For example, the supersonic infall can be realized as follows. If the central star has a sufficiently strong magnetic field, the material accretes onto the star along the magnetosphere of the central star (e.g., Koenigl 1991). In this case the disk inner edge is located at around the coronation radius where the Keplerian frequency is comparable to the stellar rotation frequency.

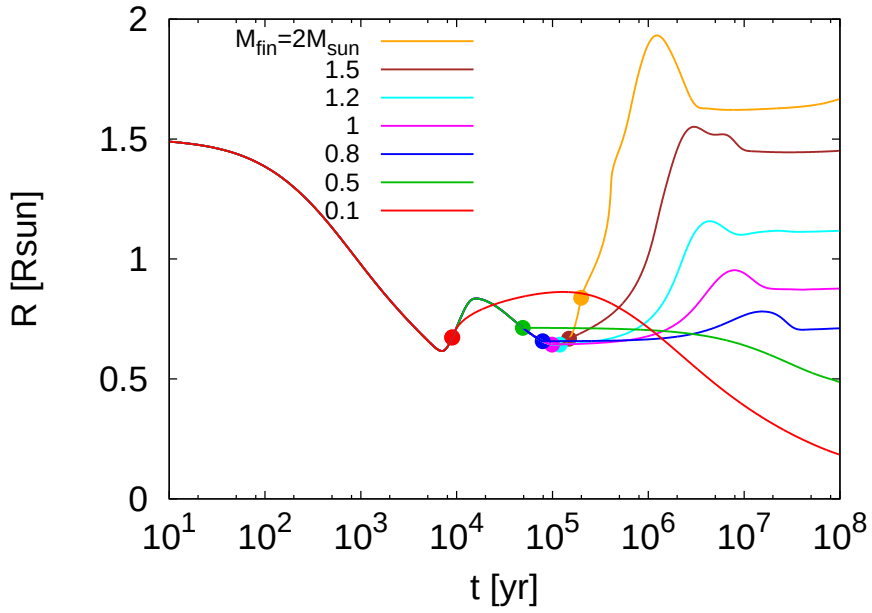

Figure 4.1: Radius evolution of the stars with the different final mass through the cold steady accretion. From the top, the final masses are 2 $M_\odot$ (orange line), 1.5 $M_\odot$ (brown), 1.2 $M_\odot$ (cyan), 1 $M_\odot$ (magenta), 0.8 $M_\odot$ (blue), 0.5 $M_\odot$ (green) and 0.1 $M_\odot$ (red). The points indicate the location where the accretion completes.

4.2 Implication for the evolutionary tracks on the H-R diagram

In order to discuss the validity of the cold accretion from the comparison with the observation on the H-R diagram, we have to compile the different mass stars' evolutionary tracks. We also describe the impact of the cold accretion on the "luminosity spread problem".

4.2.1 Varying the final mass

In this section we show the different mass star's formation other than 1 $M_\odot$ through the steady accretion from a 0.01 $M_\odot$ seed protostar in the cases that $\xi = 0, 0.1$ and 0.5.

First the evolution in the case of the cold accretion is shown in Fig. 4.1. The radius evolutions after the accretion phase quickly deviate. The higher-mass ($\geq 1.2\ M_\odot$) stars expand after the accretion because of hydrogen burning. The lower-mass stars shrink even in 10^8 yr because of the long K-H timescale.

In the case of the 0.1 $M_\odot$ star's formation, the star expands due to deuterium burning for a long period of time. This is because $L_{\rm nuc}$ is much larger than $L_\star$ and then the star expands. The expansion decreases $T_{\rm c}$ and then the deuterium burning lasts until $\sim 2\times10^5$ yr. In the H-R diagram, the 0.1 $M_\odot$ star temporarily evolves upward vertically after the accretion as shown in

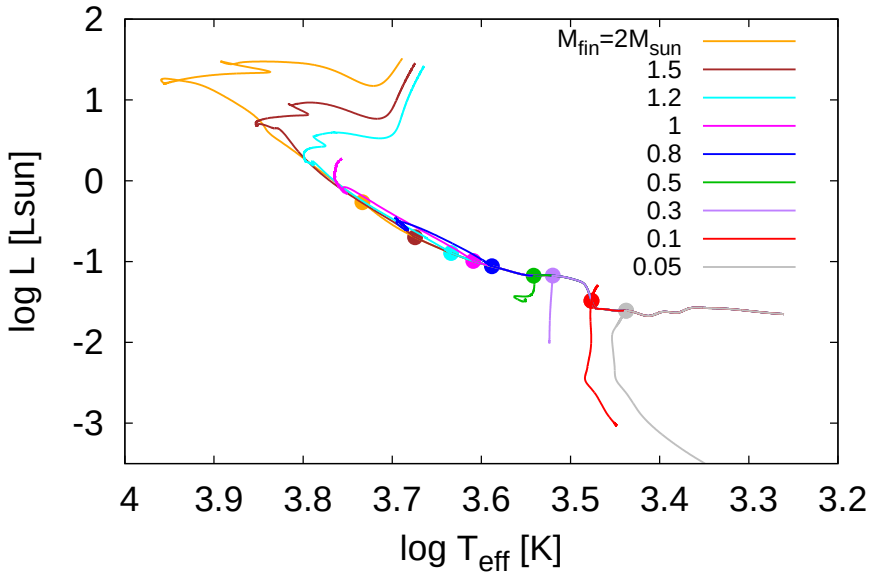

Figure 4.2: Evolutionary tracks with varying the final mass, $M_{\rm fin}$. While the initial conditions are the same (the 0.01 $M_\odot$ star with $\log T_{\rm eff} \simeq 3.25$), the accretion stops abruptly. The filled circles indicate the location where the accretion is completed. The calculation stops at 10^{10} yr or when the radius exceeds 8 $R_\odot$.

Fig. 4.2. This is because the star evolves along the Hayashi track, which is roughly vertical for the constant mass due to the strong temperature sensitivity of the opacity by negative hydrogen ions, and then the expansion leads to the vertical shift.

The end points of the tracks are 10^{10} yr or the time when the radii exceed 8 $R_\odot$. The latter criteria corresponds to the time when the stars starts ascending their red-giant branches and is used for the higher-mass (≥ 1.2 $M_\odot$) stars, which have the shorter MS lifetime due to the much vigorous hydrogen burning.

Next we show the evolutionary tracks in the cases that $\xi = 0.1$ and 0.5. Basically the stars evolve along the evolutionary tracks shown in Fig. 3.24, and after the accretion stops they move to their Hayashi tracks.

4.2.2 Impact on the luminosity spread problem of PMS stars

As described in Sec. 1.2.1, the cold accretion is a possible solution for the luminosity spread problem. Here we revisit this problem by comparing our evolutionary tracks with the observation. We show two results: First, the stars with varying the heat injection produce the luminosity spread even if their ages are the same as claimed by Baraffe et al. (2009) and Hosokawa et al. (2011). However, we have found that the smaller ξ is certainly needed to explain some stars

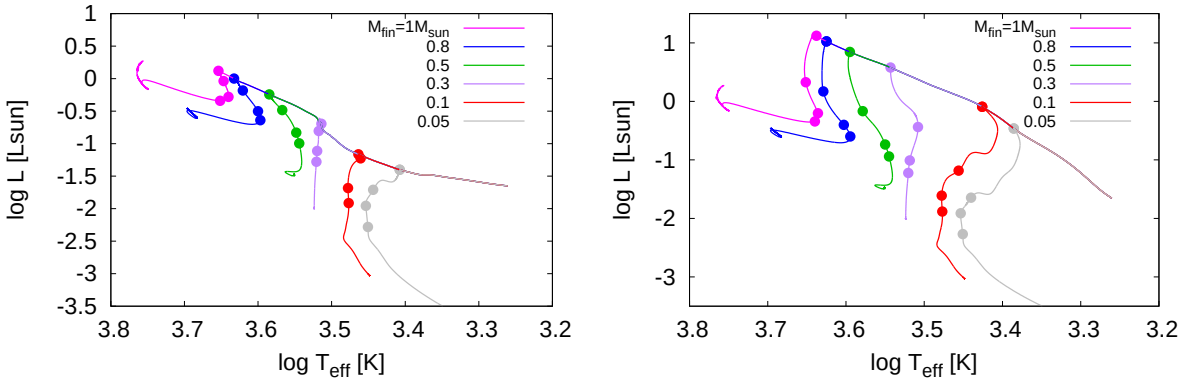

Figure 4.3: Evolutionary tracks with varying the final mass, $M_{\rm fin} = 0.05$ (grey line), 0.1 (red), 0.3 (purple), 0.5 (green), 0.8 (blue) and 1 $M_\odot$ (magenta), in the cases of $\xi = 0.1$ (left panel) and 0.5 (right). The points indicate the location where the accretion stops and the ages are equal to 1 Myr, 5 Myr and 10 Myr.

even though the number of them is only about 10% in the stars with the similar temperature.

As shown in Fig. 1.4, we compare the observation with the isochrones in the cases of $\xi = 0, 0.05, 0.1$ and 0.5, which are derived by compiling the evolutionary tracks in Figs. 4.2 and 4.3. Figure 4.4 shows the 1, 5 and 10 Myr isochrones with varying ξ. We have found that the stars located in the luminous and high temperature region can not be covered by the small ξ and then the isochrones with $\xi \gtrsim 0.05$ are needed especially in the high ($\gtrsim 3500$ K) temperature region. This is consistent with the conclusion in Hosokawa et al. (2011).

In addition, we have found that this region can not be covered by the high deuterium content as shown in Fig. 4.5. We again stress that the fact that the deuterium fraction highly affects the PMS evolution in the case of the cold accretion is found by our study. As described in Sec. 3.2.3, the deuterium content is also affect the evolution largely especially in the high temperature region. However, this effect is not sufficient even in the higher limit of the current ISM deuterium fraction $X_{\rm D} = 35$ ppm[2].

Therefore, we have found that the finite ξ is needed even if the interstellar deuterium fraction is high. Figure 4.6 shows that the 1 Myr isochrones with varying ξ covers the wide range of the H-R diagram. Thus, our results support the Baraffe et al. (2009)'s suggestion that the wide spread of the PMS stars on the H-R diagram can be explained the variation in the heat injection efficiency.

On the contrary, we have also found that the PMS accretion with the small ξ is surely needed for the two less luminous objects with ~ 4000 K and 0.1 $L_\odot$. These objects are not

[2]The present-day ISM deuterium fraction is still under debate, ranging from 10 to 35 ppm as described in Sec. 2.3.1.

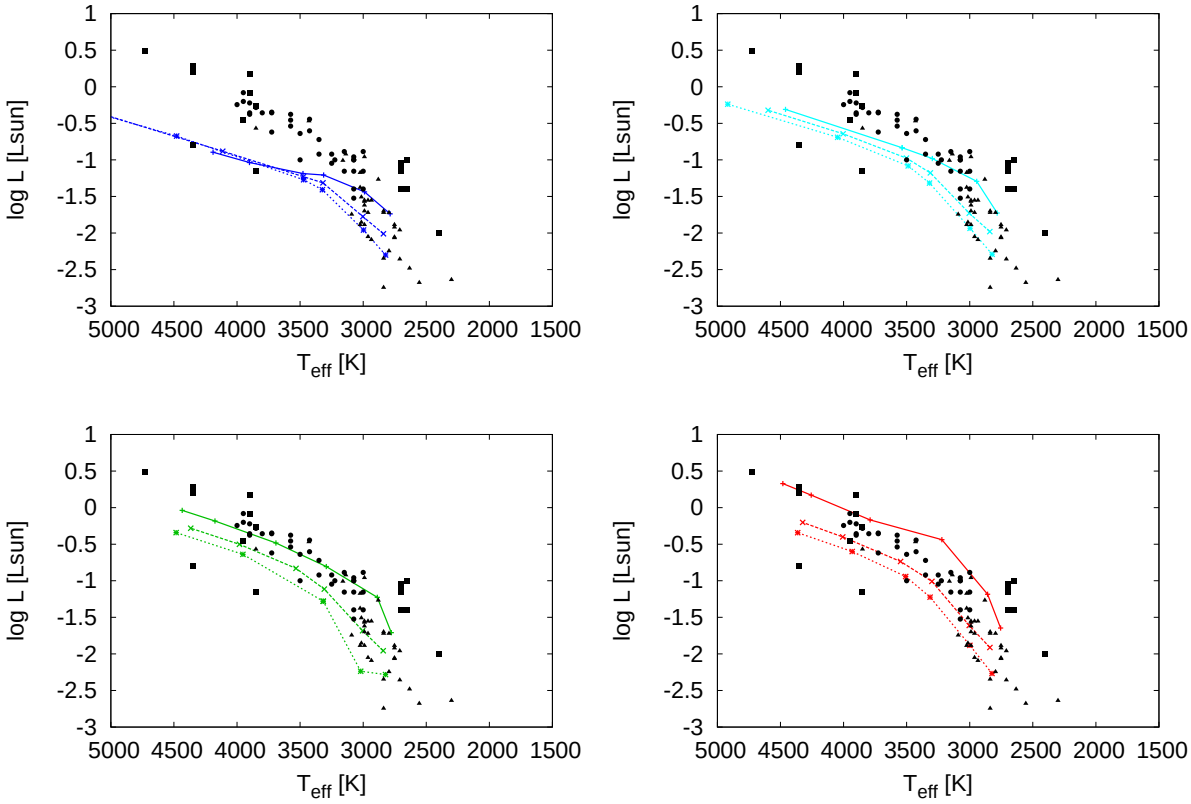

Figure 4.4: Isochrones at 1 Myr (solid line), 5 Myr (dashed) and 10 Myr (dotted) in the cases of $\xi = 0$ (top left panel), 0.05 (top right) 0.1 (bottom left) and 0.5 (bottom right). The triangles, squares and circles are the young stellar objects in Tauras and Chamaeleon I (Muzerolle et al. 2005), ρ Ophiucus (Gatti et al. 2006) and σ Orionis (Gatti et al. 2008).

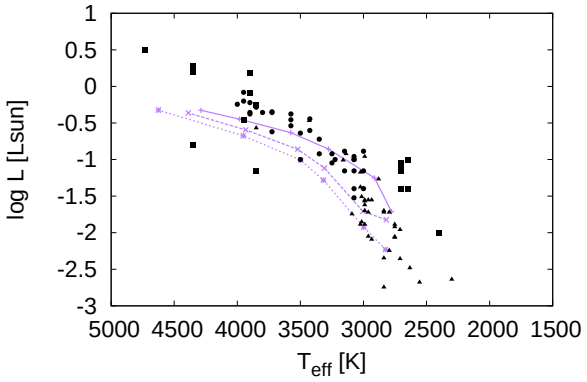

Figure 4.5: Isochrones at 1 Myr (solid line), 5 Myr (dashed) and 10 Myr (dotted) in the cases of $X_{\rm D} = 35$ ppm.

explained by the isochrones with the large ξ and $X_{\rm D}$. Considering there are about 20 objects where $T_{\rm eff} = 3500$–4500, the probability of the cold accretion with small deuterium fraction is

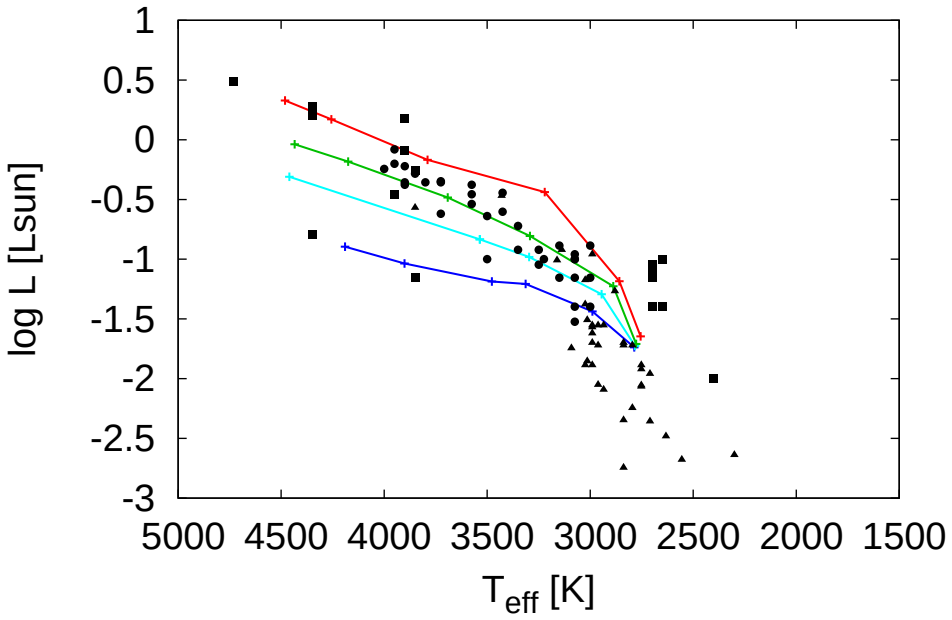

Figure 4.6: Isochrones at 1 Myr in the cases of $\xi = 0.5$ (red), 0.1 (green), 0.05 (cyan) and 0 (blue). The isochrones with varying ξ cover the wide range of area where the observed points exist on the high-temperature region.

roughly estimated to be about 10%. Therefore, we concluded that the accretion with $\xi < 0.05$ is rare ($\sim 10\%$) but is certainly needed.

Note that the number of the less luminous objects is only two. Thus, we have to consider the possibility that the low luminosity of the two objects results from the observational error. These stars are the members of the star forming region ρ Ophiuchus and Gatti et al. (2006) derived that the observational error in $L_\star$ is typically 0.5 dex for the members of this region. Moreover, we note that the less luminous objects are found only in this region. The other regions, i.e., Tauras and Chamaeleon I and σ Orionis, do not contain the less luminous objects which is consistent with the cold accretion. Therefore, both the increase of the number of the observational samples and the enhancement of the observational precision are required.

We note that if the distance to the star is more properly determined, the precision of the observation of the stellar luminosities and the membership possibility to the star forming region are expected to be highly improved. We expect that the precise determination of the distances to stars by the Gaia satellite will contribute to the understandings of the young stellar objects.

Finally, we address the degeneracy of the evolution. From Figs. 4.4 and 4.5, we have found that a location on the H-R diagram can be passed by the evolutionary tracks with the various settings (e.g., the isochrones with $\xi = 0.05$ in Fig. 4.4 are similar to those in the cold accretion

with the high deuterium content in Fig. 4.5). The changes in ξ and $X_{\rm D}$ are essentially equal, that is, these result in the change of the entropy. Thus, it is difficult to distinguish these. However, unlike the heat injection, the primordial deuterium fraction can be indirectly inferred using the fraction of ^{3}He, which is the product of deuterium fusion. If the ^{3}He is determined by the spectroscopic observation and then the initial deuterium fraction is determined, then the degeneracy is solved. We note that, however, in general it is difficult to determine the surface compositions of the young stellar objects by the spectroscopic observation.

4.3 Implication for the stellar surface composition

As shown in Sec. 3.1.3, the internal structure evolution can be largely different in the case of the cold accretion from the classical model. This also has lots of implications for the stellar evolution and the planet formation theory as described in Sec. 1.2.1. In this section we summarize the ages when the surface convective zone (CZ) becomes 0.1 $M_\star$ under a variety of settings. With these results, we especially focus on the effect of the "pollution" of the stellar surface composition of 1 $M_\odot$ stars. We have found that the age of CZ shrinkage is close to the observed protoplanetary disk's lifetime and then the pollution can occur, even though it might be rare.

4.3.1 Effect of the weak mass accretion after the main mass accretion phase on the internal structure

Before showing the results of the internal structure evolutions, it should be noted that although we have investigated the PMS evolution with the accretion which abruptly stops at 9.9×10^4yr, in reality the weak ($\sim 10^{-8}$ $M_\odot$/yr) accretion lasts until the disk lifetime ($\sim$ 6 Myr). So far we have assumed that the weak accretion after the main accretion phase has a strong impact because the even tow-orders-of-magnitude variation of the mass accretion rate is not important. In order to connect the PMS evolution to the protoplanetary disk's accretion, we verify the assumption. Figure 4.7 shows the evolution with changing the mass accretion rate. The settings are the same as those listed in Table 3.1 other than the accretion rate. It is initially 10^{-5} $M_\odot$/yr until 9.7×10^4 yr, namely 0.98 $M_\odot$, and then changed to be 10^{-8} $M_\odot$/yr until 2.097×10^6 yr. Note that the mass of the protoplanetary disk, $M_{\rm disk}$, around T Tauri stars at $\sim 10^6$ yr is typically 0.01 $M_\star$ (Williams & Cieza 2011). As expected, the weak mass accretion does not change the accretion because the accretion timescale is much longer than the thermal timescale in the swelling phase (about several million years; see Sec. 3.1.1) and then the evolution is not affected.

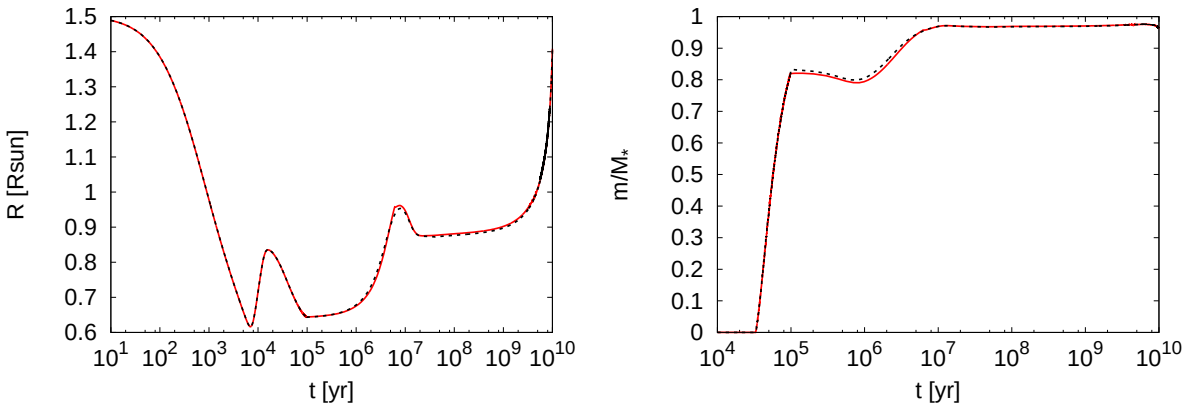

Figure 4.7: Evolution of the radius (left panel) and the internal structure (right panel) including the weak accretion after the main accretion phase. The dashed line indicates the result of the steady accretion in Sec. 3.1.1. The mass accretion rate is initially 10^{-5} $M_\odot$/yr until the star reaches 0.98 $M_\odot$ at 9.7×10^4 yr, while it is $(1/3) \times 10^{-8}$ $M_\odot$/yr until 6.097×10^6 yr.

4.3.2 Age of the surface convective zone shrinkage

In this section we explore the dependence of the internal structure evolution on the mass accretion rate, the initial radius, the deuterium mass fraction, the heat injection efficiency and the final mass. The internal structure evolutions are summarized in Fig. 4.8. We found that they are largely affected by the settings except for the mass accretion rate.

Here we define $t_{\rm CZ}$ as the time when the mass in the surface convective zone, $M_{\rm CZ}$, becomes 0.1 $M_\star$ and $t_{\rm CZ}$ under a variety of settings are summarized in Fig. 4.9.

4.3.3 Impact on the anomaly of the solar surface composition

As described in Sec. 1.2.1, the early shrinkage of CZ due to the cold accretion is helpful to solve the problem of the peculiar solar surface composition. Here we derive the conditions that the surface convective zone of the young sun shrunk before the protosolar nebula dissipated.

If this condition is satisfied, the following scenario to solve the solar anomaly problem can work. Figure 4.10 shows the schematic picture of this scenario. The chemical composition of the accreting materials can be largely affected by the planetesimal formation, which removes the refractory elements from the accreting gas. Thus, the composition of the accreting materials can be different from the stellar one and then the accretion acts as the pollution. In order for the pollution to work efficiently, the stellar surface convective zone is required to be thin. Otherwise (i.e., if the star is fully convective), the pollution is diluted within the entire star and the pollution of the surface composition is limited.

Here we assume that the disk lifetime is $t_{\rm disk} = 6$ Myr $(M_\star/M_\odot)^{-0.5}$ (Haisch et al. 2001,

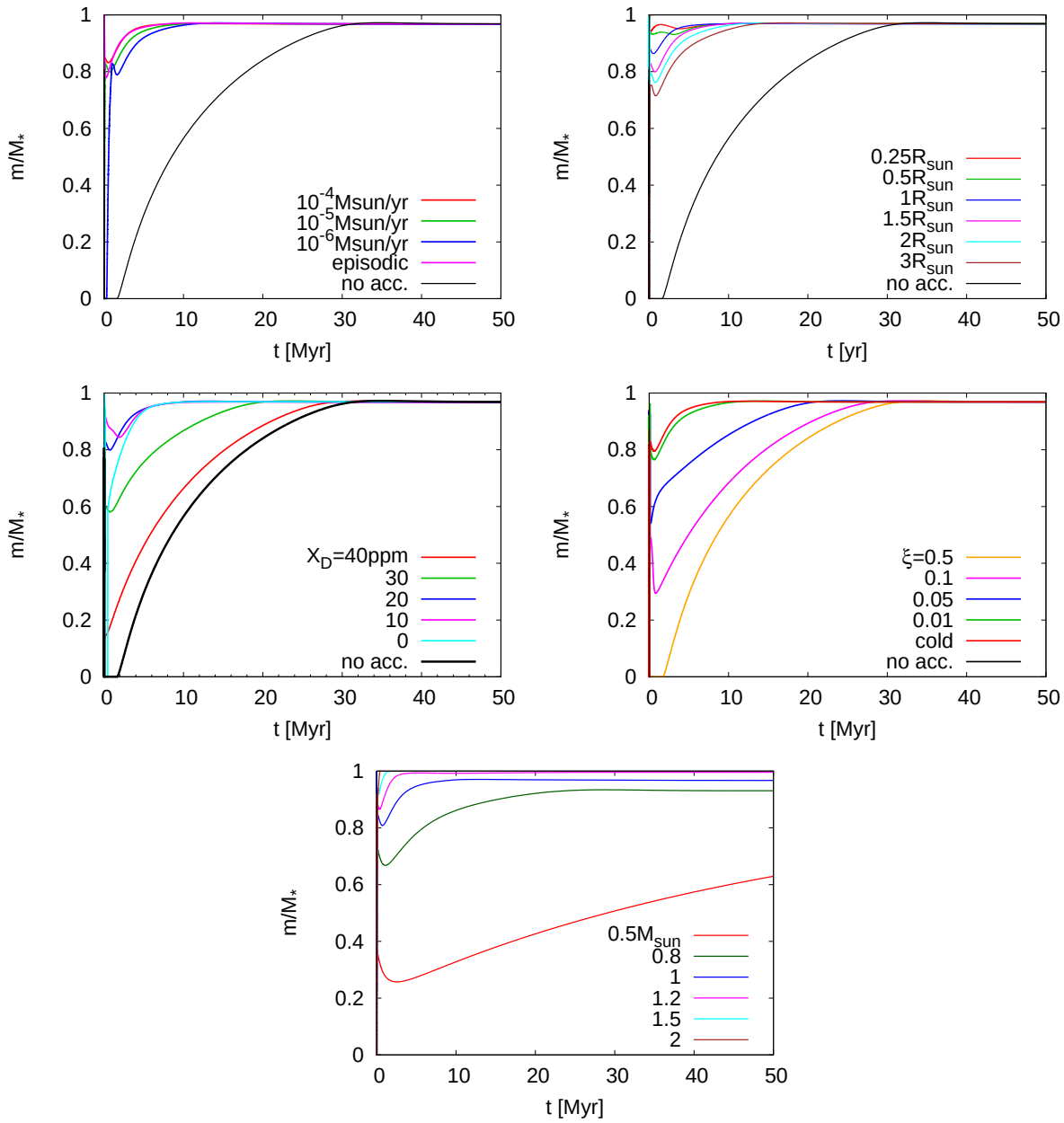

Figure 4.8: Evolution of the radiative core mass with varying (upper left) the mass accretion rate, (upper right) the initial radius, (middle left) the deuterium mass fraction, (middle right) the heat injection efficiency and (bottom) the final mass.

Yasui et al. 2014). From Fig. 4.9, we have derived the conditions that $t_{\rm CZ} < t_{\rm disk}$ as follows:

$$\xi < 0.03, \qquad R_{\rm ini} < 3\ R_\odot, \qquad X_{\rm D} < 2.5 \times 10^{-5}, \qquad M_{\rm fin} > 0.9\ M_\odot\ . \tag{4.1}$$

Furthermore, we investigate the conditions of ξ and $X_{\rm D}$ for the early shrinkage of CZ under a variety of settings. They are summarized in Fig. 4.11. In the deuterium-poor environment, the

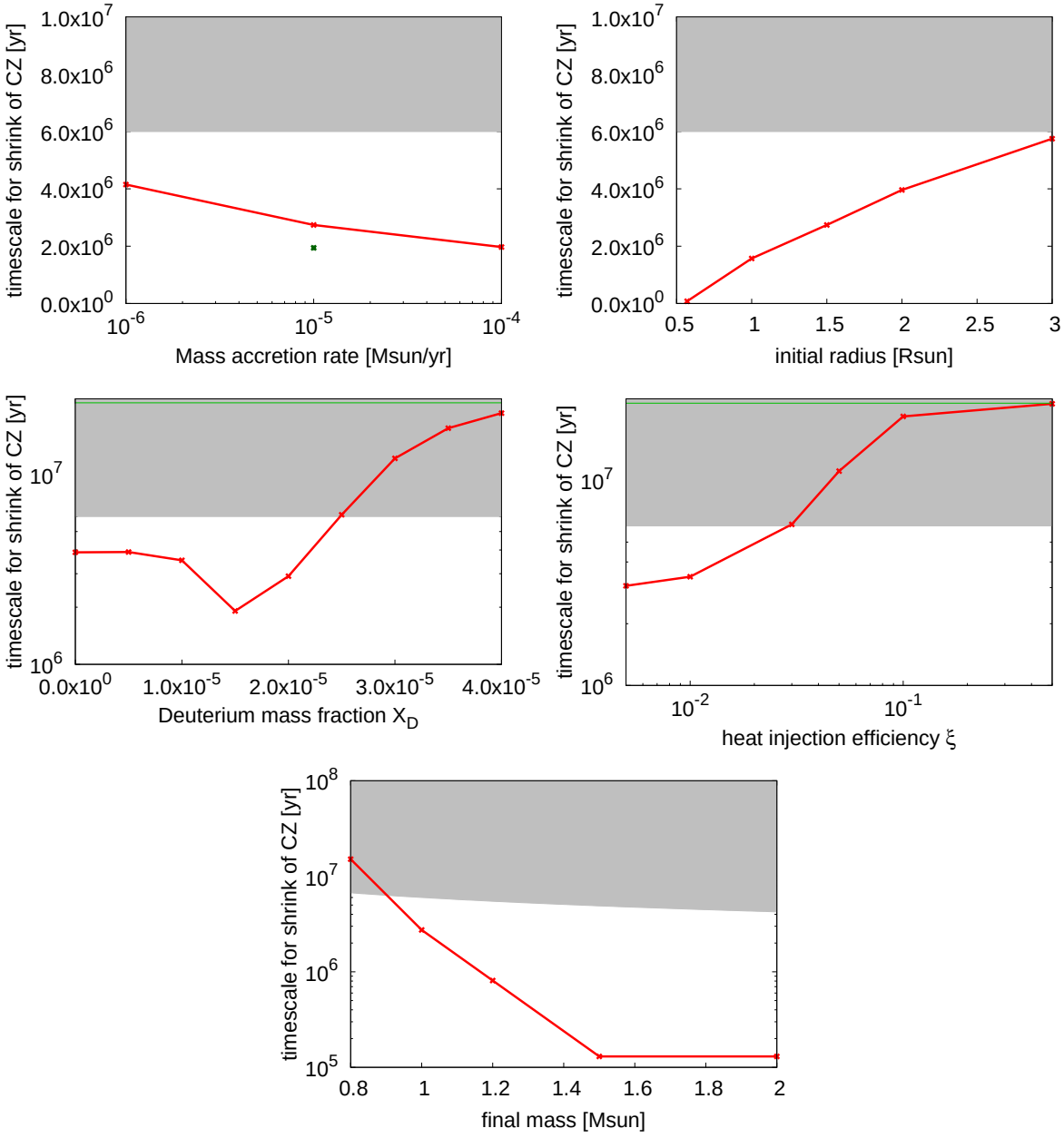

Figure 4.9: $t_{\rm CZ}$ with varying (upper left) the mass accretion rate, (upper right) the initial radius, (middle left) the deuterium mass fraction, (middle right) the heat injection efficiency and (bottom) the final mass. Note that the standard settings are listed in Table 3.1. The shaded region show the region where the disk has dissipated. Here we assume the disk lifetime as 6 Myr$(M_\star/M_\odot)^{-0.5}$ from Haisch et al. (2001) and Yasui et al. (2014) for the dependence on the host star's mass.

condition is relaxed to be $\xi \simeq 0.06$. And even if the cold accretion occurs, the higher deuterium fraction prevents the early shrinkage of the surface convective zone. This is because the total energy available from deuterium burning, $E_{\rm D} = 1.05\ \times 10^{47}$ erg $(X_{\rm D}/2.0\times10^{-5})(M_\star/M_\odot)$ (see

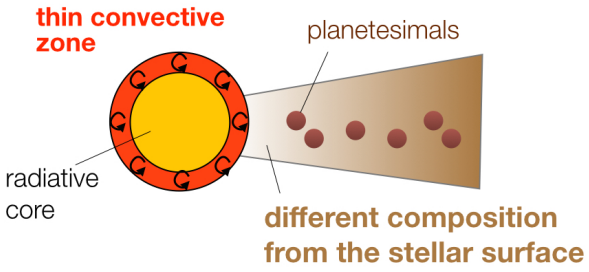

Figure 4.10: Schematic picture of making the anomaly in the surface chemical composition due to the planetesimal formation. The planetesimal formation removes the refractory elements from the accreting materials. The refractory-poor (i.e., relatively volatile-rich) accretion makes the stellar surface composition different from the initial one. This effect is visible in the case of the star with the sufficiently thin CZ.

Eq. 2.29), is comparable to the total injected energy given by

$$E = \int \xi L_{\rm acc} dt = \frac{\xi}{2} \frac{G M_\star^2}{R_\star} \sim 5.67 \times 10^{46} \ {\rm erg} \left(\frac{\xi}{0.03} \right) \left(\frac{M_\star}{M_\odot} \right)^2 \left(\frac{R_\star}{R_\odot} \right)^{-1} . \tag{4.2}$$

Here we discuss whether the anomaly of the solar surface composition results from the pollution or not. As described in Sec. 2.3.1, the deuterium fraction of the protosolar nebula is indirectly estimated to be $X_{\rm D,PSN} \simeq 25$–31 ppm. If the higher value is preferred in the future research, the pollution hypothesis for the solar composition anomaly should be abandoned.

Even if the deuterium fraction of the protosolar nebula was small within the error and $\xi = 0$, the age of CZ shrinkage is larger than the typical disk lifetime, 6 Myr. However, we have found that, if the disk lifetime is as long as 10 Myr, the pollution may work. Therefore, our results suggest that the lifetime of the protosolar nebula was longer than the typical disk lifetime of low-mass stars.

The final mass also has a strong impact on $t_{\rm CZ}$. From 0.8 to 1.5 $M_\odot$, it roughly scales with $M_\odot^7$. This is because the timing of the development of the radiative core highly depends on the temperature and then the stellar mass. Although we neglected the effect of the mass loss from the young Sun in this thesis, it has recently suggested that the young sun was as massive as 1.02 $M_\odot$ (Suzuki et al. 2013) as described in Sec. 2.5.1. The 2% increase of the initial mass of the young sun decreases $t_{\rm CZ}$ by 15%.

In order to solve the problem of the anomaly of the solar surface composition, we have to integrate the evolution of the accreting materials's composition due to the planetesimal formation such as **?** to our results of $M_{\rm CZ}$ evolution in future.

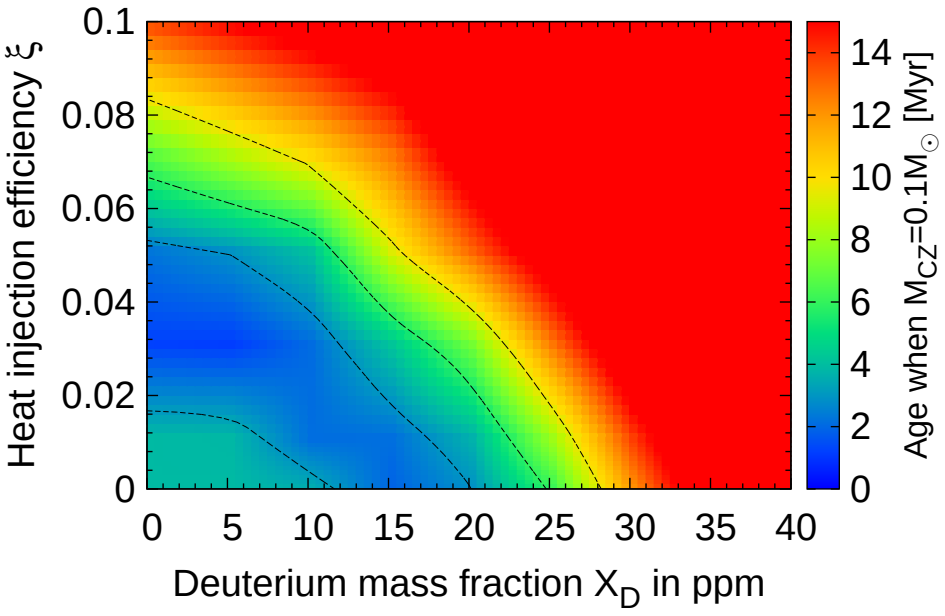

Figure 4.11: Age when the surface convective zone becomes 0.1 $M_\star$ on the ξ-$X_{\rm D}$ plane. The three lines indicate the location at 3, 6 and 10 Myr. The line at 3 Myr is separated in the low $X_{\rm D}$ and ξ region because the stellar radius becomes small enough to ignite hydrogen even in the PMS (see 3.2.3). Note that the protosolar deuterium fraction is thought to be 25–31 ppm. The settings other than ξ and $X_{\rm D}$ are standard values listed in Table 3.1 (e.g., $R_{\rm ini} = 1.5\ R_\odot$ and $M_{\rm fin} = 1\ M_\odot$).

4.4 Application to the protoplanetary disk's evolution

The protoplanetary disk's lifetime is an important quantity in the planet formation theory because it sets the maximum allowed timescale for the planet formation. In addition, since planets migrate via the interaction with the disk gas, it can largely affect the orbital distribution of planets. Therefore, in this section, we investigate the protoplanetary disk's evolution as an example of the impact of the stellar evolution on the planet formation.

The radiation from the host star is thought to be an important physical mechanism for the disk dissipation, which is called photoevaporation. We have investigated the time evolution of the luminosity of ultraviolet photons and X-rays from the host star. As a result, we have found that the stellar evolution is highly important for the disk evolution especially around intermediate-mass stars.

4.4.1 Overview of disk evolution

The dominant effects for the protoplanetary disks' dissipation are currently thought to be the following two effects: viscous accretion and photoevaporation [3](Armitage 2011, Alexander et al. 2013). The latter is a physical mechanism of the mass loss from the disk via the irradiation of the high-energy photons such as far- (FUV; 6–13.6 eV) and extreme-ultraviolet (EUV; 13.6–100 eV) photons and X-rays (> 0.1 KeV). The disk material subject to irradiation of such photons obtains the energy and if the thermal energy exceeds the gravitational potential of the central star, the material can escape into space. Therefore, the luminosity of those photons is critical for the disk lifetime. However, its time-dependence has not been investigated.

4.4.2 Model and computational method

We simulate the evolution of the surface density profile with a simple one-dimensional model. The disk evolves due to the effects of viscosity and irradiation of the high-energy photons. The evolution of the surface density distribution can be solved with the following differential equation

$$\frac{\partial \Sigma}{\partial t} = \frac{3}{r}\frac{\partial}{\partial r}\left(\sqrt{r}\frac{\partial}{\partial r}\left(\nu\Sigma\sqrt{r}\right)\right) - \dot{\Sigma}_{\rm PE} \ , \tag{4.3}$$

where r, Σ, ν, and $\dot{\Sigma}_{\rm PE}$ indicate the distance from the central star, the surface density, viscosity coefficient, and the mass loss rate by photoevaporation (Clarke et al. 2001). Note that the $\dot{\Sigma}_{\rm PE}$ can be treated as a source term because in the photoevaporative flow the material is lost without changing its angular momentum.

As for the viscosity, we use the so-called α-viscosity, $\nu = \alpha c_s h$ (Shakura & Sunyaev 1973), where c_s and h are the isothermal sound speed and the vertical pressure scale hight. The temperature at the midplane, $T_{\rm mid}$, is in general determined by the irradiation and viscous heating. In this study we simply assume the optically thin disk as

$$T_{\rm mid} = 280\,{\rm K}\left(\frac{r}{\rm AU}\right)^{-1/2}\left(\frac{L_\star}{L_\odot}\right)^{1/4} \ . \tag{4.4}$$

Using the photoevaporation rate from the literature, we can simulate the disk evolution.

[3]Hollenbach et al. (2000) examined the variety of disk removal mechanisms such as accretion, planet formation, stellar encounter, stellar winds and photoevaporation and concluded that viscous accretion and photoevaporation are dominant mechanisms. Note that although recently Suzuki & Inutsuka (2009) found that the magneto-rotational instability generate a wind and its mass loss rate is significant enough to affect the disk evolution, in this thesis we consider the viscous evolution and photoevaporation.

Photoevaporation rate

In this study we include extreme-ultraviolet (EUV; 13.6–100 eV) and X-ray (> 0.1 KeV) photoevaporation by the central star and especially focus on the time-dependence of the X-ray luminosity.

The EUV dissociate the hydrogen atoms at the uppermost layer of the disk. Due to the strong temperature sensitivity of the opacity, the temperature at the layer is fixed to 10^4 K. However, since the launching point of the photoevaporative flow by X-ray widely spreads, the photoevaporation rate is more complicated. We adopt the fitting formula of the photoevaporation rate derived by radiation-hydrodynamic simulations by Font et al. (2004), Alexander et al. (2006a,b), and Owen et al. (2012).

Furthermore, we consider the photoevaporation by the direct irradiation after the inner disk dissipates. While EUV photons reaches the outer disk through the recombination in the inner region at first, after the gap opens EUV photons can reach the outer region directly.

Time-evolution of EUV and X-ray luminosity

Observationally, the X-ray luminosity of T Tauri stars is well determined. It is well known that it correlates to the bolometric luminosity as $L_{\rm X}/L_\star \sim 10^{-3.5}$ (Preibisch et al. 2005, Flaccomio et al. 2003), although the physical mechanism of this relation is still not revealed. However, since this relation is known to be valid for the fully convective stars, the vigorous X-ray luminosity may arise form the strong convective motion.

On the other hand, the X-ray luminosity of intermediate-mass PMS stars on their Hayashi track is poorly understood since the evolution of intermediate-mass stars is fast and they have little or no Hayashi phase. The X-ray luminosity of two intermediate-mass PMS stars on their Hayashi track is reported by Stelzer et al. (2009), Hamaguchi et al. (2005) and their results are consistent with the T Tauri stars, i.e. they also have X-ray luminosity $L_{\rm X}/L_\star \sim 10^{-3.5}$. Therefore we use this X-ray luminosity on the fully convective stars.

After the star evolves, the radiative core develops and X-ray luminosity also decreases. For the Herbig Ae/Be stars, the X-ray luminosity is detected as $L_{\rm X}/L_\star \sim 10^{-6}$ (e.g., Zinnecker & Preibisch 1994).

Intermediate-mass stars evolve quickly and then the disk lifetime can be longer than the PMS duration. After the star reaches the main sequence, the X-ray luminosity much more decreases as $L_{\rm X}/L_\star \sim 10^{-9}$ (e.g., Cassinelli et al. 1994).

In order to compile these observational results, we model the evolution of X-ray luminosity

Table 4.1: Settings.

Initial disk mass	0.1 $M_\star$
Initial disk radius	10 AU
Viscous parameter α	10^{-3} $(M_\star/M_\odot)$
$\Phi_{\rm EUV}$	10^{41} s^{-1}

using the convective zone mass, $M_{\rm CZ}$, as

$$L_{\rm X} = \max\left(10^{-3.5} L_\star \left(\frac{M_{\rm CZ}}{M_\star}\right), 10^{-6}\right) \tag{4.5}$$

before reaching MS. After MS, it is changed to

$$L_{\rm X} = \max\left(10^{-3.5} L_\star \left(\frac{M_{\rm CZ}}{M_\star}\right), 10^{-9}\right) \tag{4.6}$$

The EUV photon luminosity is poorly constrained because EUV is highly absorbed by the interstellar medium and it is difficult to detect it. Due to the lack of the observational knowledge, its origin is also not revealed. Although it may result from the chromospheric activity, it is possible that the accretion generates EUV Matsuyama et al. (2003). In order to focus on the time-dependence of X-ray luminosity, in this study we set EUV photon luminosity, $\Phi_{\rm EUV}$, to be constant to 10^{41} s^{-1}.

Initial condition and the input parameters

From observational results, we assume that the initial disk mass is proportional to the host star's mass, i.e. $M_{\rm disk} \propto M_\star$ Williams & Cieza (e.g., 2011). However, since the disk size is poorly constrained to date, we set the constant initial radius.

The correlation between the mass accretion rate and the stellar mass is well known as $\dot{M} \propto M_\star^2$ (Muzerolle et al. 2005, Calvet et al. 2004). Since the origin of the $\dot{M}$–$M_\star$ relation still remains unclear Ercolano et al. (2014), here we assume $\alpha \propto M_\star$ following Gorti et al. (2009). Note that the PMS stars' luminosity is approximately proportional to the square of its mass [4] and the disk is assumed to be in the steady accretion with α-viscosity.

We summarize the settings in this study in Table 4.1.

[4]Note that the mass-luminosity relation in the PMS stars is known to be weaker than that of MS stars, $L_\star \propto M_\star^4$ according to the results of numerical simulations.

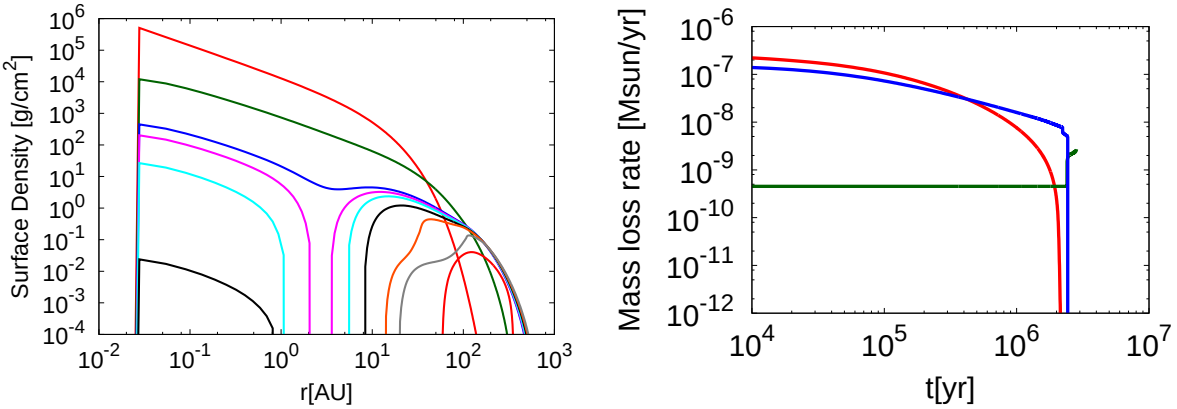

Figure 4.12: *Left panel.* Surface density evolution of the disk around a 1 $M_\odot$ star at 0, 1, 2, 2.05, 2.1, 2.2, 2,3, 2.4 and 2.5 Myr from the top. After the gap opens at 2.05 Myr (magenta line), both the inner and outer disk dissipates within 0.5 Myr. *Right panel.* Mass accretion rate onto the star (red line) and photoevaporation rate by X-rays ($\dot{M}_{\rm X}$, blue) and EUV photons ($\dot{M}_{\rm EUV}$, green). $\dot{M}_{\rm X}$ is two to one orders of magnitude higher than $\dot{M}_{\rm EUV}$. Time-dependence in $\dot{M}_{\rm X}$ is not strong.

4.4.3 Disk evolution around low-mass star

In this section we show the disk evolution around a 1 $M_\odot$ star. Figure 4.12 shows the surface density evolution around a 1 $M_\odot$ star.

At 2.05 Myr, the gap opens at ~ 3 AU. This gap is formed by X-ray photoevaporation when the mass accretion rate, $\dot{M}_{\rm acc}$, drops to the X-ray photoevaporation rate, $\dot{M}_{\rm X}$. After the gap opens, the inner disk is quickly drained by the host star. This is because the viscous timescale, $\tau_{\rm disk}$, of the inner disk is short as

$$\begin{aligned} \tau_{\rm disk} &\sim R_{\rm disk}^2/\nu \\ &\sim 0.24\ {\rm Myr} \left(\frac{\alpha}{10^{-3}}\right)^{-1} \left(\frac{T}{280{\rm K}}\right)^{-1} \left(\frac{R_{\rm disk}}{3{\rm AU}}\right)^{0.5} \left(\frac{M_\star}{1M_\odot}\right)^{0.5} . \end{aligned} \tag{4.7}$$

We have found that $\dot{M}_{\rm X}$ is two to one orders of magnitude higher than $\dot{M}_{\rm EUV}$ and time-dependence in $\dot{M}_{\rm X}$ is not strong.

4.4.4 Disk evolution around intermediate-mass star

Figure 4.13 shows the surface density evolution around a 3 $M_\odot$ star. The disk lifetime is longer than the After leaving the Hayashi tracks, the X-ray luminosity becomes much smaller and after several million years EUV photoevaporation becomes dominant. This feature is not seen in the disk evolution around low-mass stars.

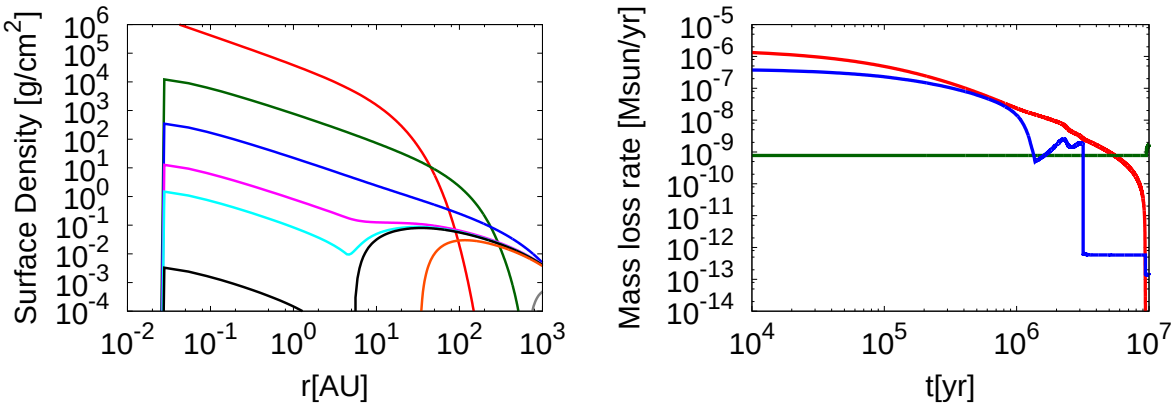

Figure 4.13: *Left panel.* Surface density evolution of the disk around a 3 $M_\odot$ star at 0, 1, 5, 9, 9.3, 9.4, 10 and 12 Myr from the top. *Right panel.* Mass accretion rate onto the star (red line) and photoevaporation rate by X-rays ($\dot{M}_{\rm X}$, blue) and EUV photons ($\dot{M}_{\rm EUV}$, green). $\dot{M}_{\rm X}$ largely changes with time and after several million years EUV becomes dominant.

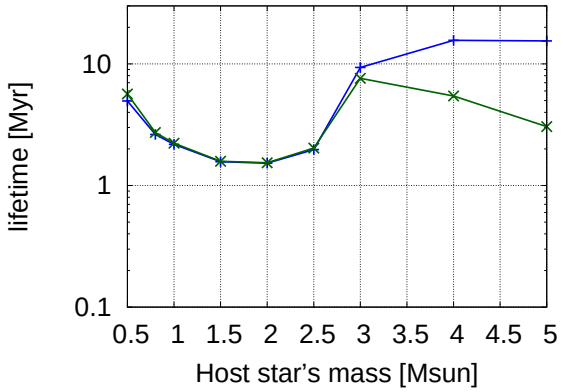

Figure 4.14: Disk lifetime with the time-dependent X-ray luminosity and constant EUV photon luminosity (blue line) and in the case that the EUV photons from the photosphere are considered (green).

4.4.5 Dependence of the disk lifetime on the host star's mass

Performing the disk evolution calculation as above, we investigate the dependence of the disk lifetime on the host star's mass. Here we define the disk lifetime as the time when the optical thickness of the disk in the vertical direction, $\tau \sim \kappa\Sigma$, becomes lower than unity. The mass opacity κ is assumed to be 10 cm^2/g (Miyake & Nakagawa 1993).

Figure 4.14 shows the disk lifetime with the host star's mass. We have found that the disk lifetime decreases as the host star's mass becomes higher within a range of 0.5 to 2 $M_\odot$ due to the large X-ray luminosity. However, for the stars more massive than 2 $M_\odot$, it increases due to the rapid decrease of the X-ray luminosity, and the dominant source of photoevaporation can be changed from X-rays to EUV photons. Thus, we found that the UV photoevaporation

is important for the disk lifetime of high-mass stars. Finally, we investigate the effect of EUV photons from the stellar photosphere.

Effect of EUV photons from the photosphere

While the effective temperature of low-mass stars is too low to emit significant ultraviolet photons, that of intermediate-mass stars is so high that the blackbody spectrum peaks at the ultraviolet. Figure 4.14 shows that the disk lifetime around intermediate-mass stars is highly affected by the EUV photons from the photosphere. Therefore, disks around intermediate-mass stars dissipate mainly by the effect of the EUV photons, contrary to the low-mass stars. We speculate that, by including the effect of the FUV, the disk lifetime around intermediate-mass stars becomes much shorter.

4.4.6 Impact of the cold accretion

In the cold accretion, the bolometric luminosity is much lower than the classical evolution. If the saturation relation still works, the X-ray luminosity is also much lower. Therefore, if the dominant source of photoevaporation is X-ray, the disk lifetime around stars which have experienced the cold accretion becomes longer.

On the other hand, the evolution of stellar effective temperature is faster in the cold accretion. Therefore, the disk lifetime around intermediate-mass stars becomes shorter although its effect is a few Myr.

Chapter 5

Summary

In this thesis, we have numerically simulated the Pre-Main Sequence (PMS) evolution including the accretion from the seed protostar to the low- or intermediate-mass stars. Recently it has been suggested that the PMS evolution is largely changed from the classical picture if the accreting material does not inject much energy into the star i.e., cold accretion. In particular, we have focused on the impact of the heat injection of the accreting material.

We have found that in the cold accretion, there are four phases: the adiabatic contraction phase, the deuterium burning phase, the second contraction phase, and the swelling phase. The star shrinks adiabatically except for the deuterium burning phase. The radius evolution is well fitted by $R_\star \propto M_\star^{-1/3}$. In the deuterium burning phase, the star expands due to the thermostat effect. After the deuterium burning phase, the star shrinks again since the deuterium burning becomes too inefficient to expand. After the accretion stops, the energy flows from the interior to the surface and then the star swells. The swelling happens after the thermal (K-H) timescale in the interior.

We have investigated the dependence of the PMS evolution on the mass accretion rate, the initial condition, the deuterium content, and the heat injection by the accreting material. We have found that the mass accretion history does not have an impact on the evolution. This result is in agreement with Hosokawa et al. (2011).

On the other hand, we have found that the PMS evolution is highly affected by the initial condition, the deuterium content, and the heat injection by the accretion. The change in the initial radius results in the change in the stellar surface entropy, and then the accreting material's entropy is also changed as found in Hosokawa et al. (2011). Note that this feature is only seen in the cold accretion. In the hot accretion, the initial condition variation is lost by the accretion energy (Stahler 1988). Currently the second core formation by three dimensional

simulations including rotation, radiation and magnetic field has intensively been investigated (e.g., Machida et al. 2008, Tomida et al. 2010). We expect that the further understanding of the second core formation enables to constrain the PMS evolution.

Although the effect of varying the deuterium content in the cold accretion has not been investigated by the previous studies, we have found that the deuterium fraction largely changes the evolution. The deuterium content can be different in each star depending on the environment. Since the deuterium was only formed in the first three minutes after the big bang, it decreases with time due to the destruction in the star. Thus, the deuterium can be deficit in the star which formed from the molecular cloud which is highly affected by the stellar wind by a dying star, or formed in the central region of the Galaxy. Therefore, our results may show that the PMS evolution can reflect the Galactic chemical evolution or the local environment of star formation history.

The heat injection highly affects the PMS evolution as expected. We have found that the heat injection of $\xi = 0.05$ is sufficient to deviate the evolution from the cold accretion.

From the comparison of our results with the observation on the H-R diagram, we have found that although the accretion with $\xi < 0.05$ is rare ($\sim 10\%$), a small number of objects certainly requires such an accretion. Therefore, we have reached the conclusion that the cold accretion plays a role in the PMS evolution.

Finally, we have discussed the application of the cold accretion to the stellar surface composition. We have confirmed the result in Baraffe & Chabrier (2010) that the surface convective zone can shrink within several million years in the cold accretion. This early shrinkage of the surface convective zone within the disk lifetime (~ 6 Myr) probably causes the pollution of the stellar surface. This is because, if the material with the composition modified from the initial one (e.g., by the terrestrial planet formation) accretes onto the star with the shallow surface convective zone, then the accreting material is mixed within the tiny region and then the stellar surface composition can be highly affected by the accreting material. We have derived the condition for the early shrinkage of the surface convective zone. The low heat injection efficiency, $\xi \lesssim 0.03$, and low deuterium content $X_{\rm D} < 2.5 \times 10^{-5}$ are needed. Although the accretion with these conditions is not common, it probably exists with $\sim 10\%$ probability. Furthermore, these conditions may be applied to the protosolar nebula. Recent observation suggests that the solar surface composition is peculiar among the solar-twins and is possibly explained by the pollution mechanism. Therefore, the stellar surface composition may be a clue to understand the environment of the planetary system at the early phase. We speculate that the stellar composition would help the search of the Earth-like planet (Ramírez et al. 2009).

Appendix A

Energy conservation of non-accreting stars

In this Appendix, we show that the energy conservation is satisfied in the calculation with MESA in order to verify that our stellar evolution calculation is reliable. After we define the error in the energy conservation of a star, we show that the energy conservation is satisfied in the case of non-accreting stars. We have found that the error in the total energy evolution of non-accreting stars is at most 0.1%.

A.1 Energy conservation equation

The energy conservation law has already been derived in Eq. 2.18 as

$$\int_0^t \left(-L_{\rm grav} - L_\star + L_{\rm nuc} - L_{\rm acc} + L_{\rm add}\right) dt' = 0 \ , \tag{A.1}$$

where $L_{\rm grav}$ is the change rate of the specific energy, $L_\star$ the bolometric luminosity, $L_{\rm nuc}$ the energy production rate by thermonuclear reactions, $L_{\rm acc}$ the gravitational energy of the accreting materials, and $L_{\rm add}$ the heat injection by the accreting materials. Energy conservation in our numerical scheme is checked by this equation. We define the error $\delta_E(t)$ as

$$\delta_E(t) \equiv \frac{\left|\int_0^t \left(-L_{\rm grav} - L_\star + L_{\rm nuc} - L_{\rm acc} + L_{\rm add}\right) dt'\right|}{E_{\rm tot}(t)} \ . \tag{A.2}$$

We show that $\delta_E(t)$ is smaller than the order of unity in the following section.

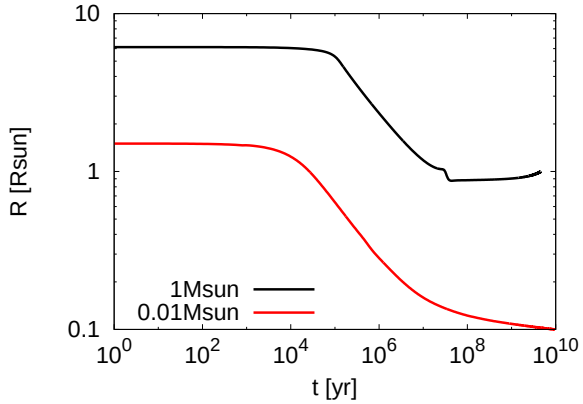

Figure A.1: Radius evolution of the non-accreting 0.01 $M_\odot$ (red line) and 1 $M_\odot$ (black line) star. The plateau in the case of the 1 $M_\odot$ star around 10^5yr is caused by deuterium burning. Note that the radius of the 1 $M_\odot$ star is 1 $R_\odot$ at the solar age, 4.567 Gyr.

A.2 Energy conservation of the non-accreting stars

In this section we show that the energy conservation law is well satisfied in the cases of the non-accreting stars with masses of 0.01 $M_\odot$ and 1 $M_\odot$. The initial radii of 1.5 and 6.1 $R_\odot$, respectively. The other settings are described in Sec. 2.3. The radius evolution is shown in Fig. A.1.

In Eq. (2.18), the terms of the gravitational and internal energies of the accreting material are zero,and the energy conservation is given by

$$\int_0^t (-L_{\rm grav} - L_\star + L_{\rm nuc})\, dt' = 0 \ . \tag{A.3}$$

Furthermore, since 0.01 $M_\odot$ is below the deuterium burning limit $\sim$ 0.013 $M_\odot$, only a little fraction of deuterium is burned. We found that about 1% of deuterium is burned in the 0.01 $M_\odot$ star, and contribution of $L_{\rm nuc}$ to the total energy evolution is limited.

We show the energy evolution of the non-accreting 0.01 $M_\odot$ star in Fig. A.2. The error of the energy conservation in Eq. (A.2) is at most 0.01%, showing that the energy conservation is well satisfied.

The energy evolution of the non-accreting 1 $M_\odot$ star is shown in Fig. A.3. In this case the energy lost by irradiation is dominated by the change of the total energy at first. Then, after the zero-age-main sequence (ZAMS), the stellar structure does not change significantly and it is dominated by the thermonuclear energy production. The error in the energy conservation in Eq. (A.3) is at most 0.1%. Considering that the total energy is about two orders of magnitudes smaller than both the radiative energy loss and the energy production by thermonuclear

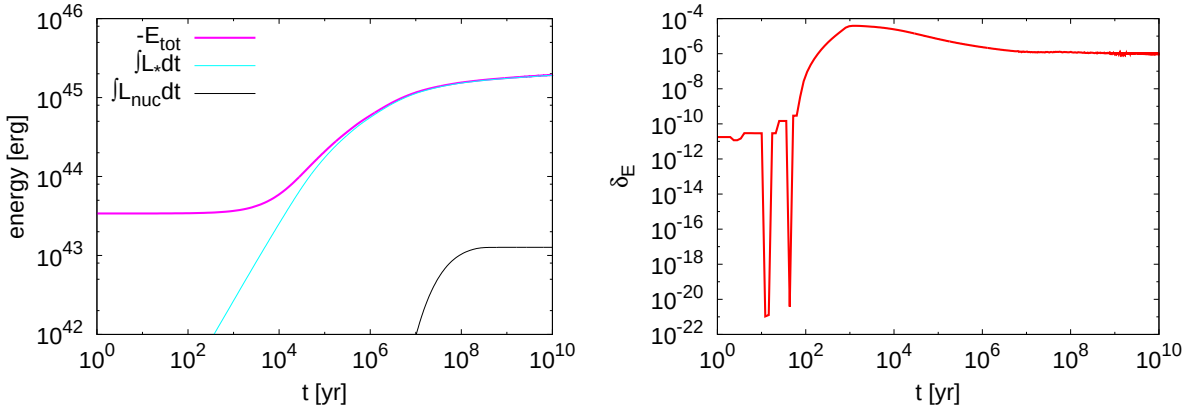

Figure A.2: (a) *Left panel.* Energy evolution of the non-accreting 0.01 $M_\odot$ star. In this case, since the nuclear energy production (black line) is not significant, the change of the total energy (magenta) is compatible to the energy loss ($\int L_\star \mathrm{d}t$, cyan). (b) *Right panel.* Error of the energy conservation in Eq. (A.2), δ_E, with time.

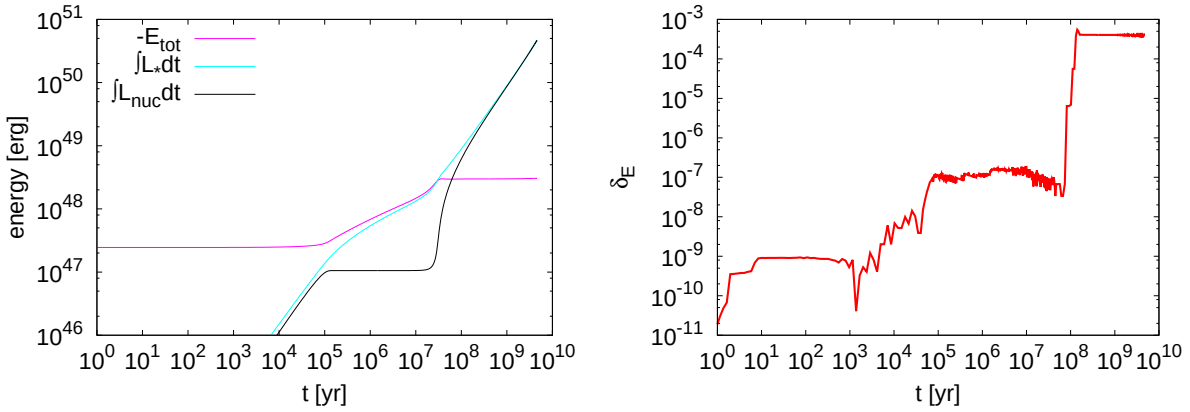

Figure A.3: (a) *Left panel.* Energy evolution of the non-accreting 1 $M_\odot$ star. In this case, the nuclear energy production (black line) is significant after ZAMS and comparable to the energy lost by irradiation (cyan). The the total energy (magenta) is about two orders of magnitude smaller than them. (b) *Right panel.* Error of the energy conservation in Eq. (A.2), δ_E, with time.

reaction, the energy conservation is well satisfied. Thus, we have confirmed the validity of our calculation in the case of non-accreting model.

Appendix B

Estimation of the accreting material's entropy with a simple disk model

In this chapter we estimate the accreting material's entropy during the main mass accretion phase with a extremely simple disk model. We evaluate the temperature and density at the disk inner edge around a protostar. The typical temperature and density of a 0.1 $M_\odot$ protostar are $T_{\rm eff} \sim 2000$–4000 K and $\rho_\star \sim 10^{-6}$ g/cm^3.

As a result, we have found that the extremely high ($\sim 10^5$ K) disk temperature is needed to generate the vigorous accretion. In the typical settings for the main accretion phase, this corresponds to the high heat efficiency, $\xi = 0.24$. Therefore, we conclude that the viscous accretion disk can not be the cold accretion.

The disk temperature at the midplane, $T_{\rm mid}$, is determined by the sum of the irradiation from the star and the viscous heating. The latter essentially means that the released gravitational energy of the accreting material is used to heat up the disk. Therefore,

$$T_{\rm eff,vis}^4 = \frac{3}{8}\frac{GM_\star \dot{M}}{\pi r^3 \sigma_{\rm SB}} \ , \tag{B.1}$$

where $T_{\rm eff,vis}$ is the disk effective temperature at the surface. Substituting the typical values at the disk inner edge around the protostar, namely $M_\star = 0.1\ M_\odot, \dot{M} = 10^{-5} M_\odot$/yr and

$r = 0.01$ AU,

$$T_{\rm eff,vis} = 8500 \text{ K} \left(\frac{r}{0.01 \text{ AU}}\right)^{-3/4} \left(\frac{M_\star}{0.1\ M_\odot}\right)^{1/4} \left(\frac{\dot{M}}{10^{-5}\ M_\odot}\right)^{1/4} . \tag{B.2}$$

The intense mass accretion and the small surface area make the disk surface temperature huge. Thus, we neglect the effect of the irradiation from the central star [1]. If the disk is optically thick in the vertical direction, namely $\kappa\Sigma \gg 1$, then the temperature at the midplane is determined with $T_{\rm eff,vis}$, the opacity and the surface density as

$$T_{\rm mid,vis} = \left(\frac{3}{8}\kappa\Sigma\right)^{1/4} T_{\rm eff,vis} . \tag{B.4}$$

Therefore, we need to evaluate the surface density Σ.

The surface density can be evaluated assuming the steady state accretion driven by the viscosity, namely $\dot{M}_{\rm acc} = 3\pi\Sigma\nu$. However, note that it is questionable whether the circumstellar disk during the main accretion phase has a steady state accretion. The accretion can be driven by the magnetic braking, in which the angular momentum of the disk material is lost by the open magnetic field which thread the disk. In this case the surface density is not necessarily high.

If we assume the disk with the steady state accretion driven by the viscosity, then the surface density around the disk inner edge, $\Sigma_{\rm in}$, is given by

$$\Sigma_{\rm in} = \frac{\dot{M}}{3\pi\nu} , \tag{B.5}$$

where ν is the viscosity of the disk. If we assume the so-called α-viscosity (Shakura & Sunyaev 1973), namely that $\nu = \alpha c_s^2/\Omega_{\rm K}$,

$$\begin{aligned}
\Sigma_{\rm in} &= \frac{\dot{M}\Omega_{\rm K}}{3\pi\alpha c_s^2} \\
&= 1.48 \times 10^5 \text{ g/cm}^2 \left(\frac{T_{\rm mid}}{2000 \text{ K}}\right)^{-1} \left(\frac{M_\star}{0.1\ M_\odot}\right)^{1/2} \left(\frac{r}{0.01 \text{ AU}}\right)^{-3/2} \\
&\quad \left(\frac{\dot{M}}{10^{-5}\ M_\odot/\text{yr}}\right) \left(\frac{\alpha}{1}\right)^{-1} \left(\frac{\mu}{1}\right)^{-1} ,
\end{aligned} \tag{B.6}$$

[1] Even in the optically thin limit, the irradiation temperature is given by

$$T_{\rm irr} = 1.56 \times 10^3 \text{ K} \left(\frac{r}{0.01 \text{ AU}}\right)^{-1/2} \left(\frac{L_\star}{0.1 L_\odot}\right)^{1/4} . \tag{B.3}$$

This is negligible compared to the viscous heating.

Substituting this equation to Eq. (B.4) using Eq. (B.2), we obtain the temperature and surface density in the case that $M_\star = 0.1\ M_\odot, r = 0.01$ AU and $\dot{M} = 10^{-5}\ M_\odot$/yr as

$$T_{\rm mid,in} = 5.66 \times 10^4\ {\rm K}(\kappa/{\rm cm}^2\ {\rm g}^{-1})^{1/5}\ , \tag{B.7}$$

$$\Sigma_{\rm in} = 5.23 \times 10^4 {\rm g/cm}^2(\kappa/{\rm cm}^2\ {\rm g}^{-1})^{-1/5}\ . \tag{B.8}$$

The opacity can be highly dependent on the density and temperature (e.g., Bell & Lin 1994). The density at the midplane can be estimated by the hydrostatic equilibrium as

$$\rho_{\rm mid} = \Sigma/2h \tag{B.9}$$

where h is the pressure scale hight given by

$$h \equiv c_{s,{\rm in}}/\Omega_{\rm K} \simeq 4.08 \times 10^{-4}\ {\rm AU} \left(\frac{T}{2000\ {\rm K}}\right)^{1/2} \left(\frac{r}{0.01\ {\rm AU}}\right)^{3/2} \left(\frac{M_\star}{0.1\ M_\odot}\right)^{-1/2} \tag{B.10}$$

Thus, the density at the midplane at 0.01 AU can be estimated as

$$\rho_{\rm mid} = 3.02 \times 10^{-6}\ {\rm g/cm}^3(\kappa/{\rm cm}^2\ {\rm g}^{-1})^{-3/10}\ . \tag{B.11}$$

At the temperature above $\sim 10^4$ K, the opacity is given as

$$\kappa = 1.5 \times 10^{20} \rho T^{-5/2} \tag{B.12}$$

in cgs unit due to the bound-free and free-free absorptions according to Bell & Lin (1994) (see B.1). Therefore, at the midplane of the disk inner edge, $T_{\rm mid,in} = 1.15 \times 10^5$ K and $\rho_{\rm mid,in} = 1.04 \times 10^{-6}$ g/cm^3. This extremely high temperature is needed in order to produce the vigorous accretion such as $10^{-5}\ M_\odot$/yr.

In order to estimate the entropy difference between the disk inner edge and the stellar surface, we use the estimated midplane temperature and density and the characteristic values of the protostars with 0.1 $M_\odot$ ($\sim$ 3000 K and 10^{-6} g/cm^3). Since the density is almost the same, the temperature difference corresponds to the energy injection given by

$$L_{\rm add} = \dot{M} c_V \Delta T \sim 3.71\ L_\odot \left(\frac{\mu}{0.62}\right)^{-1}\ . \tag{B.13}$$

In the current settings, namely $M_\star = 0.1\ M_\odot, \dot{M} = 10^{-5}\ M_\odot$/yr and $R_\star = 0.01$ AU $\simeq 2\ R_\odot$, the accretion luminosity is 15.6 $L_\odot$ (see Eq. 3.17. Therefore, we obtain the heat injection efficiency

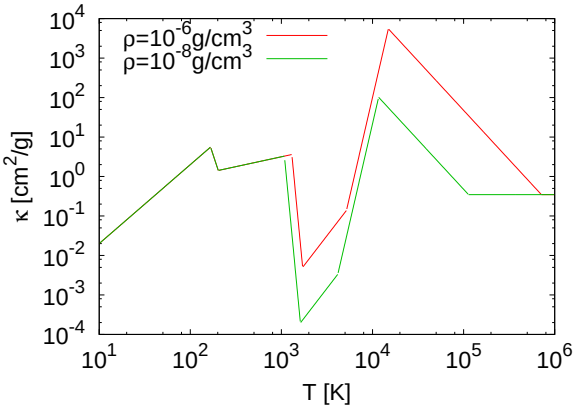

Figure B.1: Opacity in Bell & Lin (1994). The dominant sources are ice, sublimation of ices, metal dust, sublimation of dust, molecules, hydrogen scattering and bound-free and free-free absorption, and electron scattering from low to high temperature.

as $\xi = L_{\rm add}/L_{\rm acc} \sim 0.24$.

References

Adams, F. C. & Shu, F. H. 1986, ApJ, 308, 836

Alexander, R., Pascucci, I., Andrews, S., Armitage, P., & Cieza, L. 2013, ArXiv e-prints

Alexander, R. D., Clarke, C. J., & Pringle, J. E. 2006a, MNRAS, 369, 216

Alexander, R. D., Clarke, C. J., & Pringle, J. E. 2006b, MNRAS, 369, 229

Allard, F., Hauschildt, P. H., Alexander, D. R., Tamanai, A., & Schweitzer, A. 2001, ApJ, 556, 357

Angulo, C., Arnould, M., Rayet, M., et al. 1999, Nuclear Physics A, 656, 3

Armitage, P. J. 2011, ARA&A, 49, 195

Asplund, M., Grevesse, N., Sauval, A. J., & Scott, P. 2009, ARA&A, 47, 481

Bahcall, J. N., Basu, S., Pinsonneault, M., & Serenelli, A. M. 2005, ApJ, 618, 1049

Baraffe, I. & Chabrier, G. 2010, A&A, 521, A44

Baraffe, I., Chabrier, G., Allard, F., & Hauschildt, P. H. 1998, A&A, 337, 403

Baraffe, I., Chabrier, G., & Gallardo, J. 2009, ApJL, 702, L27

Baraffe, I., Vorobyov, E., & Chabrier, G. 2012, ApJ, 756, 118

Barker, A. J. & Ogilvie, G. I. 2010, MNRAS, 404, 1849

Basu, S. & Antia, H. M. 2004, ApJL, 606, L85

Behrend, R. & Maeder, A. 2001, A&A, 373, 190

Bell, K. R. & Lin, D. N. C. 1994, ApJ, 427, 987

Calvet, N., Muzerolle, J., Briceño, C., et al. 2004, AJ, 128, 1294

Cassinelli, J. P., Cohen, D. H., Macfarlane, J. J., Sanders, W. T., & Welsh, B. Y. 1994, ApJ, 421, 705

Cassisi, S., Potekhin, A. Y., Pietrinferni, A., Catelan, M., & Salaris, M. 2007, ApJ, 661, 1094

Castelli, F. & Kurucz, R. L. 2004, ArXiv Astrophysics e-prints

Caughlan, G. R. & Fowler, W. A. 1988, Atomic Data and Nuclear Data Tables, 40, 283

Chambers, J. E. 2010, ApJ, 724, 92

Clarke, C. J., Gendrin, A., & Sotomayor, M. 2001, MNRAS, 328, 485

Dunham, M. M. & Vorobyov, E. I. 2012, ApJ, 747, 52

Eddington, A. S. 1926, The Internal Constitution of the Stars

Ercolano, B., Mayr, D., Owen, J. E., Rosotti, G., & Manara, C. F. 2014, MNRAS, 439, 256

Ferguson, J. W., Alexander, D. R., Allard, F., et al. 2005, ApJ, 623, 585

Flaccomio, E., Damiani, F., Micela, G., et al. 2003, ApJ, 582, 398

Font, A. S., McCarthy, I. G., Johnstone, D., & Ballantyne, D. R. 2004, ApJ, 607, 890

Gatti, T., Natta, A., Randich, S., Testi, L., & Sacco, G. 2008, A&A, 481, 423

Gatti, T., Testi, L., Natta, A., Randich, S., & Muzerolle, J. 2006, A&A, 460, 547

Gorti, U., Dullemond, C. P., & Hollenbach, D. 2009, ApJ, 705, 1237

Grevesse, N. & Sauval, A. J. 1998, Space Sci. Rev., 85, 161

Guillot, T. 1999, P&SS, 47, 1183

Gustafsson, B. 2008, Physica Scripta Volume T, 130, 014036

Haisch, Jr., K. E., Lada, E. A., & Lada, C. J. 2001, ApJL, 553, L153

Hamaguchi, K., Yamauchi, S., & Koyama, K. 2005, ApJ, 618, 360

Hartigan, P., Kenyon, S. J., Hartmann, L., et al. 1991, ApJ, 382, 617

Hartmann, L., Cassen, P., & Kenyon, S. J. 1997, ApJ, 475, 770

Hauschildt, P. H., Allard, F., & Baron, E. 1999a, ApJ, 512, 377

Hauschildt, P. H., Allard, F., Ferguson, J., Baron, E., & Alexander, D. R. 1999b, ApJ, 525, 871

Hayashi, C. 1961, PASJ, 13, 450

Heber, V. S., Baur, H., Bochsler, P., et al. 2008, in Lunar and Planetary Inst. Technical Report, Vol. 39, Lunar and Planetary Science Conference, 1779

Hébrard, G., Tripp, T. M., Chayer, P., et al. 2005, ApJ, 635, 1136

Henyey, L., Vardya, M. S., & Bodenheimer, P. 1965, ApJ, 142, 841

Herwig, F. 2000, A&A, 360, 952

Hillenbrand, L. A. 2009, in IAU Symposium, Vol. 258, IAU Symposium, ed. E. E. Mamajek, D. R. Soderblom, & R. F. G. Wyse, 81–94

Hollenbach, D. J., Yorke, H. W., & Johnstone, D. 2000, Protostars and Planets IV, 401

Hosokawa, T., Offner, S. S. R., & Krumholz, M. R. 2011, ApJ, 738, 140

Hosokawa, T. & Omukai, K. 2009, ApJ, 691, 823

Hosokawa, T., Yorke, H. W., & Omukai, K. 2010, ApJ, 721, 478

Inutsuka, S.-i., Machida, M. N., & Matsumoto, T. 2010, ApJL, 718, L58

Kippenhahn, R. & Weigert, A. 1990, Stellar Structure and Evolution

Kippenhahn, R., Weigert, A., & Weiss, A. 2012, Stellar Structure and Evolution

Koenigl, A. 1991, ApJL, 370, L39

Larson, R. B. 1969, MNRAS, 145, 271

Lellouch, E., Bézard, B., Fouchet, T., et al. 2001, A&A, 370, 610

Linsky, J. L., Draine, B. T., Moos, H. W., et al. 2006, ApJ, 647, 1106

Machida, M. N., Inutsuka, S.-i., & Matsumoto, T. 2008, ApJ, 676, 1088

Mahaffy, P. R., Donahue, T. M., Atreya, S. K., Owen, T. C., & Niemann, H. B. 1998, Space Sci. Rev., 84, 251

Martin, R. G., Lubow, S. H., Livio, M., & Pringle, J. E. 2012, MNRAS, 423, 2718

Masunaga, H. & Inutsuka, S.-i. 2000, ApJ, 531, 350

Matsuyama, I., Johnstone, D., & Hartmann, L. 2003, ApJ, 582, 893

Meléndez, J., Asplund, M., Gustafsson, B., & Yong, D. 2009, ApJL, 704, L66

Miyake, K. & Nakagawa, Y. 1993, Icarus, 106, 20

Muzerolle, J., Luhman, K. L., Briceño, C., Hartmann, L., & Calvet, N. 2005, ApJ, 625, 906

Nelder, J. A. & Mead, R. 1965, The computer journal, 7, 308

Owen, J. E., Clarke, C. J., & Ercolano, B. 2012, MNRAS, 422, 1880

Paxton, B., Bildsten, L., Dotter, A., et al. 2011, ApJS, 192, 3

Paxton, B., Cantiello, M., Arras, P., et al. 2013, ApJS, 208, 4

Popham, R., Narayan, R., Hartmann, L., & Kenyon, S. 1993, ApJL, 415, L127

Prantzos, N. 2007, Space Sci. Rev., 130, 27

Preibisch, T., Kim, Y.-C., Favata, F., et al. 2005, ApJS, 160, 401

Ramírez, I., Meléndez, J., & Asplund, M. 2009, A&A, 508, L17

Seaton, M. J. 2005, MNRAS, 362, L1

Shakura, N. I. & Sunyaev, R. A. 1973, A&A, 24, 337

Soderblom, D. R., Hillenbrand, L. A., Jeffries, R. D., Mamajek, E. E., & Naylor, T. 2014, Protostars and Planets VI, 219

Stahler, S. W. 1988, ApJ, 332, 804

Stahler, S. W. & Palla, F. 2005, The Formation of Stars

Stahler, S. W., Palla, F., & Salpeter, E. E. 1986, ApJ, 302, 590

Stahler, S. W., Shu, F. H., & Taam, R. E. 1980a, ApJ, 241, 637

Stahler, S. W., Shu, F. H., & Taam, R. E. 1980b, ApJ, 242, 226

Stassun, K. G., Feiden, G. A., & Torres, G. 2014, NewAR, 60, 1

Stelzer, B., Robrade, J., Schmitt, J. H. M. M., & Bouvier, J. 2009, A&A, 493, 1109

Sugimoto, D. & Nomoto, K. 1975, PASJ, 27, 197

Suzuki, T. K., Imada, S., Kataoka, R., et al. 2013, PASJ, 65, 98

Suzuki, T. K. & Inutsuka, S.-i. 2009, ApJL, 691, L49

Tomida, K., Tomisaka, K., Matsumoto, T., et al. 2010, ApJL, 714, L58

Townsley, D. M. & Bildsten, L. 2004, ApJ, 600, 390

Vorobyov, E. I. & Basu, S. 2010, ApJ, 719, 1896

Williams, J. P. & Cieza, L. A. 2011, ARA&A, 49, 67

Winkler, K.-H. A. & Newman, M. J. 1980, ApJ, 236, 201

Yasui, C., Kobayashi, N., Tokunaga, A. T., & Saito, M. 2014, MNRAS, 442, 2543

Zinnecker, H. & Preibisch, T. 1994, A&A, 292, 152

Acknowledgments

The author would like to express his gratitude to S. Ida for his helpful comments, reading this manuscript, and supports in his research activity. He is deeply grateful to T. Takeuchi for his valuable advices, stimulating discussions, continuing encouragement, and reading this manuscript. He appreciates useful advice and fruitful discussions offered by T. Guillot, M. Ikoma, T. Nakamoto, B. Sato, M. Nagasawa, H. Nomura, S. Okuzumi, M. Kuzuhara, S. Inutsuka, and T. Hosokawa.

As for the calculation with the stellar evolution code MESA, he also thanks B. Paxton for his kindness of modifying it upon our request.

This work was supported by Grant-in-Aid for JSPS Fellows Grant Number 24·9296.

Finally, thanks go to all the members of the department of Earth and Planetary sciences and the Earth-Life Science Institute (ELSI) for the invaluable and joyful time.